Chem Soc Rev

REVIEW ARTICLE

View Article Online
View Journal | View Issue

Cite this: *Chem. Soc. Rev.*, 2025, **54**, 3387

# MXenes in healthcare: synthesis, fundamentals and applications†

Zaheer Ud Din Babar, [ab] Vincenzo Iannotti, [cd] Giulio Rosati, [a] Ayesha Zaheer, [c] Raffaele Velotta, [c] Bartolomeo Della Ventura, [c] Ruslan Álvarez-Diduk *[a] and Arben Merkoçi *[ae]

Since their discovery over a decade ago, MXenes have transformed the field of "materials for healthcare", stimulating growing interest in their healthcare-related applications. These developments have also driven significant advancements in MXenes' synthesis. This review systematically examines the synthesis of MXenes and their applications in sensing and biomedical fields, underscoring their pivotal role in addressing critical challenges in modern healthcare. We describe the experimental synthesis of MXenes by combining appropriate laboratory modules with the mechanistic principles underlying each synthesis step. In addition, we provide extensive details on the experimental parameters, critical considerations, and essential instructions for successful laboratory synthesis. Various healthcare applications including sensing, biomedical imaging, synergistic therapies, regenerative medicine, and wearable devices have been explored. We further highlight the emerging trends of MXenes, *viz.*, their role as nanovehicles for drug delivery, vectors for gene therapy, and tools for immune profiling. By identifying the important parameters that define the utility of MXenes in biomedical applications, this review outlines strategies to regulate their biomedical profile, thereby serving as a valuable guide to design MXenes with application-specific properties. The final section integrates experimental research with theoretical studies to provide a comprehensive understanding of the field. It examines the role of emerging technologies, such as artificial intelligence (AI) and machine learning (ML), in accelerating material discovery, structure–property optimization, and automation. Complemented by detailed supplementary information on synthesis, stability, biocompatibility, environmental impact, and theoretical insights, this review offers a profound knowledge base for understanding this diverse family of 2D materials. Finally, we compared the potential of MXenes with that of other 2D materials to underscore the existing challenges and prioritize interdisciplinary collaboration. By synthesizing key studies from its discovery to current trends (especially from 2018 onward), this review provides a cohesive assessment of MXene synthesis with theoretical foundations and their prospects in the healthcare sector.

Received 30th July 2024

DOI: 10.1039/d3cs01024d

rsc.li/chem-soc-rev

## 1. Introduction

The integration of two-dimensional (2D) nanomaterials into biomedical applications has marked a transformative era in healthcare innovation, further empowering the technology behind smart and portable devices for personalised healthcare monitoring. These materials are characterised by a large surface-to-volume ratio, mechanical flexibility, and functionalizable surfaces. Their evolution in healthcare follows the path from initial discovery to targeted advancements to address specific limitations or challenges, each of which directly influences the feasibility and effectiveness of these materials in their healthcare applications.[1,2]

Graphene, which is notable for its superior mechanical strength, high electrical conductivity, and large surface area, has been pivotal in advancing biosensing and biomedical research.[3,4] In addition, graphene derivatives with oxygen-rich functional groups, such as graphene oxide (GO) and reduced graphene oxide (rGO), exhibit notable features in for above-mentioned applications.[5] Nonetheless, potential long-term

---

[a] *Catalan Institute of Nanoscience and Nanotechnology (ICN2), CSIC and BIST, Campus UAB, Bellaterra, 08193 Barcelona, Spain. E-mail: ruslan.alvarez@icn2.cat, arben.merkoci@icn2.cat*

[b] *Scuola Superiore Meridionale (SSM), University of Naples Federico II, Largo S. Marcellino, 10, 80138, Italy*

[c] *Department of Physics "E. Pancini", University of Naples Federico II, Via Cintia 26, 80126 Naples, Italy*

[d] *Institute for Superconductors, Oxides and other Innovative Materials and Devices of the National Research Council (CNR-SPIN), Piazzale V. Tecchio 80, 80125 Naples, Italy*

[e] *ICREA Institució Catalana de Recerca i Estudis Avançats, Barcelona, Spain*

† Electronic supplementary information (ESI) available. See DOI: **https://doi.org/10.1039/d3cs01024d**

toxicity, intrinsic hydrophobicity, and inert basal planes have raised concerns, necessitating extrinsic modifications for broader utility.[6,7] Transition metal dichalcogenides (TMDCs), such as $MoS_2$ and $WS_2$, have emerged as semiconducting alternatives that are beneficial for photothermal therapies and biosensors.[8,9] Their moderate conductivity, comparatively better biocompatibility than graphene, and tunable bandgaps make them useful in electronic sensors. The lack of stability in physiological environments can also be a limiting factor, as TMDCs may degrade or lose functionality over time when implanted or used in sensing applications.[10] Moreover, TMDCs may require complex functionalization strategies to improve their selectivity.[11] Beyond graphene and TMDCs, newly discovered 2D materials, such as MBenes[12] and the members of the 'Xenes' family[13,14] stand out with attributes tailored for specialised healthcare applications. Their variable bandgaps and biodegradability offer innovative pathways to develop nontoxic and human friendly medical devices. Silicene, a member of the Xenes family, is predicted to have a high piezoresistance gauge factor (GF), demonstrating high pressure sensitivity, and thus holds promise for wearable electronics.[15] However, research on these new 2D materials is still in its early stages and requires long-term investigation and clinical inspection.

Transition metal carbides, nitrides and carbonitrides, also called MXenes ($M_{n+1}X_nT_x$), are a type of 2D materials with exceptional features for healthcare research and applications,[16,17] such as, the hydrophilic surface of MXenes offers robust colloidal stability and antibiofouling properties.

**Zaheer Ud Din Babar**

*Zaheer Ud Din Babar earned his PhD in Mathematical and Physical Sciences for Advanced Materials and Technologies (MPHS) from Scuola Superiore Meridionale (SSM), University of Naples Federico II, Italy. He conducted his research work at the Department of Physics "E. Pancini", University of Naples Federico II, Italy and the Catalan Institute of Nanoscience and Nanotechnology (ICN2), Barcelona, Spain under the supervision of Vincenzo Iannotti and Arben Merkoçi. Since 2017, he has focused on MXene research, with his current research activities involving the synthesis and post-processing of MXene inks to print electrochemical transducers for sensing and biosensing applications.*

**Vincenzo Iannotti**

*Vincenzo Iannotti is currently a professor at the Department of Physics "E. Pancini", University of Naples Federico II, Italy, where he received his PhD in 1999. His research interests focus on nanostructured magnetic materials and their applications, with emphasis on magnetic nanoparticles and magnetic composites for sensors and biomedical applications. He is currently working on the application of magnetic nanoparticles and 2D materials (MXenes) in biosensing.*

**Giulio Rosati**

*Dr Giulio Rosati is a senior postdoc researcher in the Nanobioelectronics and Biosensors Group at the Catalan Institute of Nanoscience and Nanotechnology (ICN2). Dr Rosati is a biomedical engineer with a PhD in Biotechnology, working on inkjet printing of nanofunctional inks for the fabrication of electronics and electrochemical devices and biosensors. Dr Rosati has an H-index of 12 and has published more than 30 scientific contributions. He has collaborated with and worked for several spinoffs, and he is interested in applications ranging from biomedicine to environment protection and agriculture.*

**Raffaele Velotta**

*Raffaele Velotta is presently a professor of physics at the University of Naples Federico II, where he obtained his PhD in 1992. For several years, his research focused on laser physics, nonlinear optics, and ultrashort pulse generation. In the last ten years, he has devoted himself to biosensing with particular focus on the realization of immunosensors (piezoelectric, electrochemical and optical) for detecting toxic molecules, proteins and bacteria. His current interests include immunosensors based on nanostructured surfaces (plasmon enhanced fluorescence) and magnetic nanoparticles.*

MXenes can be produced in various forms, such as clay and thick slurries, and can be easily rolled into desired shapes. MXene inks offer excellent compatibility with a wide range of printing techniques and surfaces. MXenes also demonstrate liquid crystalline behavior at higher concentrations, showing great potential for electronic displays, smart glasses, thermal camouflage devices, sensing and tribology.[18] Metal-like conductivity of MXenes makes them an important material for applications such as electrochemical sensors, wireless antennas and actuators for soft robotics, among others.[19] Their chemically active surface subsequently provides control over various critical factors in biomedical applications, such as tuning cell–material interactions, external functionalization for biosensing, theranostics, drug delivery, and controlled release.[20] MXenes also exhibit redox-active properties that are highly beneficial for catalysis and numerous sensing applications.[21,22] Although they lack semiconducting bandgaps similar to those of TMDCs, MXenes exhibit photothermal properties and possess light-to-heat conversion capability, which is useful in photothermal cancer therapy.[23] Furthermore, their optical functionality within the near-infrared II biowindow enables high-resolution imaging.[24] Such nuanced features of MXenes have transformed contemporary trends in healthcare research, heralding an era of advanced nanomaterials.

In this review, we discuss the versatile features of MXenes and highlight their potential in healthcare applications. We demonstrate MXene synthesis from a laboratory standpoint, primarily focusing on the acidic etching routes and the intercalation–delamination phase. We present laboratory modules along with a detailed explanation of the underlying science of the synthesis procedures. The synthesis of MXene composites has been explained in a similar manner. Such an approach connects experimental synthesis and laboratory observations with underlying scientific reasons (aided by atomistic descriptions), effectively filling the current gap in learning/understanding MXene synthesis. We strengthen this relationship by providing a detailed analysis of computational studies and correlating their outcomes with experimental part, thus offering a thorough understanding of the topic, which effectively distinguishes this review from others.[2,16,17,25–31] Furthermore, we provide a similar relationship to understand MXenes' properties, MXene–water interaction, and the role of terminations in determining its stability.

Then, we explore the potential of MXenes in diverse healthcare applications, such as nanocarriers for drug delivery and vectors for gene therapy, and discuss their roles in sensing, bioimaging, therapeutics, regenerative medicine, and wearable technologies. It also includes the role of MXenes as an effective tool for immune profiling, single-cell detection, and the applications of MXene-based technologies as bioelectronic implants, thus providing a forward-looking perspective on MXene research. Note that MXenes exhibit a robust structure–property relationship, with their performance (or physicochemical nature) influenced by numerous factors. As MXenes are typically customized prior to use in these applications to ensure effective functionality, it is equally important to identify which parameters should be included and to what extent in MXene-based materials to make them suitable for medical applications. In this review, we thoroughly examine common strategies for tailoring MXenes and explicitly discusses the role of each

**Ruslan Álvarez-Diduk**

*Dr Ruslan Álvarez-Diduk obtained his PhD in chemistry from the Universidad Autónoma Metropolitana (México) in 2014. From 2015 to date, he has worked as a senior postdoctoral researcher in the Nanobioelectronics and Biosensors group (Prof. Merkoçi). His research focuses on the development of novel nanostructured biosensors using both optical and electrochemical platforms, which are based on point-of-care and low-cost systems. He is also involved in exploring new and novel routes for nanoparticle synthesis, graphene reduction and laser patterning, and the development of readout platforms including smartphone based biosensing.*

**Arben Merkoçi**

*Arben Merkoçi is an ICREA Professor and the director of the Nanobioelectronics & Biosensors Group at the Institut Català de Nanociencia i Nanotecnologia (ICN2). Prof. Merkoçi's research focuses on the design and application of cutting edge nanotechnology and nanoscience based cost/efficient biosensors. The paper/plastic-based nanobiosensors involve the integration of biological molecules (DNA, antibodies, cells and enzymes) and other (bio)receptors with micro- and nanostructures/motors and are applied in diagnostics, environmental monitoring or safety and security. He has published around 350 peer review research papers, supervised 35 PhD students and has been invited to give plenary lectures and keynote speeches on around 200 occasions in various countries. He is the Co-Editor In Chief of Biosensors and Bioelectronics and a member of the Editorial Board of other journals. He is the co-founder of two spin-off companies, PaperDrop dedicated to nanodiagnostics and GraphenicaLab focused on electronic printing.*

involved parameter and the extent of its impact on MXene performance, which is another novel aspect of this review. Aided by ESI,† we connect all the critical aspects essential to learn/understand MXenes, thus providing a complete guide for young researchers.

Followed by a spectrum of healthcare applications, the final sections discuss the role of artificial intelligence (AI) technologies in accelerating MAX discovery (synthesizability of MAX), predicting synthesizable phases (exfoliability of MAX to MXene), and identifying favorable features, such as high stability. In addition to AI-integrated MXene applications, we highlight the correlation between the theoretical approaches and AI-based models for predicting the optoelectronic properties of the entire MXene database. In the current era of AI technologies, this integration represents a rapidly advancing frontier in materials science, thus presenting another novel aspect of this review as compared to others.[2,16,17,25–31] Finally, this review also provides valuable insights into the potential limitations of MXenes by comparing them with other 2D materials and offers guidance to future researchers and graduates aiming to unlock the full potential of MXenes in healthcare technologies.

## 2. Elementary characteristics of MXenes

MXenes are generally obtained from the MAX phase, which is the primary precursor for their synthesis. MAX phases, represented as $M_{n+1}AX_n$, are a class of three-dimensional (3D) layered structures with transition metal atoms, principally from groups 3–6 of the periodic table (3d–5d block elements), A-group elements (from group IIIA or IVA), "X" represents carbides (C), nitrides (N), or carbonitrides (CN) and "$n$" describes the number of layers. In MAX phases, MA shares a mixed covalent/ionic/metallic bond, whereas MX shares only a metallic bond. Owing to the difference in relative binding strengths, it is possible to selectively remove the A layers. The removal of A weakens the interlayer bonding, causing the layers to separate and results in a 2D layered morphology termed as MXenes.[32] Because there are very few atomic layers in a single MXene stack, its thickness is typically less than 1 nm. However, its lateral dimensions can vary from nanometres to microns depending on the production method and size of the MAX precursor.

MXenes are denoted as $M_{n+1}X_nT_x$, where $T_x$ denotes the functional groups appearing on the outer M-layers after chemical etching. $T_x$ can vary depending on the selected synthesis method. Fluoride-containing acid routes render =O, –OH, –F groups, and –Cl (predominantly in the HF + HCl route). MXenes have a $P6_3/mmc$ space group symmetry, and from a crystallographic viewpoint, they have a hexagonal crystal structure where "X" elements are closely packed with M elements, residing at the octahedral interstitial sites of the M sub-lattice, and thus coordinated with 6 M atoms. This explains why the MX structure remains intact even during harsh acidic etching. Furthermore, surface terminations occupy different thermodynamically favourable sites. $Ti_3X_2T_x$, $Ti_2XT_x$, $V_2XT_x$, $Nb_2XT_x$, and $Nb_4X_3$, where X=C and/or N, $T_x$ = –OH, =O, –F, *etc.*, are common examples of experimentally synthesised mono-transition metal MXenes. Hence, MXenes offer versatility in composition because varying the transition metal "M", X elements, terminal groups "$T_x$" and number of layers "$n$" can lead to a wide range of materials. Examples include double-ordered transition metal (DTM) MXenes, in which two different transition metal atoms coexist in the same MXene structure, but with two different atomic orderings, *e.g.*, in-plane ordering (i-MXenes) and out-of-plane ordering (o-MXenes). Also, the random atomic arrangements of M elements and $T_x$ distributions lead to high-entropy counterparts.[33] Excluding solid solutions and computationally discovered phases, recent studies have suggested that more than 50 different compositions of MXenes have been experimentally synthesized. The surface functional groups of MXenes can be tailored to achieve specific functionalities, thereby enhancing the versatility of MXene structures. The surface chemistry of MXenes also imparts diverse redox behaviors, which are beneficial for electrochemical sensing. As discussed previously, easy solution processing of MXenes[34] and the possibility of additive-free functionalized inks allow the use of various printing techniques to fabricate electronic devices,[35,36] wearable E-skin[37] and bioelectrodes.[38] Unlike graphene and other related 2D materials, the synergistic combination of metal-like conductivity ($\sim$20 000 S $cm^{-1}$), and optical versatility confers intriguing optoelectronic properties. Intrinsic hydrophilicity (due to a negative zeta potential of below −30 mV) imparts a colloidal nature to MXenes (without aggregation in various aqueous and organic solvents). Other attributes include larger lamellar surfaces that assist redox activity, drug or growth factor loading,[39] antimicrobial properties,[40] size-dependent physical (photophysical) properties,[41] and enzyme-mimicking capabilities,[42] further enhancing their utility in biosensing, drug delivery, tissue engineering, therapy, and wearable medical devices. In particular, the exceptional electrical conductivity of MXenes makes them a suitable alternative material for neural and cardiac tissue regeneration. MXenes are distinguished from other carbon-based 2D materials because of their higher extinction coefficient ($\varepsilon$), which allows for robust absorption in the near-infrared (NIR) region with minimal radiative decay.[43] These characteristics, combined with exceptionally efficient light-to-heat conversion (high photothermal conversion efficiency),[44,45] highlight their potential as superior photothermal agents for photothermal therapy (PTT) for cancer hyperthermia and *in vivo* photoacoustic imaging (PAI) within NIR-I/NIR-II biowindows.[24] Paramagnetic MXenes enable artifact-free high-field magnetic resonance (MRI) and computed tomography (CT) imaging,[38] whereas modified MXenes show exceptional potential for MRI and photothermal therapy (theranostics).[46] Similarly, MXenes with high-atomic-number elements exhibit remarkable X-ray attenuation for CT imaging and efficient photothermal conversion, making them highly promising for theranostic applications.[47] Furthermore, the possibility of diverse extrinsic modifications and composite/hybrid formation offers additional customization for healthcare applications.[39] MXene uniquely converts noble metal salt solutions into corresponding nanoparticles (NPs), making this approach rapid, safe, and cost-effective, while maintaining MXene quality. Conversely, positive charges appeared at the edges of the $Ti_3C_2$ MXene flake.[48] This difference between the surface and edge charges introduces new properties, enabling distinct functionalizations at the edges compared to the surface. Combined with the above-mentioned interesting features, and a straightforward and scalable manufacturing process, these characteristics differentiate MXenes from other 2D materials. Furthermore, there are several other methods to modify MXene surfaces and fine-tune their properties for specific healthcare applications, which are discussed in the following sections.

## 3. MAX to MXenes: atomistic insights and laboratory guide

The following section explicates the synthesis of MXenes and divided into three parts. It begins with a brief atomistic perspective of etching, followed by intercalation–delamination procedures and monolayer synthesis. In the subsequent part, laboratory protocols are demonstrated, and critical observations and instructions are highlighted explicitly. Ways to quickly access MXene synthesis in the laboratory and many important factors (*e.g.*, oxidation, MXene films, surface chemistry and solution processing) are provided in the supplementary information I (ESI†). A mechanistic interpretation of etching and delamination is provided alongside the laboratory protocol to enable a deterministic understanding, thereby enhancing the tutorial aspects.

### 3.1. A brief atomistic view

Unlike graphene, where van der Waals interactions are prominent among the graphite layers, the metallic interactions between MA bonds in the MAX phase inhibit its mechanical exfoliation. Therefore, wet chemical routes are primarily employed for MXenes. Other methods include molten salt, halogen, alkali, and electrochemical etching. Variations in the etching conditions can yield different degrees of exfoliation, resulting in varying flake sizes, morphologies, surface terminations, and properties. For simplicity, the procedure for extracting MXene flakes from MAX phases can be understood by dividing this process into three stages.

**Pre-etch washing:** This phase involves Al–$Ti_3AlC_2$ (a MAX phase with a higher stoichiometric ‘‘Al’’ content), where the MAX phase is immersed in hydrochloric (HCl) acid (Scheme 1, part 1). In this process, intermetallic impurities are dissolved in HCl and subsequently washed away. Pre-etch washing has also been reported for $V_2AlC$ (Table 2).

**Leaching of ‘‘A’’ layers:** This phase, known as ‘‘etching’’, involves the selective elimination of the interleaved ‘‘A’’ layers to produce multilayered MXenes (ml-MXenes). Typically, the wet chemical route employs strong etchant solutions, such as fluoride-containing acids (*e.g.*, HF, HF/HCl, and LiF/HCl). The ‘‘A’’ layers react with fluoride-containing acids, facilitating their selective removal from MAX precursors and leaving behind the desired ml-MXene. The efficiency of removing the ‘‘A’’ layers is influenced by the Gibbs free energy of the etching reaction. In the case of HF etching, the Gibbs free energy is related to the relative strengths of the M–A and M–X bonds in the MAX phase

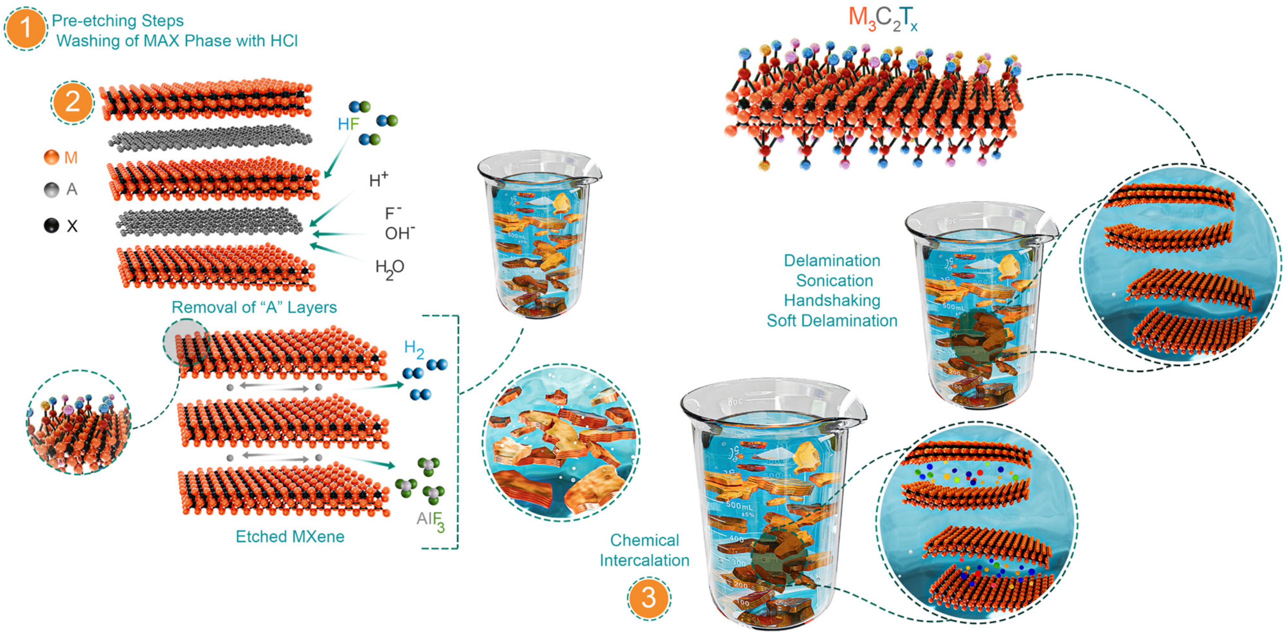

Scheme 1 Step-by-step atomistic insight into MXene synthesis.

(further explained in Section 3.4.2.1). For etching to occur, the "A" layers must be oxidised and converted into a soluble byproduct, which can be easily washed away.[49] Notably, for Al-based MAX phases (*e.g.*, $Ti_3AlC_2$), HF interacts with outer "A" atoms, where $H^+$ oxidises Al to $Al^{3+}$, and $F^-$ from HF acids converts oxidised $Al^{3+}$ to soluble $AlF_x$, which can easily be removed during washing (Scheme 1, part 2). Such ligand interactions are crucial for producing soluble species; otherwise, by-products may remain at the initial reaction sites as oxidized or hydrolysed species, impeding further etching of the inner "A" layers.[50] Therefore, the etchant solution should be strong enough to effectively dissolve the oxide layers and ensure effective etching. This also helps the etchant solution to gradually access the inner atoms, propagating stepwise exfoliation. Additionally, this process generates $H_2$ gas, which is observed as bubbles within the reaction vessel. In other etching routes, *e.g.*, electrochemical oxidation of Al, its subsequent removal is possible in the presence of –OH and/or –Cl ligands. Similarly, etching of non-Al MAX phases (*e.g.*, $Ti_3SiC_2$) requires multiple oxidants,[51] such as $HNO_3$ or $H_2O_2$, in addition to HF, due to the strong Ti–Si bonds. Nevertheless, depending on the synthesis route, etching terminates the outer M layers (top and bottom) with randomly distributed functional groups. These groups provide a negative charge to the flake surface (ζ-potential) and impart hydrophilic characteristics. The surface chemistry of MXenes is a crucial distinguishing feature compared to other 2D materials and provide additional opportunities to tune their properties.

**Intercalation and delamination:** During the etching phase, stronger M–A bonds are substituted by weaker hydrogen bonds and facilitate the insertion of external agents into the interlayer galleries. These external molecules, known as intercalants, further weaken their bonds, resulting in single-layered MXene (sl-MXene) or few-layered MXene (fl-MXene). This process is known as intercalation-assisted delamination (Scheme 1, part 3). The introduction of the host species can initiate ion exchange with the flake surface, change the surface environment, and catalyse this delamination. Flake isolation can be achieved through methods such as shaking (including hand-shaking and vortex shaking), sonication, or straightforward collection by centrifugation. Delamination is also possible without shaking or centrifugation by a technique known as soft delamination.[52] In all cases, it is important to consider that sonication, shaking, and/or soft delamination yield MXene flakes with different sizes, defect densities, and chemistries.

### 3.2. Laboratory guide

During the experimental synthesis of MXenes, each stage of production requires thorough consideration. Starting with MAX phases, which are the primary precursors of MXenes, the choice of constituent elements (*e.g.*, M, A, and X) determines the processing conditions of MAX phases and their resulting properties. Hence, each step must be executed carefully. In the following sections, we divided the laboratory production of MXene into several stages: synthesis of the MAX phase and washing with HCl (which is necessary for excess aluminum MAX phases), wet chemical etching, intercalation–delamination, washing procedures, flake collection, and concentration control. For clarity, we include laboratory modules for each stage to illustrate the experimental setup with associated mechanistic understanding.

**Instructions for readers**

In Section 3.2, the parts labelled as phase-1, phase-2, phase-3 and phase-4 are categorized as follows and should be read in the given order.

(1) **Preliminary context:** This section discusses the important background before proceeding with the experiments.

(2) **Laboratory guidelines (boxes):** This section provides a pedagogical demonstration of the laboratory aspects, along with essential instructions, and critical points to be considered while working in the laboratory.

(3) **Mechanistic insights:** This section connects experimental aspects to theoretical underpinnings for a holistic understanding.

**3.2.1. (Phase-1) MAX synthesis and pre-etch washing.** Preliminary context: the quality of MXenes is affected by their parent MAX phases. Therefore, thoroughly controlled synthesis of MAX phases with controlled stoichiometry, high crystallinity, and minimum oxygen impurities needs to be assured. It is suggested to analyse the crystallinity of raw materials used in the synthesis of MAX powder and the final synthesized MAX phase should be investigated by XRD measurement and Rietveld refinement of the obtained patterns at every step. The classification and synthesis of MAX phases involve several factors that are not detailed here and can be accessed in ref. 53. Briefly, the synthesis of MAX phases involves mixing raw metal precursors (*e.g.*, Ti, Nb, Mo powder, *etc.*), "A" layer powders (*e.g.*, Al, Si, *etc.*), and carbon precursors in specific molar or mass ratios followed by reactive high-temperature sintering in an argon-filled tube furnace.[54] The stoichiometric ratios (Table 1) significantly influence the *n* values in the MAX phase and subsequently determine the thickness of the resulting MXenes. To enhance the stability of MXenes in environmental settings, MAX phases with excess Al-content (Al–$Ti_3AlC_2$) represent a significant advancement.[55] In this case, it is necessary to wash MAX with HCl for a specific period (12 h to 18 h depending on the particle size of the MAX powder) at room temperature to dissolve the intermetallic impurities, which are then removed in the subsequent washing steps.

**3.2.2. (Phase-2) etching.** Preliminary context: This conversion of MAX to MXene depends on several factors including the size of the MAX particles, reaction conditions (such as time and temperature), the type and concentration of the etchant solution. Additionally, three main parameters affect the size of the MXene flakes: the size of the MAX phase crystals, complete or partial etching of MAX phase, and the degree of delamination into isolated flakes.

*3.2.2.1 Mechanistic insights into etching.* There are several factors that effectively determine the etching procedures. Specifically, in HF-based scenarios, changing the type of etchant and/or increasing the HF concentration plays a crucial role. For example, higher concentrations can reduce the required

### Phase-1 laboratory guidelines

The experimental setup for MAX-phase production is illustrated in Scheme 2-i. It details all the steps of MAX phase production, such as mixing of MAX precursors, which is typically performed *via* ball milling (18 h, 60–70 rpm for $Ti_3AlC_2$ MAX), followed by successive annealing in a tube furnace (time: 2–4 h, temperature: 1380–1400 °C, and ramp rate: 3.5–4 °C $min^{-1}$ while maintaining continuous supply of argon).[56] After cooling, the synthesized crystalline MAX bar is ground using a drill machine to obtain fine powder, which is sieved according to the required size (generally 400 mesh sieve size is used to get particles of size 38 μm) and collected for HCl washing. The MAX phase is gradually added to a beaker containing 9 M HCl (10 ml/1 g of MAX) to dissolve the intermetallic impurities[i]. Since the addition of the MAX phase is exothermic, an ice-bath should be used throughout the process and the mouth of the beaker should be kept open to allow for gas discharge (Scheme 2-ii). Intense bubbling can occur, so reduce the stirring and control the rate of MAX addition if necessary. Once all the MAX phase is added, allow the reaction to proceed for the anticipated time (12–18 h).[56] Washing is performed to remove dissolved impurities from the etchant solution *via* repeated centrifugation (Scheme 2-iii). A deep purple supernatant is observed with Al–$Ti_3AlC_2$ during the initial washing cycles, which gradually fades with the washing cycles, indicating complete removal of impurities[ii]. Once a neutral pH is achieved, the sediment is filtered through vacuum filtration and dried under vacuum and then crushed into powder (Scheme 2-iv). Now, the MAX phase production is complete, and it is ready to be converted to 2D MXene ($M_{n+1}X_nT_x$), as discussed in the next section.

**Phase 1-critical point**

(i) This step should be performed in a fume hood.

(ii) One critical aspect is that the supernatant in the initial washing cycles may exhibit distinct colours according to the MAX type and intermetallic impurities. The absence of chromatic behaviour can be correlated with the absence of intermetallic impurities, which are common in typical $Ti_3AlC_2$ MAX phases (if carefully synthesised).

### Phase-2 laboratory guidelines

In this procedure, MAX is added to the etchant solution and stirred using a magnetic stir bar for a specific duration. Depending on the intended MXene and etching route, the etchant solution may vary. The reaction time, temperature, type, and concentration of the etchant also play important roles (see Table 1). For $Ti_3C_2T_x$, HF, HCl + LiF, and $H_2O$/HCl/HF mixtures are frequently employed. As an example, we take the mixed acid route, *i.e.*, $H_2O$/HCl/HF (9 mL : 18 mL : 3 mL or 6 mL : 12 mL : 2 mL volume ratio for 1 g of $Ti_3AlC_2$)[iii]. This approach is relatively safer because of the lower amount of HF acid used, and also yields good quality MXene.[56,59] The MAX powder is added at room temperature or even the reaction vessel is placed in an ice-bath[iv]. Once the addition of the MAX phase is complete, it is moved to the oil bath and set the temperature at 35 °C. The MAX phase must be added slowly to the etching solution to avoid overheating, and the mixing speed should be low to avoid possible splashing. After MAX addition, the reaction bottle is sealed[v], and stirring is maintained for 24 h at 300–400 rpm (Scheme 3-i). Once the reaction is complete[vi], the etching mixture is transferred to a centrifuge bottle[vii]. Washing is performed *via* centrifugation until the pH becomes close to 6–7 (Scheme 3-ii). Use a pipette to draw the supernatant for pH control[viii]. Once the pH is neutral, the sediment is filtered out (Scheme 3-iii). Depending on the application, the etched MXene cake (ml-MXene) can be dried and stored. If delamination is intended, drying is not recommended. In dried ml-powders, the deintercalation of water reduces the interlayer spacing, thus reducing the ion mobility into interlayer galleries and decreasing the delamination yield. Without drying, a high yield of delaminated flakes can be obtained. Note that it is unlikely that all the MAX phase is etched into MXene, and there exists a certain amount of unreacted MAX.

**Phase 2-critical points**

(iii) Using HF-compatible reaction bottles, such as those made from Neglane, PTFE, or HPPE, is also recommended. The reaction should be conducted in a fume hood due to the hazardous nature of HF, which can cause severe tissue and bone damage. At concentrations above 50%, HF causes rapid and severe pain, burns, and blisters, while at concentrations below 20%, symptoms may be delayed up to 24 hours. HF fumes are harmful and can damage the respiratory tract and eyes. Personal protective equipment (PPE) such as acid-resistant gloves, face shields, masks, aprons, closed-toe footwear, and safety goggles are essential.[65]

(iv) To avoid overheating, use of an ice-bath in the first step can be beneficial.

(v) It is better to create a condenser to trap the vapours (preferred for long reactions, such as $Nb_2CT_x$ MXene) and discharge the gas buildup. It is better to use a pipette: cut the bulb in half and pass the narrow end of the pipette through the hole in the lid. The half-cut bulb should be inside the lid.[56]

(vi) It is recommended that the reaction vessel be removed from the oil bath and gently fixed on top. Thus, the oil sticking to the side of the bottle can fall back into the bath, and the mixture has enough time to cool down.

(vii) Do not turn off the hot plate and keep the temperature at 35 °C, as it will be required for the delamination phase (if you are following 24 h delamination). If not, set the temperature to 65 °C. In this case, the delamination time is 1 h.

(viii) PPE is recommended during the initial washing cycles, because the supernatant is highly acidic.

etching time and produce flakes with an accordion-like composition (larger c-LPs). Conversely, lower concentrations of HF or mixed acids with low HF contents may require longer etching times, potentially leading to variations in morphology such as the usual accordion-like morphology is difficult to observe. Quantitatively, low HF concentrations such as 5 wt% can significantly remove Al, but an accordion-like morphology is evident when HF concentrations of 10 wt% or more are used.[64] In short, the so-called accordion-like morphology of ml-MXene is associated with the use of pure HF method. The frequently used LiF + HCl and HF (at varying concentrations) exhibit different kinetics and degrees of exfoliation. Initial investigations revealed that increasing the temperature, etching period and decreasing the particle size accelerated the conversion of MAX to MXene.[66] Therefore, a longer etching time or the need for a stronger etchant becomes crucial for MAX phases with large particle size. However, recent investigations reported that the MAX particle size has less influence on the etching time; rather, the temperature and etchant composition/concentration are more significant factors. Kinetic curves (amount of exfoliation *versus* time) in Fig. 1a demonstrate that the synthesis time can be significantly reduced to a few hours by slightly increasing the temperature, switching the etchant solution to $NH_4HF_2$, and/or regulating the HF concentration.

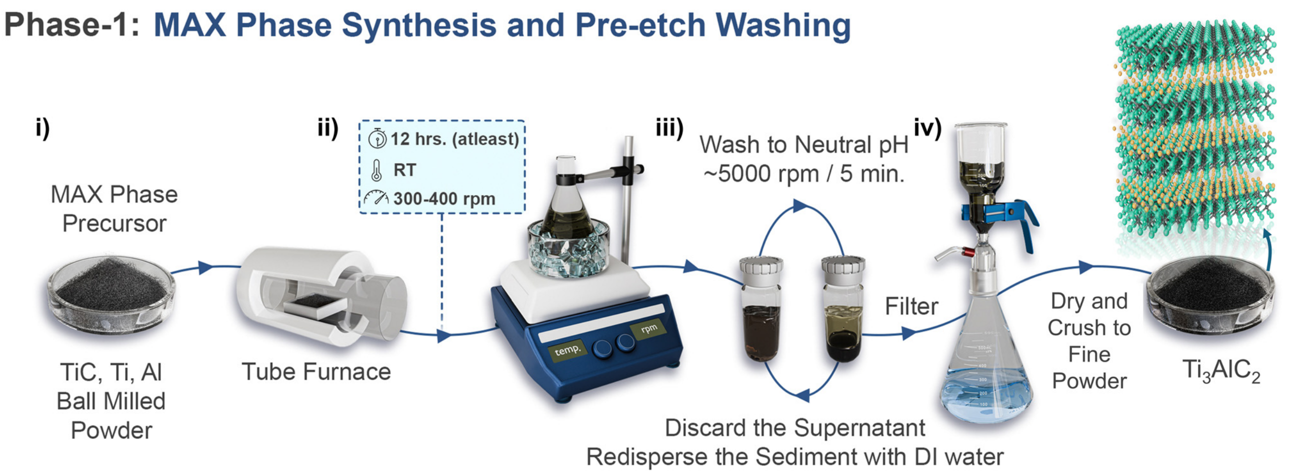

Scheme 2 (i) Schematic of the laboratory setup used for synthesis of MAX phase. (ii) Experimental setup and parameters required for pre-etch HCl washing. (iii) Depiction of repeated centrifugation for pH control. (iv) Depiction of the vacuum filtration assembly to collect the MAX powder.

Regardless, etching of MAX is not immediate or constant throughout the reaction, but a diffusion-limited process. Instead of etching all the A layers simultaneously, it occurs kinetically in a stepwise manner,[67] divided into the following series of events. (i) Activation, where etching is not initiated; (ii) steady state, where etching occurs but MAX is still under-etched; (iii) completion, where full conversion of MAX-to-MXene occurs; and (iv) over-etching, characterised by defects or formation of byproducts, such as oxides, fluorides, or hydroxides (Fig. 1b). Typically, for HF-based routes, etching begins from exposed ''Al'' atoms and/or macroscopic defect sites and proceeds towards the inner regions of the MAX particles with increasing etching depth until complete etching occurs (Fig. 1c).[67,68] Studies suggest that the process of Al removal initiates differently according to the type of etchant used. For example, the etching of $Ti_3AlC_2$ starts at the outermost exposed surface in the LiF + HCl route, whereas it begins along the grain boundary when HF is used as an etchant (Fig. 1d). Particularly, in the LiF + HCl route, the etchant does not directly interact with all the ''Al'' layers at once (especially the inner particles) because of the limited space and inaccessibility of the etchant. So, interrupting the reaction before the specified time or using a lower LiF concentration can lead to partially or non-etched MAX particles. Conversely, HF breaks down polycrystals into single crystals along the grain boundaries (in a direction perpendicular to the basal plane), gradually exposing more ''Al'' sites and accelerating the etching process. This allows more ''Al'' atoms in the newly exposed areas to be etched and over time, almost all MAX particles are converted into MXene (Fig. 1d). The higher initial concentration of HF in the pure etchant compared to that in LiF + HCl allows for greater etching strength, penetration into individual grain boundaries, and breaking of polycrystalline grains into single-crystalline particles. Hence, the HF method is believed to be a more efficient etching route than the HCl + LiF method. Also, the LiF + HCl etchant can leave polycrystalline particles unbroken (at low LiF concentrations) and requires sonication to increase the yield. This kinetically controlled procedure may

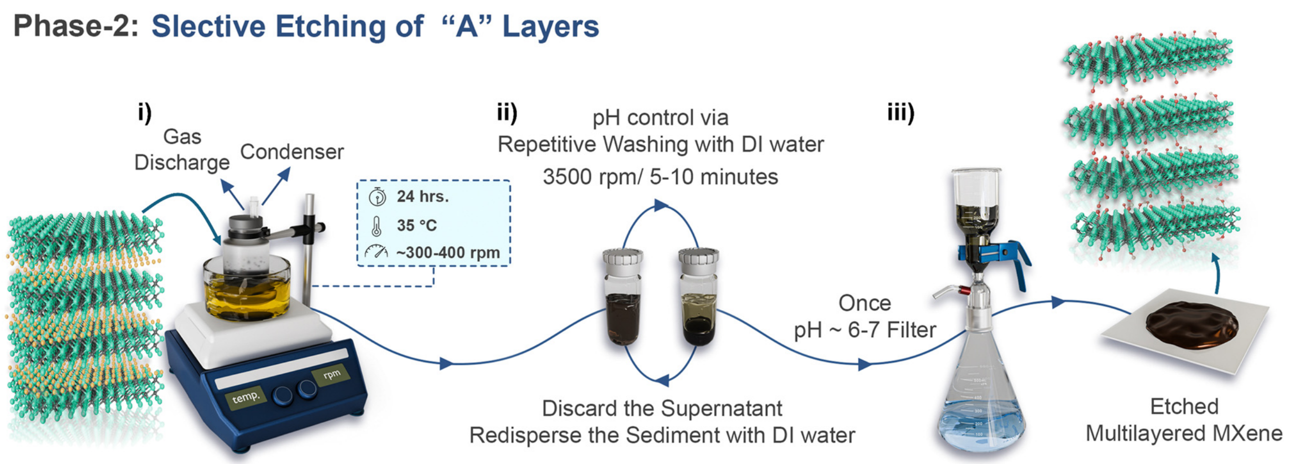

Scheme 3 (i) Laboratory settings typically followed for etching (ii) washing procedure for pH control. (iii) Depiction of the filtration assembly and as-etched MXene cake obtained after filtration. Note: this method is universal for almost all MAX phases etched *via* the wet-chemical route.

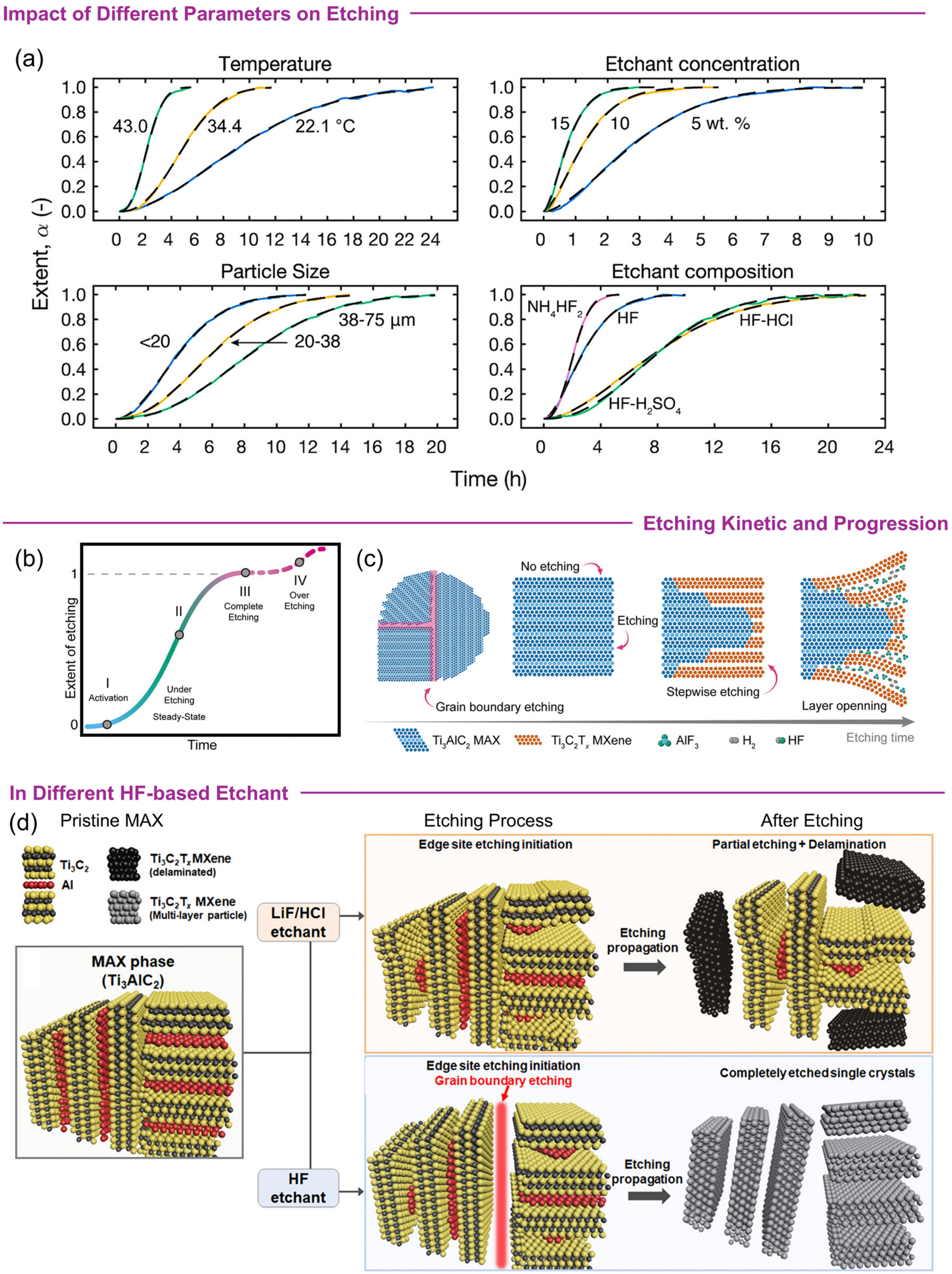

**Fig. 1** (a) Kinetic curves (amount of exfoliation *versus* time) for $Ti_3AlC_2$ MAX etching. (b) The kinetic curve showing different events taking place during chemical synthesis of MXene. (c) Illustration of the etching procedure showing stepwise etching propagation, beginning at the edges along the basal planes and progressing gradually to the inner particles. Reproduced with Permission from ref. 67 Copyright © 2022, American Chemical Society. (d) Etching mechanism of mono-aluminium in different etchants (LiF/HCl and HF) showing distinct etching mechanisms for each. Reproduced withr Permission from ref. 68 Copyright © 2022, American Chemical Society.

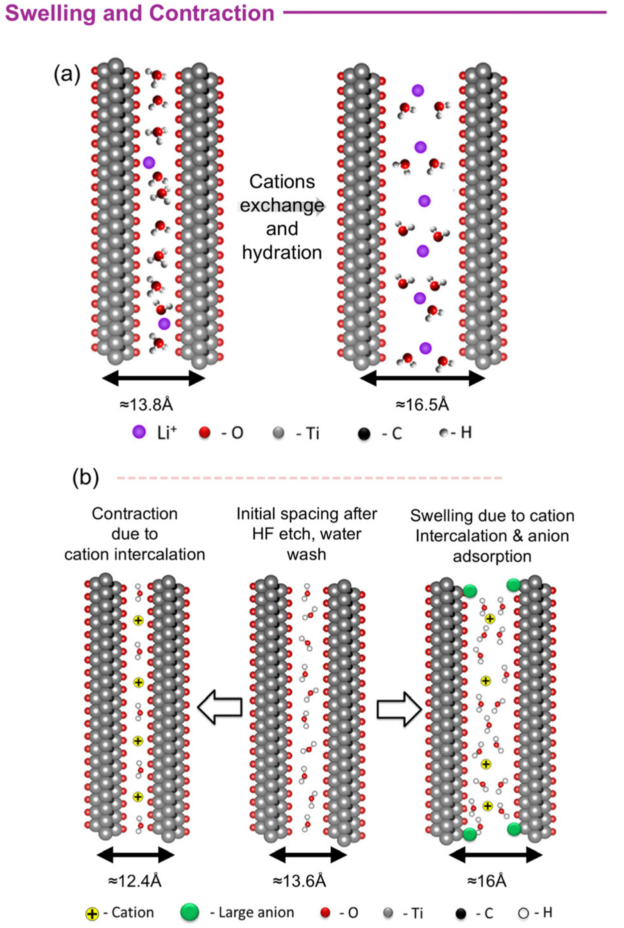

Fig. 2 (a) The atomistic mechanism of clay swelling suggests that cationic exchange occurs after $Li^+$ insertion (excess $Li^+$ ions in water substitute for $H_3O^+$ ions) and causes swelling. Reproduced with Permission from ref. 69 Copyright © 2019, American Chemical Society. (b) Mechanism of cation adsorption on the MXene surface suggests a decreased *d*-spacing (left). Anions preferentially adsorb on the edge, facilitate the further diffusion of $M^{x+}$ ions, and increase the *d*-spacing. Reproduced with Permission from ref. 70 Copyright © 2018, American Chemical Society.

explain the expected longer etching time for the dense MAX-phases and the variations in the flake size of the resulting MXene. In contrast, MXene produced through LiF + HCl shows a larger interlayer spacing than that of HF due to spontaneous delamination of $Li^+$ insertion during the etching process. In short, the influence of MAX selection and etching pathways on the nature of MXenes highlights the complex and interconnected nature of its synthesis.

**3.2.3. (Phase-3) intercalation and delamination.** Preliminary context: intercalation is a critical step in the MXenes' delamination. This process involves the insertion of various organic/inorganic and metal ions within the sheet network. Notably, the delamination approach varies depending on the MAX etching route since a method effective for one etching route may not work for others. In addition, the selection of an intercalant is also strongly correlated with the MXene type, as every MXene hosts a different intercalating agent[49] (Tables 1 and 2). For example, even for the same MXene, $Ti_3C_2T_x$, the etching method notably determines this choice. Such as, the interaction of bulky organic molecules ($TMA^+$/$TBA^+$ ions) is possible only for HF etched ml-MXenes.[49] This is due to their prominent accordion-like morphology that can effectively accommodate large molecules within expanded interlayer galleries. In contrast, ml-MXenes obtained *via* the HF + HCl method can only be delaminated with LiCl (*i.e.* $Li^+$ ions) due to the accessible spacing for $Li^+$ ions and the presence of –Cl terminations.[70,71] This supports the need for a suitable combination of etching and intercalation–delamination approaches. Meanwhile, MXenes produced by *in situ* techniques, (*e.g.*, HCl + LiF) do not require additional steps for delamination because $Li^+$ ions intercalate during the etching process, spontaneously assisting the delamination process. In this approach, sonication might be required in subsequent steps to increase the yield, as reported in the literature.[64] Predominantly, the choice of intercalant determines the physicochemical properties of the resulting MXene and influence its application performance.

Once the intercalation phase is complete, the mixture is transferred to a centrifuge tube and washing is performed.

**3.2.4. (Phase-4) washing and collection of delaminated MXene.** Preliminary context: in delamination, intercalants push the layers apart, causing noticeable swelling during subsequent washing. The expansion (swelling) of the intercalated-MXene sediment is an important indication to observe. This kind of swelling is more obvious in ml-$Ti_3C_2T_x$ and DTM MXene sediments. During the collection of delaminated MXenes, once can observe two distinct phases at the bottom corners of the centrifuge tube: a dark black slurry and a grey sediment.[64] The black slurry likely contains swollen ml-$Ti_3C_2T_x$, while the grey sediment is unetched MAX. Hence, separation of sl-$Ti_3C_2T_x$ flakes from the sediment requires additional centrifugation cycle.[54]

Besides that, soft delamination is another method to obtain flakes with large lamellar dimensions.[52] These techniques differ in the mechanisms as it doesn't involve sonication or shaking and have different control and scalability. Similar to the selection of a suitable intercalant, the processing steps to obtain delaminated MXene also influence the lamellar structure and surface chemistry. So, a careful selection and tuning of these parameters is crucial. Certainly, all these characteristics provide exceptional control and tunability but also presents a challenge in understanding the associated complexity and interplay among these factors.

For simplicity, this phase is divided into three stages, each provided with relevant schematics. (a) Washing: primarily to remove unreacted Li and further delamination. (b) Collection of delaminated MXene, and (c) concentration control according to the required application.

*3.2.4.1 Mechanistic insights into intercalation–delamination, ion-exchange and swelling.* As discussed previously, the stronger

### Phase-3. Laboratory guidelines

Intercalation of host molecules facilitates the delamination of multilayered MXene (ml-MXene). For $Ti_3C_2T_x$ MXenes and other Ti-based counterparts, lithium chloride (LiCl) is a commonly used intercalating agent (Table 1).

Typically, 1 g of LiCl is dissolved in 50 mL of deionized (DI) water for 1 g of etched-MAX[ix]:

(i) First, 1 g of LiCl is dissolved in 10 mL of DI water (Scheme 4-i). It is advisable to touch the bottle to check if the solution becomes warm, which confirms that LiCl has dissolved properly[x].

(ii) After dissolving LiCl, the remaining DI water is added and ml-MXene obtained in previous step is mixed (Scheme 4-ii). Stirring is maintained at 300–400 rpm to ensure uniform mixing under argon purging (Scheme 4-iii).

At this point, there are two ways to proceed further:

(i) Delayed delamination: the mixture is maintained at 35 °C for 24 hours.[59]

(ii) Quick delamination: the mixture is maintained at 65 °C for 1 hour. For this method, argon (Ar) bubbling is required[xi].[56]

**Phase 3-critical points**

(ix) Perform the reaction inside a fume hood.

(x) LiCl is highly hygroscopic and absorbs moisture from the air. Tightly close the LiCl container, secure it with Parafilm, and place it in a desiccator.

(xi) To prevent oxidation during quick delamination,[56] create two holes in the lid of the delamination bottle—one for vapor condensates and gas exhaust, and the other for the Ar inlet. Use a pipette for the Ar inlet by cutting the longer part, fitting it into the Ar supply pipe, and sealing it with parafilm strips. Adjust the pipette length to ensure it is adequately immersed in the solution. This can be done separately using another bottle containing the same volume of DI water to make adjustments easier and ensure uniform bubbling.

### Phase-4: washing; laboratory guidelines

*Initial steps:*

- Once the intercalation phase is complete, transfer the mixture to centrifuge tubes. The experimental conditions for the washing process are presented in Scheme 5a.
- Perform repeated centrifugation cycles[xii].

*Early cycles:*

- During the first few cycles, the supernatant is usually clear[xiii] and should be discarded into a waste container.
- The sediment is redispersed using DI water, and centrifugation is performed again until a dark supernatant appears[xiv].

*Later cycles:*

- Once the supernatant turns dark, increase the centrifugation time to 1 hour.
- After 1 hour, remove the supernatant.

*Final steps:*

- Add DI water to the sediment[xiv], mix well, and proceed to the next step (B).

**Phase 4a-critical points**

(xii) Keep in mind that the number of cycles can vary depending on the centrifuge system.

(xiii) Pipette out the supernatant to see the color. The transparent supernatant should be discarded. If it is not transparent, it means MXene has spontaneously separated into layers. Nevertheless, it includes residual LiCl and should be discarded.

(xiv) With each cycle, MXene converts to clay and adheres to the tube, making it hard to disperse. To ensure uniform dispersion, a glass rod can be used to mix the contents, and strong shaking (by hand or vortex machine) can be performed.

M–A bonds in MAX phases are replaced by the weaker hydrogen bonds during the etching process. Additionally, the surface environment allows intercalation and easier delamination into single/few layers. Although functional groups offer robust interlayer interactions, ml-MXenes, even with a hydrophilic surface, are difficult to delaminate with $H_2O$ alone. So, it requires the diffusion of polar solvents, organic/inorganic molecules, and metal cations/anions into the interlayer galleries, which can overcome the sluggish exfoliation kinetics. This insertion effectively weakens the bonding by forcing the layers apart and causing delamination of the stacked ml-MXene particles.[83]

In MXenes, the intercalation process behaves differently from typical layered materials such as graphite, where staging behaviour is usually prominent. MXenes exhibit structural similarities to clay minerals and demonstrate subtle ion-exchange, wherein ions within their structure can be replaced by those from the surrounding solution. So, their surface terminals and transition metal skeleton show layer rigidity identical to clays and exhibit interstratification behavior. But, the layers of atoms in MXenes tightly coupled, so the intercalation requires strong chemical interactions followed by ion-exchange behaviour.[84] Here, cationic exchange plays a vital role in both synthesis and post-processing of MXenes, profoundly influencing the structure–property relationship. Furthermore, it is closely linked to the surface environment, lateral size, and structure of the MXene flakes.[85] Such ionic exchange occur due to highly polar surface of MXenes that drives electrostatic attraction with guest cations, while maintaining electrical neutrality. Such cationic exchange offers

### Phase 4b: flakes collection; laboratory guidelines

This step is important to separate the delaminated MXene (sl-MXene) from the non-delaminated MXene (ml-MXene) and unetched MAX and any of the following strategies can be followed:

*Via repeated centrifugation:*

After completing the (previous) washing step, re-dispersed the sediment and centrifuge the solution at 3500 rpm for 10 minutes (see Scheme 5b).[82] Observe the supernatant using a pipette (Scheme 5b-i). It should be thick and dark black$^{xv}$. Collect this supernatant in a glass beaker$^{xvi}$. This supernatant is referred to as the first delamination$^{\dagger}$. Redisperse the sediment again, then centrifuge again at 3500 rpm for 10 minutes. Collect the supernatant as before. Continue this process until the supernatant becomes less concentrated or transparent. Variations in the color of the supernatant can be observed as shown in Scheme 5b-ii. All supernatants collected from each cycle constitute single-layer MXene$^{xvii}$.

*Alternative collection method:*

Use two centrifuge tubes for this approach (named $T_1$ and $T_2$). Take the redispersed sediment after 1 h step in a centrifuge tube ($T_1$) and centrifuge it at 3500 rpm/15 minutes. Instead of collecting the supernatant in a separate container, pipette it into another centrifuge tube ($T_2$). Centrifuge $T_2$ at 3500 rpm for 15 minutes and collect its supernatant. This supernatant contains single-layer MXene$^{\dagger}$. Discard the sediment from $T_2$$^{xviii}$. Return to $T_1$, redisperse the sediment with DI water, centrifuge at 3500 rpm for 15 minutes, and transfer the supernatant to $T_2$$^{xix}$. Centrifuge $T_2$ again, collect the supernatant, and discard the sediment. Repeat this process until the supernatant in $T_1$ becomes transparent.[59] While this method is more time-consuming, it generally produces higher quality MXene with minimal mixing of non-delaminated and unreacted MAX.[59]

Final sediment disposal: in both methods, the remaining sediment can be observed as two distinct layers: an upper dark layer containing swollen multilayered MXene and a lower gray layer of unetched MAX (Scheme 5b-ii). Redisperse and dispose of the sediment in a waste container.

**Phase 4b-critical points**

(xv) It is possible that the supernatant may not be dark. This means that the MXene is not delaminated effectively. Vigorous shaking (hand or vortex) for 30 minutes should be performed followed by centrifugation at 3500 rpm/10 minutes.[56] If the supernatant is still transparent or light green (in the case of $Ti_3C_2$), sonicate it for a couple of minutes and centrifuge at 3500 rpm/10 minutes. Sonication should be a last resort as it may produce smaller flakes. Vortex shaking is preferred for rapid delamination. For the LiF + HCl approach, longer sonication times are recommended, ideally in an ice bath with argon bubbling to prevent overheating and oxidation. Despite variations in techniques, the experimental setup remains consistent.

(xvi) Use a pipette to transfer the supernatant.

(xvii) It is recommended to further centrifuge the collected supernatant at 3500 rpm/10–15 minutes. Then collect the supernatant and discard the sediment. This is done to ensure removal of ml-MXene that may have been introduced during the initial collection cycles.

(xviii) The sediment is ml-MXene clay and should not be mixed with sl-MXene

(xix) It is recommended to use a new centrifuge tube.

(†) Visually check and assess the success of MXene synthesis by adding a small amount of delaminated MXene into enough DI water (explained in ESI-1†).

### Phase 4c: concentration control; laboratory guidelines

The MXene single layer obtained from the previous step should be purged with Ar and stored in a refrigerator ($<4$ °C). Also, the single layer of MXene can be converted into films by vacuum filtration and stored at room temperature after vacuum drying. If, the monolayer suspension need to be concentrated into a thick slurry, one can follow the concentration step (Scheme 5c). Here, centrifuge the single layer suspension at 1000 rpm/10 minutes (or 9000 rpm/30 minutes) and remove the supernatant$^{xx}$. The sediment will be a thick paste containing sl-MXene flakes. Additional washing can be performed to ensure the removal of any possible impurities. Now, the MXene can be transferred to storage containers. One may add DI water as per required concentrations$^{xxi}$.

**Phase 4c-critical points**

(xx) If the supernatant is not transparent after centrifugation, it indicates the presence of very small flakes that did not settle. Discard this supernatant and perform additional washing until the supernatant is clear.

(xxi) Add a measured amount of DI water to the sediment, mix thoroughly, and perform soft centrifugation (lowest possible rpms for 5 minutes) to ensure a uniform mixing of the content. Now pipette out the MXene to a storage container, seal it and store it under cold and dry conditions ($<4$ °C).

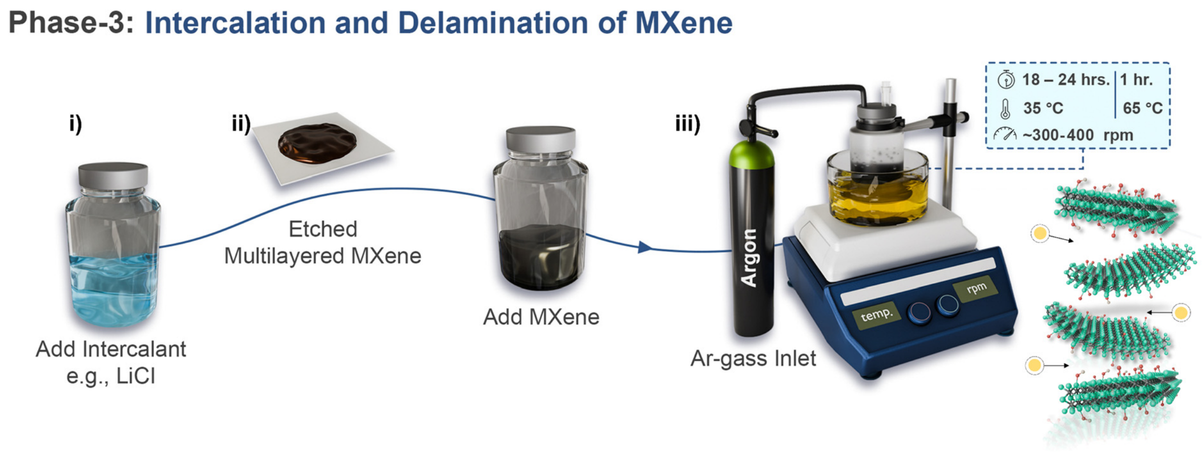

Scheme 4 (i) Depiction of LiCl addition to DI water. (ii) Mixing of the ml-MXene cake with LiCl solution. (iii) Laboratory setup and processing conditions.

Scheme 5 (a) Experimental settings for (i) initial washing cycles and (ii) 1 hour washing cycle after intercalation to remove unreacted Li ions. (b) Experimental settings for flake collection: (i) separation of delaminated flakes from non-delaminated MXene and unreacted MAX. This process is repeated many times until all delaminated MXene is collected. (ii) Colour change of the supernatant after each collection cycle. The dark supernatant in the early cycle indicates more MXene, whereas the clear supernatant in later cycles indicate delaminated MXene has been collected. The residue usually shows two different shades, indicating swollen ml-MXene and unreacted MAX. (c) Procedure for concentrating delaminated MXene.

possible crosslinking (preferable for extrinsic functionalization for specific biomedical or sensing applications). Similarly, the valence states of the M atoms in MXenes enable charge transfer and can facilitate the reduction of metal salts on the MXene surface (discussed in Section 3.5). Typically, MXenes exhibit a zeta potential of less than −30 mV at various pH values, which explains why positive metal ion intercalation accelerates sluggish exfoliation kinetics.

Table 1 For $Ti_3C_2T_x$ MXene: a catalogue on synthesis parameters (per gram) of well-known etching methods

| Fundamental aspects of MAX phases | | | | Experimental condition for wet chemical etching of $Ti_3AlC_2$ MAX phase | | | | | | | Production of isolated flakes | | | | | |
|---|---|---|---|---|---|---|---|---|---|---|---|---|---|---|---|---|
| | | MAX features | | Etching parameters | | | | | | | Intercalation and delamination | | | | | |
| Category | Acronym | Elemental composition (molar ratio) | Particle size (μm) | Etching route | HF Conc.–Vol. | HCl Conc.–Vol. | LiF Conc.–Vol. | $H_2O$ (ml) | Time (h) | Temp. (°C) | Inter.[a] | Time (h) | Temp. (°C) | Sonication | Shaking | Ref. |
| (Excess Al)[b] | Al-$Ti_3C_2T_x$ | TiC : Ti : Al (2 : 1.25 : 2.2) | 32 | HF + HCl + $H_2O$ | 50 wt%–2 ml | 12 M–12 ml | — | 06 | 24 | 35 | $Li^{+c}$ | 04 | RT | ✗ | ✗ | 55 |
| | | TiC : Ti : Al (2 : 1.25 : 2.2) | < 71 | | 48 wt%–3 ml | 12 M–18 ml | — | 09 | 24 | 35 | $Li^{+c}$ | 01[d] | 65[d] | ✗ | ✓[e] | 56 |
| | | TiC : Ti : Al (2 : 1 : 1; ms) | < 38 | | 50 wt%–2 ml | 12 M–12 ml | — | 06 | 24 | 35 | $Li^{+c}$ | 18 | 35 | ✗ | ✗ | 59 |
| | | TiC : Ti : Al (2 : 1 : 1; ms)[f] | < 38 | | 50 wt%–2 ml | 12 M–12 ml | — | 06 | 24 | 35 | $Li^{+c}$ | 18 | 35 | ✗ | ✗ | 52 |
| MILD | Clay | $Ti_2AlC$ : TiC (1 : 1) | < 38 | HCl + LiF | — | 6 M–30 ml | 5 M–1.98 g | — | 45 | RT | — | — | — | ✓[g] | ✗ | 60 |
| | MILD-1 | $Ti_2AlC$ : TiC (1 : 1) | < 38 | | — | 6 M–20 ml | 7.5 M–1 g | — | 24 | 35 | — | — | — | ✗ | ✓[h] | 61 |
| | MILD-2 | $Ti_2AlC$ : TiC (1 : 1) | ≤ 38 | | — | 9 M–20 ml | 7.5 M–1 g | — | 24 | 35 | — | — | — | ✗ | ✓[i] | 62 and 63 |
| | O-MILD | TiC : Ti : Al (2 : 1 : 1) | < 74 | | — | 9 M–20 ml | 12 M–1.6 g | — | 24 | RT | — | — | — | ✗ | ✗ | 64 |
| HF | HF-MXene | $Ti_2AlC$ : TiC (1 : 1) | < 38 | HF | 50 wt%–1 ml | — | — | — | 02 | RT | — | — | — | — | — | 62 |
| | | TiC : Ti : Al (2 : 1 : 1) | < 74 | | 30 wt%; 10 wt% 5 wt%; 20 ml | — | — | — | 5; 18; 24 | RT | $TMA^+$ | 12 | RT | — | ✓ | 64 |

**Abbreviations:** MILD = minimally intensive delamination, HF = hydrofluoric acid; O-MILD = optimized MILD; M = molar; ms = mass ratio; Conc. = concentration; Vol. = volume; μm = micrometre; ml = milli liters, g = grams; HCl = hydrochloric acid; LiF = lithium fluoride; $TMA^+$ = tetramethyl ammonium hydroxide ions; RT = room temperature; S $cm^{-1}$ = siemens per centimetre.

[a] Intercalating molecule/ion. [b] Prior to etching, HCl washing is reported for such MAX phase to remove intermetallic impurities. MXenes produced from such MAX phase exhibit longer stability (for more than 10 months). [c] For 1 g MAX, 1 g LiCl is dissolved in 50 ml of MilliQ. [d] For 1 h delamination at 65 °C, argon or nitrogen bubbling reported to be necessary. [e] Vortex shaking for 30 minutes in necessary. Otherwise, manual shaking can also be performed. This is because the delamination time is short, and it requires mechanical agitation to produce delaminated flakes. [f] The delamination path employed in the study was termed as soft delamination. [g] To delaminate MXene using this approach, 1 h of sonication is reported and flakes were collected after 1 hour of centrifugation at 3500 rpm. Remember to use an ice bath and Ar bubbling to avoid over heating MXene suspension. [h] Increasing the concentration of LiF facilitate the production of delaminated MXene by manual shaking and avoid the use of intense sonication. But after 3500 rpm/1 h, concentration of MXene suspension was not high. In other others, yield was not higher. [i] As reported, increasing HCl concentration above than 6 M (such as 9 M) delaminate $Ti_3C_2T_x$ MXenes effectively and yield higher concentration of MXene colloidal solution even at manual shaking of < 5 minutes.

**Additional comments**: source of carbon precursor of MAX phase has significant effect the quality of MXene flakes and their aqueous stability.[57] Also, choice of etchant solution effectively determine the surface chemistry of MXenes and properties final application.[58] Before, synthesizing MXene, one should know the requirements and carefully choose the etching routes. (HF + HCl + $H_2O$) + LiCl route offer best delamination with good yield and MXene of good quality. HCl + LiF avoid the direct use of HF, therefore considered greener method but the sonication decreases the sheet size and can induce defects, both leads to reduced stability.

Organic and inorganic molecules, such as $TBA^+$, $TMA^+$, $TPA^+$, *etc.*,[86–90] and univalent metal ions, like $Li^+$, $Na^+$, and $K^+$, and/or multivalent cations, such as $Be^{2+}$, $Ca^{2+}$, $Mg^{2+}$, $Zn^{2+}$, $Mn^{2+}$, $In^{3+}$, $Ho^{3+}$, and $Al^{3+}$, have been extensively used. These cations induce pillaring effects within the flakes and significantly contract or expand the interlayer spacings.[85,91] This cationic exchange also facilitate the mobility of water molecules within the sheets as cations carry water molecules in their hydrated states (Fig. 2a). So, an expanding pressure is provided by such water molecules upon interaction with MXene galleries. Experimentally, this phenomenon is associated with observable swelling, and a clay-like sediment that appears during washing cycles (discussed in phase 4A).[70,85,86] This can be a sign of successful delamination during the experimental synthesis. From a crystallographic viewpoint, this is indicated by the downshifting of the typical 002 peak to lower $2\theta$ values and a corresponding increase in *d*-spacing.

Thermodynamically, this interaction is maintained by the hydration enthalpy of cations and the tendency of the process to reach thermodynamic equilibrium.[84] Whereas the surface termination of MXene influence this thermodynamic equilibrium. Theoretically, the interactions of guest ions must follow certain thermodynamic criteria (*e.g.* Gibbs free energy, $\Delta G$). In particular, cations ($M^{x+}$) behaves differently because of their varying hydration state, thus inducing distinct intercalation effects. For example, a larger *d*-spacing is observed when hydrated metal ions with larger radii intercalate into MXene galleries, resulting in a significant change in the *c*-spacing. Furthermore, the separation between the layers is also expected to change with humidity following the adsorption or desorption of associated water layers.[92,93] Highly charged metal ions (*e.g.* $Fe^{2+}$) tend to form strong ionic or chemical interactions with nearby surface groups, and metal-ion crosslinking induce gelation to form 3D structures.[94] Primarily, the hydration enthalpy or hydration energy $\left(\Delta H^\circ_{\text{hyd.}}\right)$ serve as a critical parameter to relate this interaction between the cation and $H_2O$. $\Delta H^\circ_{\text{hyd.}}$ is directly proportional to $z^2$ (ionic charge) and inversely related to $r$ (ionic radius, Å),[95] which means that cations with a high ionic charge and smaller $r$ have to occupy more water layers and swell MXene significantly.

Ghidiu *et al.* explored the relationship between interlayer expansion and the hydration enthalpy of cations. Cations with a higher charge-to-radius ratio, indicated by a higher absolute value of hydration enthalpy, tend to form $H_2O$ bilayers (two water layers) between flakes.[70] Compared with other cations, $Li^+$ ions ($r = 0.60$ nm; $\Delta H^\circ_{\text{hyd.}} = -520\ \text{kJ mol}^{-1}$) exhibit significant water uptake under higher relative humidity ($R_H$) and wet conditions. Gao *et al.* theoretically predicted that each cation exhibits a distinct affinity for water molecules and MXene surfaces. Noticeably, adsorbed cations electrostatically attract both layers, and the interlayer spacing decreases. Such electrostatic attraction can be high, making it difficult for additional $M^{x+}$ ions to intercalate further because of the narrow galleries. Regardless, an important thing is knowing where the cations go. Previously, it was assumed that they attach to surface terminations. However, this is not always the case. A recent groundbreaking study by Anasori *et al.* demonstrated that cations can fill voids in the defect sites of surface transition metals, thereby increasing stability.[96]

Moreover, Viogt *et al.* reported that anions ($M^{x-}$) can also participate and induce ion exchange, but in a different manner from cations. Notably, anions preferentially reside on the positively charged MXene edges, showing steric effects and preventing the restacking of the MX-flakes (Fig. 2b).[70] The presence of anions on the edges keeps the interlayer spaces open for further water intercalation/de-intercalation. Meanwhile, this can promote the further insertion of $Li^+$ with their full hydration shells upon washing with $Li^+$-containing solutions, leading to significant swelling with more water layers compared to the absence of anions.[70] In conclusion, the etching–intercalation–delamination coordination highlights the interconnected nature of MXene synthesis. This association also offers facile tunability with plenty of space for modification. Yet, this induces complexity and requires some rational approach to first define the synthesis parameters and establish some standards.

### 3.3. Exploring the *in situ* HF methods

Although HF + HCl acid (or pure HF) is established as an outstanding etchant for ''Al'' with the advantage of a higher yield of delaminated MXenes, the direct use of HF poses a safety risk. A safer (and greener) method consists of fluoride salts (LiF, NaF, KF, *etc.*) combined with hydrochloric acid (HCl). In this approach, the interaction of metal fluorides with HCl results in the *in situ* formation of HF. Meanwhile, intercalating ions (*e.g.*, $Li^+$, $Na^+$, and $K^+$) are formed simultaneously to assist delamination. This method yields a clay-like sediment that can be sonicated to obtain highly concentrated aqueous dispersions of delaminated flakes. However, sonication can induce defects, and the size distribution can be significantly different from that of HF or HF + HCl counterparts. Alhabeb *et al.* investigated the effect of etchant concentration on the size, quality, and conductivity of flakes using the LiF + HCl approach.[64] For example, LiF (5 M) + HCl (6 M) causes delamination; however, large flakes were obtained at higher molar ratios of LiF (5–7.5 M) and HCl (6–9 M), respectively. Furthermore, a higher LiF concentration (12 M) was identified as the optimal concentration for better delamination (Table 1). This indicates that a threshold concentration of $Li^+$ ions is required to induce significant swelling for the effective separation of the flakes. This method, referred to as 'minimally intensive layer delamination' (MILD), emphasizes a gentle approach for producing larger single flakes. Typically, MILD methods produce MXene sheets of larger lateral size (in microns), with fewer pinholes/defects compared to pure HF methods, and a higher O-to-F content. *In situ* LiF + HCl has also been reported to leach out non-Al MAX phases, such as $Mo_2Ga_2C$, thus producing $Mo_2CT_x$. However, the scalability of LiF + HCl is limited despite its extensive use. The requirement of sonication and reaction

**MXenes other than $Ti_3C_2T_x$**

The laboratory practices for synthesising MXenes using a wet chemistry route are generally consistent across different MXenes. However, there are specific variations depending on the MXene type. Here are key points to consider: etching conditions such as temperature, etchant concentration, and time change with respect to MXene (Table 2). In addition, the choice of intercalating agent's changes depending on the ml-MXene. So, a ml-MXene may require different intercalants. Moreover, certain laboratory processing conditions, such as washing speed, vary significantly after the intercalation phase† (Scheme 6). Keep in mind, some MXenes require vigorous shaking for delamination. Also, the color of the supernatant‡ can vary during the initial washing cycles after etching. The collection and concentration of the delaminated flakes can be performed by following the phase 4b and 4c, as previously discussed. In addition, Table 2 also summarises the different experimental conditions. Nonetheless, the success of MXene synthesis can be assessed by visual inspections (ESI-I†).

(†) Lighter MXenes (small *n*-values) require stronger force to settle down, and thus require higher rpm and time. (‡) Before centrifugation, the suspension is usually black and after centrifuge, clear supernatant with MXene sedimented at the bottom can be seen. For TMAOH or TBAOH bases, the supernatant from the first cycles is dark and should be discarded. In subsequent cycles, if the supernatant is not transparent, this means that MXene is already delaminated and isolated flakes are mixed with the supernatant. In that case, without removing the supernatant, centrifuge it at 10 000 rpm/10 minutes and discard the supernatant unless it becomes clear. Observe the supernatant at the end of every cycle. If the supernatant is still dark (after 2–3 repetitions), discard it if pH is $>8$, because the base intercalant should not present in the final MXene.

by-products, such as $Li_3AlF_6$ nanoparticles, constrains the purity and stability of MILD-MXenes. Nick *et al.* recently proposed a next-generation MILD method (termed NG-MILD) that involves robust dissolution of $Li_3AlF_6$ in sulfuric acid ($H_2SO_4$), followed by isopropyl alcohol (IPA) washing.[97] Recent reports have also indicated the use of weak acids (*e.g.*, phosphoric acid, $H_3PO_4$).[98] Other fluoride-containing agents such as hydrogen bifluoride ($NH_4HF_2$), NaF, $HBF_4$, and $NaBF_4$ dissolved in HCl also produce *in situ* HF.[99] Note that the experimental practices for etching and subsequent washing are similar to those discussed previously. The downside of the $NH_4HF_2$ involved approach includes a higher content of –F terminations and poorer water dispersion. In addition, the highly corrosive nature of HF (even HF is formed *in situ*) and large amounts of acid waste during washing induce serious safety concerns. To overcome these issues, several other synthesis methods have been developed.

### 3.4. Other synthesis strategies

In recent years, the synthesis of MXenes has extended beyond the traditional aqueous fluoride-containing methods, leading to the exploration of various alternative techniques. These approaches overcome certain limitations of conventional methods, such as the use of aggressive acids and provide a facile control over tailoring the MXene surface environment. Herein, we provide a brief overview of these methods.

**Molten salt-assisted and halogen etching:** Compared to the previously discussed etching routes, molten salt-assisted and

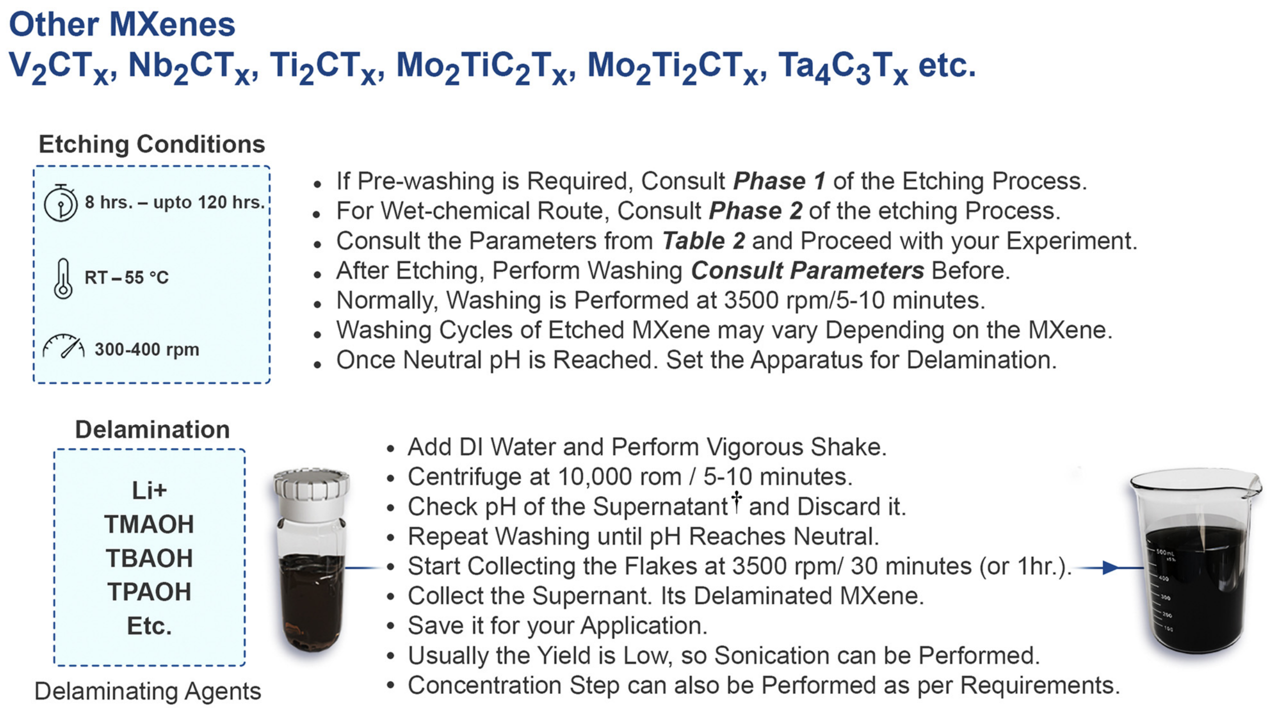

- If Pre-washing is Required, Consult ***Phase 1*** of the Etching Process.
- For Wet-chemical Route, Consult ***Phase 2*** of the etching Process.
- Consult the Parameters from ***Table 2*** and Proceed with your Experiment.
- After Etching, Perform Washing ***Consult Parameters*** Before.
- Normally, Washing is Performed at 3500 rpm/5-10 minutes.
- Washing Cycles of Etched MXene may vary Depending on the MXene.
- Once Neutral pH is Reached. Set the Apparatus for Delamination.

- Add DI Water and Perform Vigorous Shake.
- Centrifuge at 10,000 rom / 5-10 minutes.
- Check pH of the Supernatant† and Discard it.
- Repeat Washing until pH Reaches Neutral.
- Start Collecting the Flakes at 3500 rpm/ 30 minutes (or 1hr.).
- Collect the Supernant. Its Delaminated MXene.
- Save it for your Application.
- Usually the Yield is Low, so Sonication can be Performed.
- Concentration Step can also be Performed as per Requirements.

Scheme 6 Generalised scheme to synthesise MXenes other than $Ti_3C_2T_x$. Most MXenes (other than Ti-based systems) require an organic basis for delamination and must be carefully washed away.

Table 2 For MXenes other than $Ti_3C_2T_x$: a catalogue on synthesis parameters (per gram) of well-known etching methods

| Different MAX phases and MXene structures | | | | Wet chemical etching routes and experimental parameters | | | | | | Production of isolated flakes | | | | | | |
|---|---|---|---|---|---|---|---|---|---|---|---|---|---|---|---|---|
| | | MAX features | | Etching parameters | | | | | | Intercalation and delamination | | | | | | |
| | | | | | | | | | | Intercalants | | | | | | |
| | MXene | Elemental composition (molar ratio) | Particle size (μm) | Etching route | HF Conc.–Vol. | HCl Conc.–Vol. | LiF (g) | Time (h) | Temp. (°C) | Type | Conc.–Vol. | Time (h) | Temp. (°C) | Sonication | Shaking | Ref. |
| **$M_2CT_x$** | $V_2CT_x$[a] | V : Al : C (2 : 1.1 : 0.9) | < 38 | HF + HCl + $H_2O$ | 48–50%–12 ml | 12 M–8 ml | — | 72 | 50 | $TBA^+$ | 5 wt%–20 ml | 6 | 50 | ✗ | ✓[b] | 72 |
| | | V : Al : C (2 : 1.2 : 1) | < 38 | HCl + LiF | — | 12 M–12 ml | 1 | 120 | 90 | — | — | — | — | ✓[c] | ✓[c] | 73 |
| | | V : Al : C (2 : 1.1 : 0.9) | < 38 | HF | 48–50%–20 ml | — | — | 96 | RT | $TMA^+$ | 5 wt%–20 ml | 6 | RT | ✗ | ✓[b] | 72 |
| | | | < 38 | HF | 48–50%–20 ml[d] | — | — | 45 | RT | $TMA^+$ | 25 wt%–3 ml | 12[e] | RT | ✗ | — | 74 |
| | | V : Al : C (2 : 1.3 : 1) | < 38 | HF | 30% | — | — | 92 | RT | $TBA^+$ | 54–56%–10 ml | ∼4 | RT | ✗ | ✓[f] | 75 |
| | $Ti_2CT_x$ | Ti : Al : C (2 : 1.1 : 0.9) | < 75 | HF + HCl + $H_2O$ | 48–50%–2 ml | 12 M–12 ml[g] | — | 24 | RT | $Li^+$ | 50 ml | 4 | RT | ✗ | ✗ | 76 |
| | | Ti : Al : C (2 : 1.1 : 1) | ∼90 | HCl + LiF | — | 11.7 M–40 ml | 4 | 35 | 24 | — | — | — | — | ✓[h] | ✗ | 77 |
| | | | — | HF | 10 wt%–10 ml | — | — | 8 | RT | $TMA^+$ | 25 wt%–1 ml | 2 | RT | ✓[i] | ✗ | 43 |
| | $Nb_2CT_x$ | Nb : Al : C (2 : 1.1 : 1) | < 74 | HF + HCl + $H_2O$ | 48%–12 ml | 12 M–8 ml | — | 48 | 50 | $TMA^+$ | 5 wt%–20 ml | 6 | 35 | ✓ | ✗ | 78 |
| | | | < 74 | HCl + LiF | — | 12 M–20 ml | 2 | 84 | 100–115 | — | — | — | — | ✓ | ✗ | 79 |
| | | | < 74 | HF | 50 wt%–20 ml | — | — | 48 | 50 | $TMA^+$ | 4 ml | 18 h | RT | ✓ | ✗ | 80 |
| | | | — | HF | 48–50 wt%–10 ml | — | — | 96 | RT | $TMA^+$ | 25 wt%–1 ml | 12 | RT | ✓[i] | ✗ | 43 |
| | | Nb : Al : C (4 : 1.1 : 2.7) | < 75 | HF | 48–50 wt%–20 ml | — | — | 168 | RT | $TMA^+$ | 0.5 g–25 wt% | 12 | RT | ✗ | ✗ | 76 |
| | | | — | HF | 48–50 wt%–10 ml | — | — | 90 | RT | $TMA^+$ | 25 wt%–1 ml | 12 | RT | ✓[i] | ✗ | 43 |
| **$M_3C_2T_x$** | $Mo_2TiC_2T_x$ | Mo : Ti : Al: C (2 : 1 : 1.1 : 2) | — | HF + HCl + $H_2O$ | 10 wt% –10 ml | 10 wt%–10 ml | — | 40 | 40 | $TBA^+$ | 0.8 wt% | 2 | RT | — | ✗ | 62 |
| | | | < 38 | HF | 48–50 wt%–20 ml | — | — | 48 | 55 | DMSO | 10 ml | 24 | RT | ✓ | ✗ | 81 |
| | | | — | HF | 48–50 wt%–10 ml | — | — | 100 | 55 | $TMA^+$ | 25 wt%–1 ml | 12 | RT | ✓[i] | ✗ | 43 |
| | | | < 75 | HF | 48–50 wt%–20 ml | — | — | 96 | 50 | $TMA^+$ | — | 12 | RT | ✗ | ✗ | 76 |
| **$M_4C_3T_x$** | $Mo_2Ti_2C_3T_x$ | Mo : Ti : Al : C (2 : 2 : 1.3 : 2.7) | — | HF + HCl + $H_2O$ | 10 wt%–10 ml | 10 wt%–10 ml | — | 40 | 40 | $TBA^+$ | 0.8 wt% | 2 | RT | ✗ | ✗ | 62 |
| | | | < 38 | HF | 48–50 wt%–20 ml | — | — | 90 | RT | — | — | — | — | ✗ | ✗ | 81 |
| | | | < 75 | HF | 48–50 wt%–20 ml | — | — | 96 | 50 | $TMA^+$ | — | 12 | RT | ✗ | ✗ | 76 |
| | | | — | HF | 48–50 wt%–10 ml | — | — | 96 | 55 | $TMA^+$ | 25 wt% | 12 | RT | ✓[i] | ✗ | 43 |
| | $Ta_4C_3T_x$ | | — | HF | 48–50 wt%–10 ml | — | — | 72 | RT | $TMA^+$ | 25 wt% | 12 | RT | ✓[i] | ✗ | 43 |

**Abbreviations**: M = molar; Conc. = concentration; Vol. = volume; μm = micrometre; ml = milli liters, g = grams; RT = room temperature; S $cm^{-1}$ = siemens per centimetre; HCl = hydrochloric acid; HF = hydrofluoric acid; LiF = lithium fluoride; $TMA^+$ = tetramethyl ammonium hydroxide ions; $TBA^+$ = tetrabutyl ammonium hydroxide ions; DMSO = dimethyl sulfoxide; $Li^+$ = lithium ions. [a] $V_2AlC$ particles usually contain unreacted elemental powders or intermetallic impurities. MAX powder is reported to washed by soaking in 9 M HCl for 12 h. [b] It is crucial that the shaking process should be performed for at least 2 min to ensure that the sediment is uniformly redispersed in fresh DI water and flakes were collected at 2000 rpm/30 minutes centrifuge and collecting the dark supernatant. [c] Ultra-sonication of 15 minutes is reported followed by manual shaking and centrifuge (4500 rpm/20 min) for delaminated flakes collection. [d] In this study, prior to etching, the resulting powder was treated in 100 mL of a 10 M $H_3PO_4$ solution at 80 °C for 15 h to dissolve and remove impurities from $V_2AlC$, such as $Al_8V_5$ and $V_2C$. [e] The resulting etched $V_2C$ powder was dried at 60 °C in a vacuum oven overnight and increase in delamination time can be associated to this. [f] Shaking for 2 minutes was performed to mix the thick settled powder and further centrifuged at 2000 rpm/30 minutes to collected delaminated flakes. [g] In this study, mixed acid route was followed, and 6 ml was also added alongwith HF and HCl. [h] MXene sediment was mixed in 20 ml of DI water and sonicated for 1 h at RT under Ar bubbling and flakes were collected after 1 hour of centrifuge at 3500 rpm. [i] To delaminate MXene using this approach, 1 h of sonication is reported and flakes were collected after 1 hour of centrifuge at 3500 rpm. Remember to use ice bath and Ar bubbling to avoid over heating MXene suspension.

halogen-based etching routes are safe, fluorine-free, and provide MXenes with the feasibility of adding an array of other functional groups beyond those produced *via* conventional HF-based etching (═O, –H, –F, –Cl, *etc.*).[100] The Lewis acid molten salts route (*e.g.*, $CuCl_2$, $CdCl_2$, $CdBr_2$, $ZnCl_2$/NaCl/KCl system, $FeCl_2$ *etc.*) is effective in removing A-layers, extending beyond the typical Al such as Zn, Si, and Ga.[101–103] In this method, oxidizing agent-stabilizing ligand pairs also exist, similar to fluoride-based routes ($H^+$–$F^-$), such as $Cu^{2+}$ (oxidizing agent) and $Cl^-$ (oxidizing ligand) in $CuCl_2$, leading to volatile byproducts that are then evaporated, producing $Cl^-$ or $Br^-$ terminated MXene.[33,49] Due to their weak bonding with transition "M" atoms, these terminal groups (–Cl and –Br) act as a template and are covalently substituted with other groups *e.g.* ═O, –NH, –S, –Se, and –Te through specific postprocessing procedures (detailed in ESI-I†). This is perhaps the most attractive feature of this strategy as it provides an easier route towards surface-customized MXenes. This approach is also an environment-friendly alternative as one-pot synthesis method for MXenes; however, it requires high temperatures, which leads to increased energy consumption. In addition, it is challenging to delaminate the resulting MXenes into single-layer flakes, and the yield is limited too.[104] Halogen-based etching offers a safer, milder, and more versatile alternative, enabling the modification of surface terminations with assemblies similar to those in molten-salt processes.[103] Examples of this approach include the use of $I_2$ in acetonitrile $CH_3CN$ with HCl washing, leading to $Ti_3C_2I_x$, and elemental halogens with interhalogen compounds to produce $Ti_3C_2Br_x$.[105,106] These approaches show promise for producing MXenes beyond $Ti_3C_2T_x$, particularly nitride MXenes, which are difficult to prepare *via* HF etching.

**Water-free etching:** Water serves as the primary solvent in the acid etching process, affecting MXene storage and limiting its use in water-sensitive applications. However, MXenes can be synthesized by immersing the MAX phase in a polar organic solvent, such as propylene carbonate (instead of water) and ammonium dihydrogen fluoride ($NH_4HF_2$), which removes the A layer and allow $NH^{4+}$ cointercalation.[107] The synthesized MXenes predominantly contain excessive –F terminal groups (70%), with the remaining 30% comprising ═O/–OH groups. Water-free etchants improve the chemical stability of MXenes and reduce the oxidation. Also eliminating fluorine groups is estimated to significantly decrease the defects in MXenes and provide the ability to tailor their surface terminations.[105,106,108] However, the synthesis process requires an argon-filled glovebox to maintain purity and is relatively slow, taking approximately 196 h, making it time consuming and complex. Further research is necessary to optimize the process, reduce the synthesis time, and evaluate its effectiveness for various applications.

**Electrochemical etching:** Another promising approach to obtain fluorine-free MXenes is electrochemical etching. In this process, the MAX phase electrode is subjected to a certain potential in the presence of low-concentration HCl as an electrolyte, which leads to the removal of the A layers.[109] The resulting MXene lacked the –F terminations. However, unreacted MAX phases lead to unwanted carbide-derived carbon (CDC) layers during the corrosion process. The insertion of intercalants has solved this problem, as intercalant opens the layers that facilitated further etching deeper into the internal $Ti_3AlC_2$ layers. Furthermore, molten salt-assisted electrochemical etching enabled the *in situ* formation of –Cl-terminated fluorine-free $Ti_3C_2Cl_2$.[110] The surface terminations can be further tuned to ═O and/or –S, thus contributing to the structural diversity. Molten salt-assisted electrochemical etching has been used to directly produce $Ti_2C$ MXene using elemental components (Ti, Al, and C), resulting in a one-pot synthesis of –F-free MXenes.[111] In addition to Ti–MXenes, the electrochemical etching of $Nb_2C$ MXenes has also been reported for enzymatic electrochemical sensors.[112] While electrochemical etching has proven effective for producing fluorine-free MXenes, several key factors such as electrolyte composition, selection of etching voltage, precise control over etching time, influence on the synthesis process and relatively low yield (40%) pose challenges for widespread use.

**Acoustic synthesis:** One of the most innovative and distinct approaches for MXene synthesis is acoustically driven fabrication, which offers a novel perspective compared with traditional methods.[113] This approach enables the rapid (millisecond) synthesis of $Ti_3C_2T_x$ by applying megahertz-frequency acoustic excitation to the $Ti_3AlC_2$ MAX phase in a LiF solution, presenting a cost-effective solution for MXene production.[114] High-frequency acoustic waves have also been used to delaminate multilayer MXenes into MXene quantum dots, highlighting the chemical-free production of zero-dimensional structures.[115]

Various other synthesis methods have been explored, including alkali-assisted hydrothermal etching, hydrochloric acid-assisted hydrothermal etching, dry solvent extraction, and thermal reduction, as detailed in recent reviews.[103,116–118] Bottom–up approaches, such as chemical vapor deposition-assisted template growth[119] and plasma-liquid synthesis[120] have also been investigated.

In short, alternative methods demonstrate significant versatility in tailoring MXene properties, such as introducing diverse surface terminations (*e.g.*, –Cl and –Br *via* molten salts) and enabling fluorine-free synthesis. Challenges such as energy consumption, synthesis complexity, and low yields limit their scalability. Methods such as molten salt etching, water-free etching, and electrochemical approaches provide valuable platforms for niche applications and customized MXenes, particularly where environmental concerns or specific termination chemistries are critical. However, wet chemical etching using fluorine-containing solutions remains the most efficient and scalable method for large-scale production, offering higher yields and simple processing. So, HF-based wet etching continues to dominate practical and industrial applications owing to its reliability and cost-effectiveness.

### 3.5. Strategies for nanocomposite and hybrid synthesis

To expand the use of MXenes and address inherent limitations, it requires controlled surface modification with various organic/inorganic species and nanomaterials (such 0D, 1D, and 2D systems). The purpose is to enhance their colloidal stability in a biological media, providing a suitable interface for sensing, profuse drug loading and elevated photothermal conversion efficiency.

Although the literature often discusses MXene composites for biomedical and biosensing applications,[17,121] we focus on tutorial aspects presenting a mechanistic view for academic insights. Unlike other 2D materials, MXene's transition metals can donate electrons because of their lower oxidation states (acts like reducing agents), thereby acting as an innovative platform to anchor noble metal nanoparticles. So, the wet chemical reduction of metal salts precursors is the most efficient method to decorate the MXene surface with nanoparticles. Such an approach is more suitable than physical methods as it allows control over nanoparticle size and shape through external factors like pH, temperature, and reaction duration. Despite these advantages, residual reducing agents or surfactants (if used any) can interfere with analyte adsorption.

**3.5.1. Self-reduction.** MXenes can directly reduce noble metal cations into metallic nanoparticles (NPs) *via in situ* redox reaction without using external reducing agents. These metallic nanostructures firmly adhere to the MXene surface and provide a simple method to create nanostructured substrates. According to Cheng *et al.*, the surface electrons strongly determine the electronic structure of MXene, thus playing a crucial role in the self-reduction process.[122] Functional groups on MXene surface have a strong impact on its electronic structure, with the electronic work function ($W$) varying in the following order: $W_{OH} < W_F < W_O$. Also, the position of the Fermi level ($E_F$) varies with terminations (Fig. 3a) and changes the band gap values. Similarly, the valence electrons near $E_F$ respond differently and typically participate in oxidation–reduction reactions. As evident from the electronic configuration (Fig. 3a), $E_F$ is significantly higher than the $H^+/H_2$ redox energy of –OH terminated MXenes. Consequently, when $Ti_3C_2(OH)_2$/(–OH) interacts with an acidic solution containing metal salt precursors, electron transfer occurs from MXene to the $H^+$ ions in the solution, releasing $H_2$ molecules. Conversely, $Ti_3C_2F_2/O_2$ does

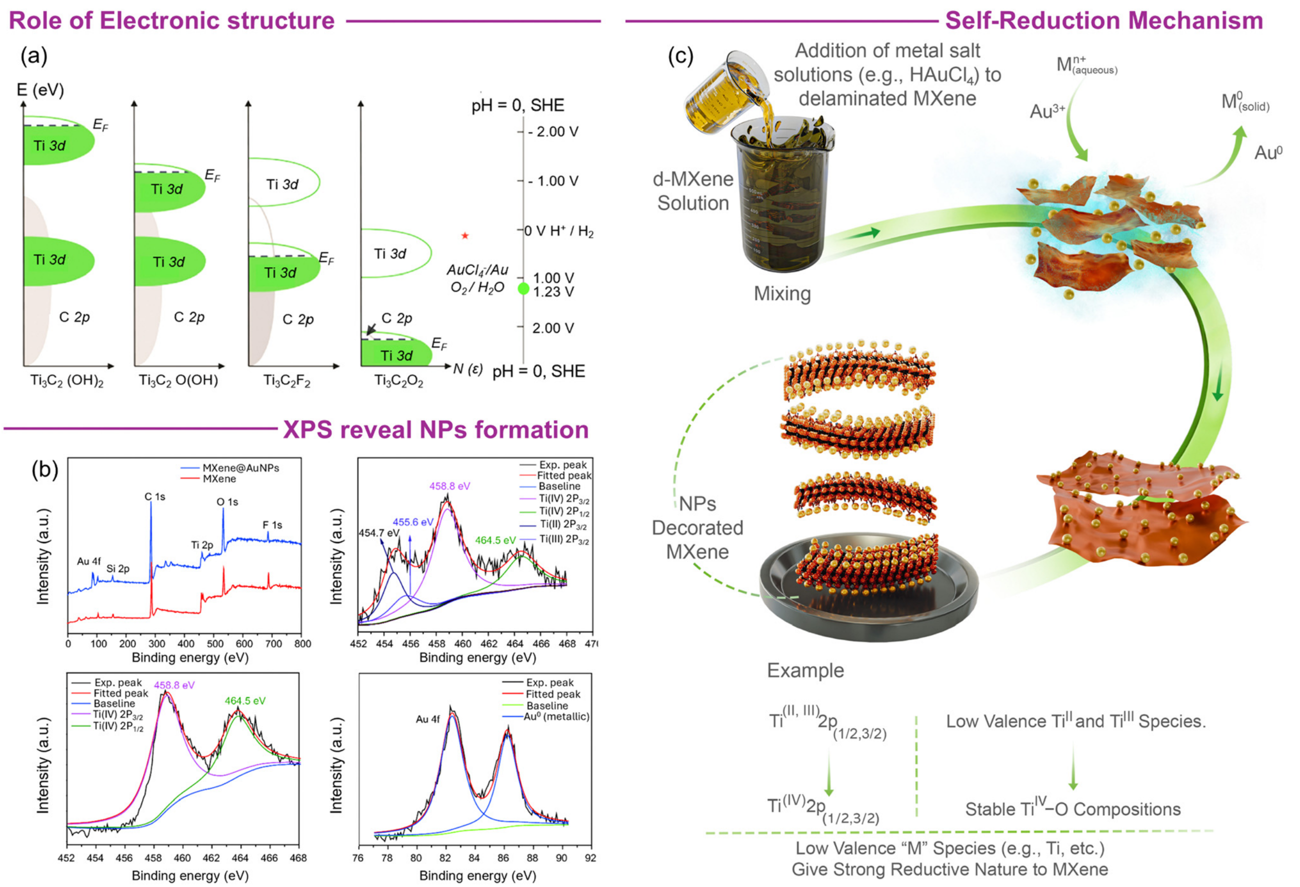

Fig. 3 (a) The density of states (DOS) in terminated MXenes, analysed using density functional theory (DFT), reveals a shift in the Fermi level with respect to the terminal groups. The difference in energy levels facilitate charge transfer and the spontaneous reduction of the salt solution. Reproduced with Permission from ref. 122 Copyright © 2020, Elsevier. (b) XPS indicates the presence of lower valence titanium species Ti(II) $2p_{1/2}$ and Ti(III) $2p_{3/2}$ that enable self-reduction processes and change to stable Ti(IV) species and $Au^0$ NPs formation. Reproduced with Permission from ref. 127 Copyright © 2018, Science China Press and Springer-Verlag GmbH Germany, part of Springer Nature. (c) Schematic illustration of the self-reduction of salt solution to the corresponding nanoparticles on MXene flakes.

not facilitate electron transfer because its $E_F$ is lower than the redox potential of the $H^+/H_2$ couple and lacks non-binding Ti sites. Hence, $Ti_3C_2(OH)_2$/(–OH) donates electrons to noble metal cations such as $Au^{3+}$ without affecting the structural stability or requiring an external reducing agent. Such interactions are effective even at low concentrations of metal salt solutions ($1.0 \times 10^{-4}$ mol $L^{-1}$) and yield a uniform distribution of NPs on the MXene surface.[122] Typically, the hydroxyl groups (–OH) in common reducing agents facilitate the conversion of metal salts to cations and then to nanoparticles.[123] So, the surface functional groups not only promote ion exchange, but the intrinsic –OH also acts as an effective reducing agent. Now, one may correlate this effect of the –OH groups with the electron donation aspects previously discussed with the DOS interpretation. X-Ray photoelectron spectroscopy (XPS) further elucidated the self-reduction mechanism (Fig. 3b). In $Ti_3C_2T_x$, a distinct peak around 458.8 eV in the samples is attributed to $Ti^{(IV)}$ $2p_{3/2}$, indicating stabilised $Ti^{(IV)}$–O compounds. Whereas a broad peak at approximately 454.7 eV for $Ti^{(II)}$ $2p_{1/2}$ and 455.6 eV for $Ti^{(III)}$ $2p_{3/2}$ suggests the presence of lower valence titanium species. These low-valence Ti species facilitate the formation of metallic nanoparticles and enabled self-reduction processes, principally leading to the conversion of $Ti^{(II)}$ $2p_{1/2}$ and $Ti^{(III)}$ $2p_{3/2}$ to stable $Ti^{(IV)}$ species (Fig. 3b and c).[124] A similar mechanism can be associated with other nanoparticle salts or bimetallic systems; however, their growth and morphology may be different.[124–126] Sonication during the self-reduction process can significantly impact growth and lead to a more uniform distribution or monodispersed MXene solution.[126] Nonetheless, self-reduction is most favourable for metallic nanoparticles and provides facile control over the size, shape, and concentration of NPs on the MXene surface.

**3.5.2. Electrostatic self-assembly.** Another method to prepare MXene composites or hybrids is the electrostatic self-assembly approach that can also be generalised to other nanomaterials. MXene flakes typically have a negative charge as confirmed by their zeta potential (usually below −30 mV). This property allows MXenes to hold positive guest species electrostatically. Usually, the noble metal NPs have a negative charge and cannot interact effectively with MXene surfaces. To enable electrostatic self-assembly, cationic surfactants such as cetyltrimethylammonium bromide (CTAB) have been used (Fig. 4a). CTAB reverses the polarity of the guest species to a positive charge that promotes their deposition on the negatively charged MXene sheets. The change in zeta potential of the MXenes and guest species (before and after CTAB treatment) can be used to verify the charge inversion and formation of self-assembly. Also, an immediate agglomeration can be observed,

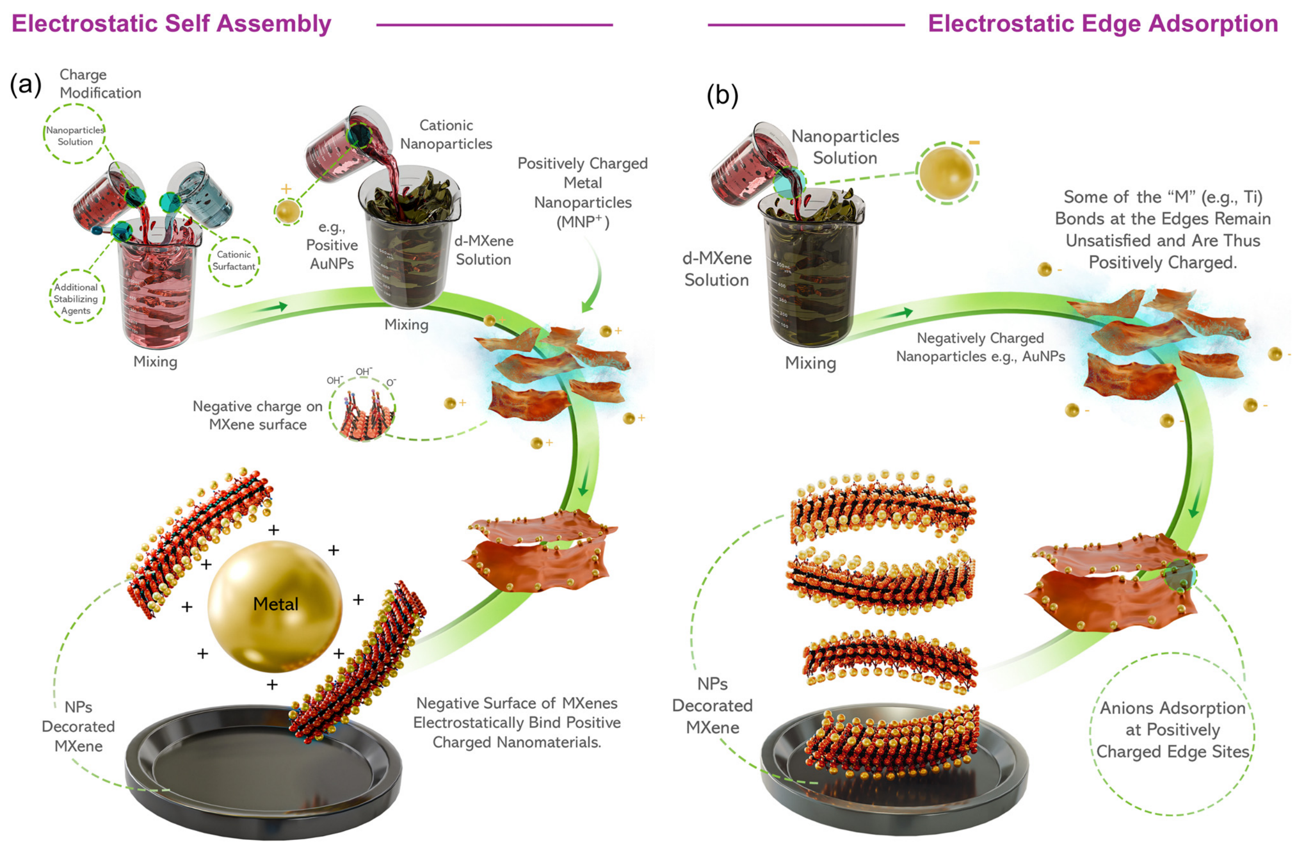

Fig. 4 Schematic demonstration of the (a) possible pathway for charge inversion and electrostatic self-assembly with negatively charged MXene. (b) Electrostatic adsorption of negatively charged nanoparticles with positive edges of MXene flakes.

indicating successful electrostatic assembly. For simplicity, we use the acronym ‘‘guest species’’, which can be generalized to other nanomaterials reported in the literature.[128,129] Apart from this, certain 2D materials such as layered double hydroxides (LDH) have an intrinsically positive surface and offer facile synergistic integration with MXene flakes for benefits such as enhanced specific capacity.[130]

**3.5.3. Electrostatic edge adsorption.** Interestingly, MXenes exhibit a peculiar charge distribution across the flake dimensions. Natu *et al.* revealed that the edges of $Ti_3C_2T_x$ are positive compared to the surface.[48] Upon adding gold NP solution to MXene suspension, negatively charged AuNPs preferably reside at the edges (Fig. 4b). This difference in polarity between the surface and edges enables new features *e.g.*, distinct functionalizations as observed in other 2D materials, and shows potential for sensing applications.[131]

**3.5.4. Doping.** Introducing foreign elements into two-dimensional materials, known as ‘‘doping’’, significantly alters their chemical and physical properties. It has been demonstrated that MXenes can be incorporated with non-metals, transition metals, and single-atom systems, which in turn effectively enhances their physical, chemical and electrical properties. Doping typically involves the addition of heteroatoms over/within the MXene lattice and can be performed before and/or after etching (Fig. 5). According to the literature,[26,28] the M, X, or T components of MXenes can be doped and categorised as (a) M-doped-, (b) X-doped, or (c) T-substituted MXenes. Transition metals such as Mo, Cr, and Ru can replace the M and X positions in doped MXenes, whereas heteroatoms such as N, P, S, or O can be inserted in all three positions (M, X, and T). Halides can also replace the T elements. Doping modifies the interlayer structure and surface area, thus enhancing electrode conductivity and imparting new redox capabilities which lower the electrode/electrolyte interfacial impedance. Although the literature suggests that dopant atoms serve as the active sites, the complex surface chemistry of MXenes provides a variety of adsorption and reaction pathways. This implies that each component of the doped MXenes work synergistically to drive cascade reactions.

**Supplementary information I (ESI†)**

- Quick check to access MXene synthesis in a lab
- Flake size distribution and influencing factors
- MXene films and drying conditions
- Oxidation and restoring oxidized MXene
- Surface chemistry of MXenes
- Solution processing and printing

As stated above, the synthesis of MXenes can be evaluated in the laboratory through visual assessment. This section outlines the methods used for quick onsite analysis. Additionally, various factors, such as the MAX phase particle size, etchant concentration, delamination method, and centrifugation, can affect the MXene size distribution. Strategies to address MXene oxidation, methods to mitigate it, and techniques for restoring oxidized MXenes are also discussed. Furthermore, the vacuum filtration of MXene dispersions, a commonly used technique for fabricating MXene films for various applications, is briefly reviewed. In addition, the surface chemistry of MXenes is described. Functional inks and controllable modifications of MXenes allow their use in 3D printing, inkjet printing, and other printing techniques to fabricate sensing devices and biomedical prototypes. Herein, we discuss the printing process of nanofunctional inks and the processing of MXenes to obtain functional inks for printing.

# 4. Healthcare applications of MXenes

This section discusses the applications of MXenes in various healthcare domains, such as sensing, biomedical imaging, synergistic therapies, regenerative medicine, wearable devices. For a more detailed understanding of the subject, a discussion on the biocompatibility, antimicrobial features and ecological impact of MXenes is provided in ESI-II.†

## 4.1. Customization of MXenes for healthcare applications

Considering that the following section discusses the use and ongoing trends of MXenes for sensing and various biomedical applications, understanding their customization is paramount for effective biological utility. MXenes exhibit a robust structure–property relationship driven by their versatile compositions (varied M and X elements), layer number, synthesis methods, surface terminations, flake size, and geometry. These factors critically influence their electrical, optoelectronic, and mechanical properties as well as their stability in physiological media, biocompatibility, and biodegradability. Therefore, a thorough understanding and precise control of the

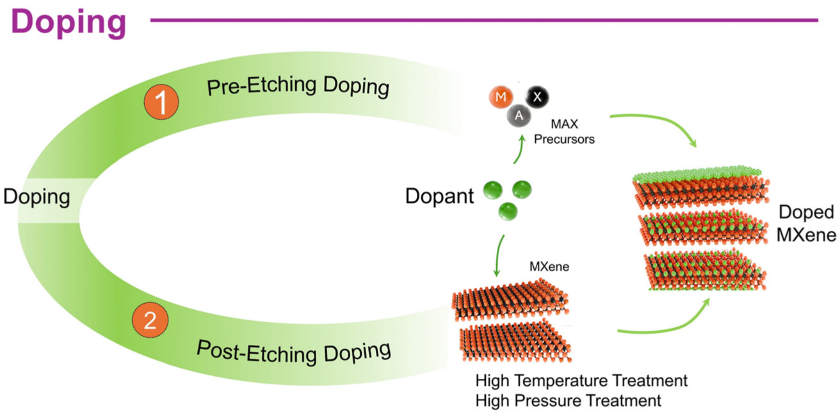

Fig. 5 Possible approaches of doping MXenes.

aforementioned parameters is essential to ensure the safe and effective application of MXenes in biomedical settings.

The intrinsic surface terminations of MXenes uniquely enable precise tuning of their properties. Also, their tendency to aggregate in physiological environments necessitates modification to ensure colloidal stability. For this purpose, the introduction of hydrophilic groups such as –OH, –COOH, polyethylene glycol (PEG), polyvinylpyrrolidone (PVP), soy phospholipid (SP), polyvinyl alcohol (PVA), and bovine serum albumin (BSA) significantly enhances stability in physiological environments.[39,132] This, in turn, enhances their interaction with living cells, improves cellular uptake, biodistribution, and loading capacity, while also facilitating *in vivo* degradation.[133] External modifications also enhance the photothermal conversion efficiency (PTCE) in NIR-I/NIR-II biowindows, enabling photothermal hyperthermia to effectively eradicate the tumor.[132] Similarly, surface modifications are crucial for integrating bio-recognition elements for biosensing applications. For instance, APTES (3-aminopropyl triethoxysilane) grafting is commonly used because of its strong covalent affinity for the –OH groups. At the same time, amine groups ($-NH_2$) of APTES provide a stable interface for biofunctionalization.[134] Introducing noble metal nanoparticles or other nanomaterials onto the MXene flakes mitigate their self-restacking, thereby improving colloidal stability and biocompatibility.[135] The nanoparticles also promote the immobilization of DNA or antibodies for (bio)sensing applications. The development of more robust MXene structures, such as 0D/2D (*e.g.*, Au, Ag, Pt, and Pd nanoparticles, and bimetallic systems), 1D/2D (*e.g.*, carbon nanotubes), 2D/2D (*e.g.*, TMDCs, graphene derivatives, and other 2D materials),[136] and hydrogels[137] has broadened their use in sensing applications. This also provides control over the thermal conductivity of MXenes, which is critical for heat-sensitive applications, such as photothermal therapy.[138]

The physical dimensions of the MXene flakes play a crucial role in determining their biomedical functionality. Such variations can arise from several factors, as detailed in ESI-I.† Briefly, MXenes with larger lateral sizes exhibit improved interflake contact and better alignment, resulting in higher conductivity.[139] Flake dimensions are also important for the rheological behavior of MXenes (*e.g.*, for printing) and their mechanical properties.[34] From a biological perspective, MXene sheets exhibit size- and morphology-dependent antimicrobial properties (ESI-II†). Conventional top–down synthesis methods often produce micron-sized sheets, raising concerns about biosafety. For intravenous or intratumoral administration, smaller MXene flakes facilitate smooth intracellular transport, enhance cell penetration, and reduce the accumulation risk. Reducing the flake size also enhances the photocatalytic activity, particularly for reactive oxygen species (ROS) generation during wound healing.[140] MXene quantum dots (QDs) can easily diffuse into biological tissues owing to their ultrasmall size, thus enabling detailed fluorescence imaging at the cellular level. These properties make them ideal for monitoring cellular processes, tumor visualization, and assessing therapeutic delivery in real-time.

Another strategy to regulate MXene properties is by modifying the interlayer gaps (interlayer tunability), which affects the electrical, optoelectronic, and mechanical characteristics. The sub-nanometer interlayer spacing facilitates rapid ion uptake and can be modulated through post-etching procedures by introducing suitable molecules (*e.g.*, polyaniline ''PANI'', polypyrrole ''PPy'')[141] or spacers (*e.g.*, CNT, *etc.*).[142] This can provide a stable interface for biological applications, enhance electrochemical performance, and control mechanical properties (*e.g.*, stiffness and flexibility), thus optimizing the performance of MXenes in wearable devices or implants.[27] On the other hand, oxidized MXenes have shown potential for gas sensing, inducing antimicrobial features to MXenes, and facilitating sonodynamic therapy.

In summary, a careful selection and implementation of these strategies can optimize their performance. However, ***it is crucial to determine the extent to which these parameters affect the utility of MXenes in biomedical applications***. In brief, (i) the surface engineering effectively controls the properties.[143,144] Various engineered MXenes, such as SP@$Ti_3C_2T_x$,[145] SP@$Ti_3C_2T_x/MnO_x$,[146] SP@$Ti_3C_2T_x$/PLGA,[147] SP@$Ta_4C_3T_x/MnO_x$,[148] SP@$Ta_4C_3T_x$/IONPs[149] CTAC@$Nb_2CT_x$,[150] $Nb_2CT_x$/PVP,[151] $Mo_2CT_x$/PVA,[152] PEGylated-MXenes,[132] *etc.* have shown an improved biomedical profile compared to their pristine counterparts.[140] (ii) Delaminated MXenes with small flake sizes (typically sub-nanometer) are preferable for effective biomedical functionalities;[153–155] however, they often exhibit reduced oxidative stability. Surface engineering also mitigates this problem by functionalizing the materials with stabilizing agents. (iii) Higher concentrations or dosages of MXenes can induce aggregation, exceed the capacity of cellular systems, and increase toxicity, as detailed in ESI-II.†[156] Therefore, a well-functionalized MXene with an appropriately small flake size and concentration is the optimal choice for biomedical applications. Nevertheless, larger flakes of MXene offer high conductivity and mechanical strength, which are particularly beneficial for electrochemical sensing and wearable devices. These factors collectively position MXenes as highly versatile materials with significant potential for use in various biomedical technologies.

### 4.2. Sensing

MXenes have become interesting materials for sensing applications due to their electrical conductivity, and adjustable surface chemistry. Here we review the use of MXenes in electrochemical and optical sensors.

**Electrochemical signal transducers:** For electrochemical biosensing, the earliest investigations reported haemoglobin immobilized ml-$Ti_3C_2T_x$ for $H_2O_2$ detection with an LOD of 20 nM (linear range of 0.1–260 μM).[157] ml-MXenes offered a protective microenvironment for the immobilized enzymes whereas $H_2O_2$ effectively oxidised the terminal groups, thereby enhancing the oxygen density and improving the charge transfer process. In contrast, sl-MXenes demonstrated a superior heterogeneous electron transfer rate (HET), thus performing comparatively better than ml-MXenes counterparts. As HET depends on the difference between cathodic and anodic peak

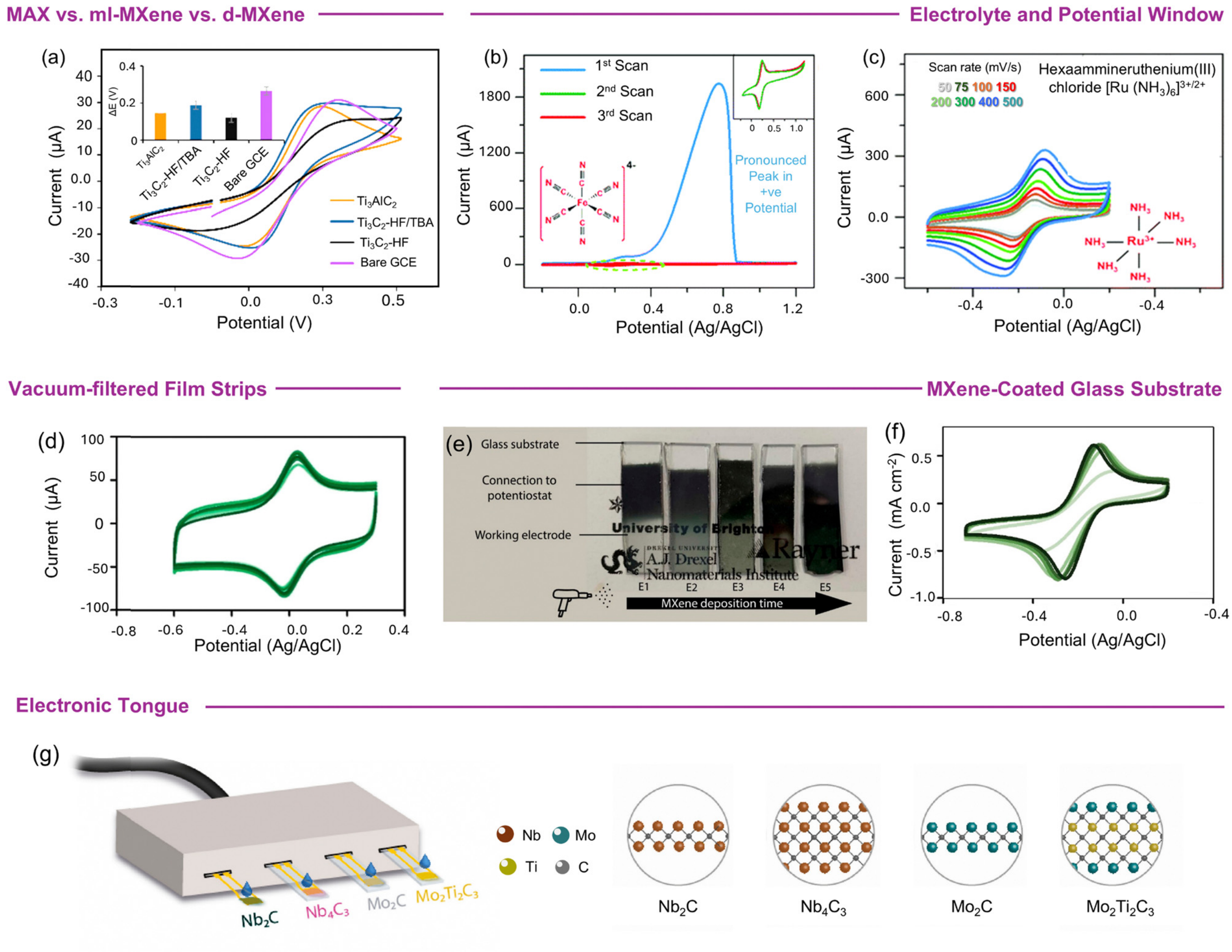

Fig. 6 (a) CV behaviour of $Ti_3AlC_2$ MAX and different configurations of $Ti_3C_2T_x$ MXenes; the inset shows the corresponding $\Delta E_p$ values. Reproduced with Permission from ref. 158 Copyright © 2020, American Chemical Society. CV trends of delaminated $Ti_3C_2T_x$ (b) in the $[Fe(CN)_6]^{4-/3-}$ redox probe (in 0.1 M KCl) in the anodic potential window showing an evident oxidation peak of $Ti_3C_2T_x$ itself and an irreversible nature in subsequent scans (c) in the $[Ru(NH_3)_6]^{3+/2+}$ redox probe (in 0.1 M KCl) showing no oxidation peak. Reproduced with permission from ref. 160 and the Royal Society of Chemistry. (d) CV behavior of MXenes films strips with prominent capacitive contribution. (e) Digital image of spray-coated MXenes on Glass substrate. (f) Corresponding CV curves with prominent faradaic contributions. Reproduced with Permission from ref. 162 Copyright © 202, American Chemical Society. (g) Schematic illustration of gold-interdigitated electrodes modified with four different MXenes acting as e-tongue. Reproduced with Permission from ref. 165 Copyright © 2024 The Authors. Published by Elsevier B.V.

potentials ($\Delta E_p$), narrower $\Delta E_p$ corresponds to remarkable catalytic activity of sl-$Ti_3C_2T_x$ in the $Fe^{2+}/Fe^{3+}$ redox couple (in 0.1 M KCl) (Fig. 6a).[158] This can be attributed to the more exposed surface of isolated flakes that offer more reaction sites for redox reactions than stacked multilayers. Here, a crucial aspect to emphasize is the oxidation of MXenes during electrochemical scanning. Lorecova *et al.* initially reported this kind of electrochemically triggered irreversible oxidation of $Ti_3C_2T_x$ in the positive potential window. Such an electrochemical oxidation is associated with the formation of a permanent $TiO_2$ layer (termed Ti-anodisation) during the initial anodic scan, atypically observed with an incredibly high anodic current ($I_a$) in the very initial scan (Fig. 6b).[159] This suggests that a negative potential window should be the practical scanning region for utilising pristine $Ti_3C_2T_x$ in sensing applications using standard procedures. Alshareef *et al.* further elucidated this aspect and associated this oxidation with the complete stabilization of unstable surface Ti atoms to the $Ti^{4+}$ valence state.[160] Overcoming this limitation, hexaammineruthenium(III) chloride $[Ru(NH_3)_6]^{3+/2+}$ can be utilised as an alternative redox probe for analytical applications. $[Ru(NH_3)_6]^{3+/2+}$ exhibited well-defined anodic and cathodic peaks in the negative window, precluding the need for sweeping in the positive region (Fig. 6c). Also lowering the pH to acidic levels results in a minimal oxidation current. Interestingly, Nb-based counterparts ($Nb_2CT_x$ or $Nb_4C_3T_x$) showed stability at an anodic potential up to 0.5 V.[161] Natalia *et al.* reported vacuum-filtered pristine MXene films for electrochemical sensing.[162] The cyclic voltammetry (CV) behaviour of film strips as working electrodes exhibited a stable response in the $[Ru(NH_3)_6]^{3+/2+}$ system with capacitive behaviour dominating the faradaic response (Fig. 6d). Relatively thinner electrodes obtained through spray coating on glass substrates (Fig. 6e) effectively reduce the capacitive response (Fig. 6f). This indicates that the thickness of MXene as an active material is a critical factor. An electrode with minimal thickness and a well-defined area is essential for achieving an electrochemical response suitable for sensing applications. In addition to horizontally stacked MXene sheets (as is typically the case with vacuum-filtered films or spray-coating), Hideshima *et al.* reported APTES functionalized vertically aligned (VA) nanosheets on the electrode surface by freeze-dried electrophoretic deposition.[163] The VA structure prevented the self-restacking of the sheets. Also, the high porosity (thus offering more electroactive area) of the VA architecture yielded an amplified CV signal, and enabled the sensitive determination of buckwheat BWp16 protein ($10^{-2}$–$10^{2}$ ng mL$^{-1}$). In addition, APETS-functionalized SL/FL $Ti_3C_2T_x$ has also offered a sensitivity of 37.9 μA ng$^{-1}$ mL$^{-1}$ cm$^{-2}$ towards carcinoembryonic antigen (CAE), a cancer biomarker.[164] Particular selectivity towards other disease biomarkers can be achieved in electrochemical sensors by functionalizing MXene sensors with specific biomolecules.[121] To date, the direct functionalization of MXene surfaces is scarce and requires a mediator, such as metal nanoparticles. Nonetheless, implementing modification strategies can enhance the noise levels and detection limits of the sensors, in addition to the added cost and time. Recent advancements have expanded the application of MXenes beyond $Ti_3C_2T_x$. For instance, $Nb_2CT_x$, $Nb_4C_3T_x$, $Mo_2CT_x$, and $Mo_2Ti_2C_3T_x$ MXenes have been used in an impedimetric electronic tongue (e-tongue) (Fig. 6g).[165] These MXenes showed remarkable sensitivity (1 nmol L$^{-1}$) towards neurotransmitter detection in complex matrices, such as contaminated urine, without requiring specific biorecognition elements. This highlights the versatility of MXenes in diverse sensor architectures, paving the way for their real-time clinical diagnostic applications. MXenes have also demonstrated potential for heavy metal ion sensing due to their intrinsically negative surface. Positive metal cations ($Cd^{2+}$, $Pb^{2+}$, $Cu^{2+}$, and $Hg^{2+}$) can interact effectively with the MXene surface and exhibit distinct voltammetric peaks. The detection limits were 0.1 mM for $Cd^{2+}$, $Pb^{2+}$, and $Cu^{2+}$, and 1 mM for $Hg^{2+}$.[166] MXenes such as $Ti_3C_2T_x$[167] and $Nb_4C_3T_x$[168] showed promise for determining bromate ($BrO^{3-}$) and lead ($Pb^{2+}$) ions. The potential of MXenes in HMI sensing is attributed to the robust and sensitive surface interactions driven by the charged nature of metal ions and the receptive properties of the MXene surface.

**Optical sensors:** Optical sensors offer numerous advantages such as simplicity, high throughput, and real-time detection. Compared to other 2D materials, the adjustable number of layers and variations in their composition (varying the M and/or X) provide tunable electronic and dielectric properties to MXenes. Such tunability gives rise to a broad range of optical absorption. Functional groups further enhance this tuability by inducing dipole and interfacial polarisation, while also facilitating profuse absorption of analytes. Studies have highlighted the potential of MXenes as a substrate for surface-enhanced Raman scattering (SERS) sensors. Gogotsi *et al.* investigated seven different MXenes ($Nb_2CT_x$, $Mo_2CT_x$, $Ti_2CT_x$, $V_2CT_x$, $Ti_3C_2T_x$, $Mo_2TiC_2T_x$, and $Ti_3CNT_x$), with each of them offering a distinct optical behaviour across the visible and near-infrared (NIR) range.[169] This variation in optical behaviour can be attributed to the unique transverse surface plasmon resonance of each composition and exhibits distinct enhancement factor (EF) values. MXenes demonstrated the capability to detect rhodamine 6G dye at concentrations as low as $10^{-7}$ molar. Notably, $Ti_3C_2T_x$ and $Ti_2CT_x$ displayed a higher EF, surpassing commercially available substrates, with $Ti_3C_2T_x$ outperforming AuNPs, showing sensitivity against various dyes (Fig. 7a and b). This highlights the versatility of the $Ti_3C_2T_x$ SERS substrates. Numerous other studies have also shown that MXene nanosheets exhibit extremely high optical transmittances (approximately 98%). However, there is an ongoing debate regarding the linear optical transmission of monolayer MXene, especially considering that MXene is at least three times thicker than monolayer graphene.

Conversely, MXene quantum dots (MQDs) with unique electronic and optical properties address several intrinsic limitations of MXene nanosheets (MNSs). For examples, the fluorescence quantum yield (FLQY) of MQDs is much higher than that of MNSs. Also, MQDs display excitation-dependent fluorescence, and the interaction of HMIs with surface groups can induce quenching or enhancement of fluorescence (FL) signals. Zhang *et al.* explored the behaviour of $Ti_3C_2T_x$ QDs (TQDs) for numerous HMIs ($Co^{2+}$, $Al^{3+}$, $Cu^{2+}$, $Cr^{3+}$, $Ca^{2+}$, $Mg^{2+}$, $Fe^{2+}$, $Fe^{3+}$, and $Pb^{2+}$) and reported the distinct fluorescence activity of each metal.[172] Such as $Al^{3+}$, $Ca^{2+}$, and $Mg^{2+}$ superimpose the FL intensity of TQDs and are classified as FL enhancers. Conversely, $Fe^{3+}$, $Fe^{2+}$, $Co^{3+}$, $Cu^{2+}$, $Pb^{2+}$, and $Cr^{3+}$ drastically reduce the output intensity and are referred to as quenchers. The FLQY of MQDs can further be improved by various modification (such as doping or surface passivation), leading to enhanced detection sensitivities compared to pristine MQDs. For example, Wan *et al.* reported APTES-functionalized MXene NS derived QDs (N-MQDs) with an average size of 8.63 nm (Fig. 7c).[170] N-MQDs exhibit a FLQY of 15.4% and show high sensitivity for detecting $Cu^{2+}$ ions over a concentration range of 0.5–500 μM with an LOD of 0.15 μM (Fig. 7d). Such approaches introduce additional reactive groups and result in a higher QY and a favourable environment for further biofunctionalization. Compared to fluorescence sensors for HMI detection, MQDs have proven to be more useful as optical probes for biomarker detection *via* the electrochemiluminescence (ECL) approach.

**Gas sensing:** The higher signal-to-noise ratio (up to two orders of magnitude) of MXenes compared to other 2D materials, make them suitable for gas sensing at ppb concentrations. Regardless of whether the gas is oxidised or reduced, MXenes respond positively by an increase or a decrease in channel conductivity.[173] Herein, surface engineering of MXenes plays a crucial role. Such as, the partial oxidation of $Ti_3C_2T_x$ MXene leads to ethanol detection at concentrations as low as $10^{-6}$ molar, much lower than those of pristine $Ti_3C_2T_x$ (Fig. 7e).[171] Upon heating, $TiO_2$ formation occurs that changes bandgap values of $Ti_3C_2T_x$ from 4.3 to 3.4 eV, hence inducing a potential

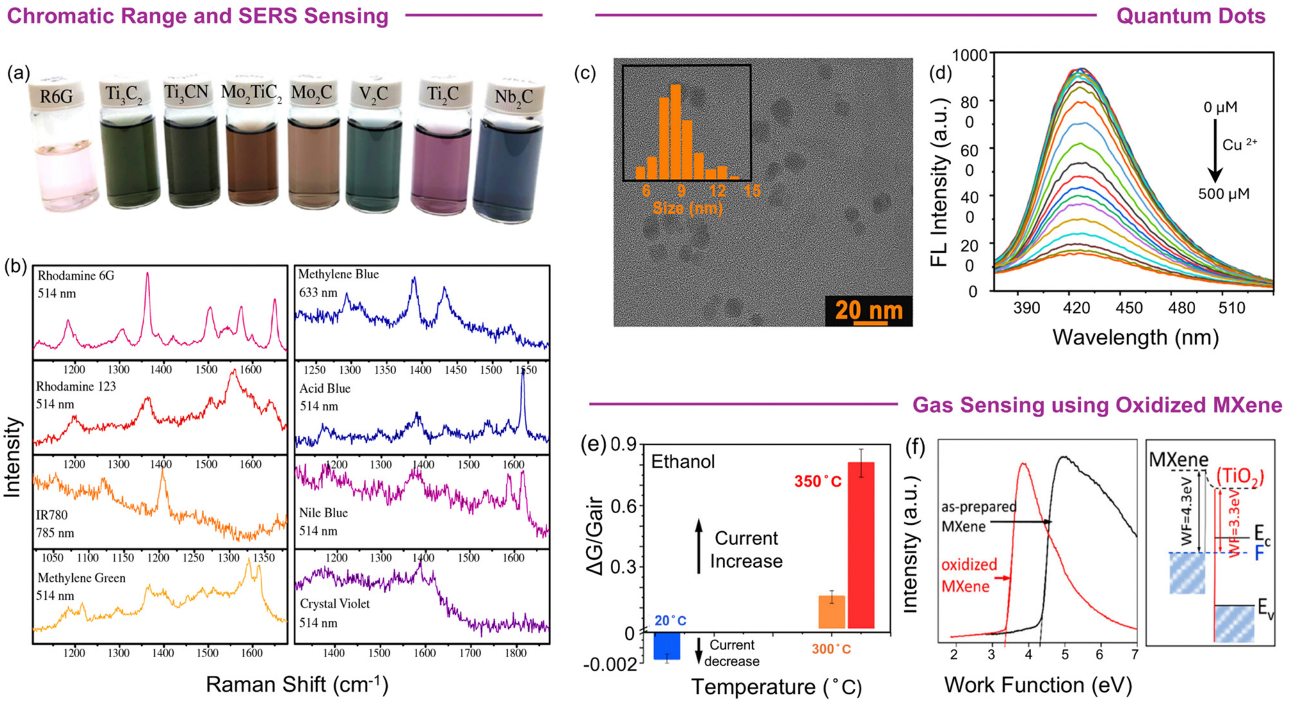

Fig. 7 (a) Optical image of R6G dye solution ($10^{-5}$ M) and seven different MXenes (<1 mg mL$^{-1}$), (b) SERS spectra of the $Ti_3C_2T_x$ substrate against different dyes at $10^{-7}$ M concentration. Reproduced with permission from ref. 169, Copyright © 2022, The Author(s), under exclusive licence to the Materials Research Society. (c) Transmission electron microscopy image and corresponding size distribution indicate a size of ~8.63 nm. (d) Variations in FL spectra at different concentration of $Cu^{2+}$ ions. Reproduced with Permission from ref. 170 Copyright © 2022, American Chemical Society. (e) Response of the $Ti_3C_2T_x$ gas-sensing channel at different annealing and measurement temperatures (f) variation in the work function and the band diagram of pristine and oxidised $Ti_3C_2T_x$ MXene. Reproduced with Permission from ref. 171 Copyright © 2020, American Chemical Society.

barrier of ~1 V (Fig. 7f). According to the band diagram, electrons from the MXene channel sink into $TiO_2$, while the induced potential barriers inhibit their backward diffusion. So, the adsorbed gas molecules dope the surface $TiO_2$ layers, transfers electrons, reduce the potential barriers and increase the conductivity. Nevertheless, this meaningfully explains why rutile or anatase $TiO_2$ significantly reduces the work function, supporting the advantageous effect of metal oxides on sensor performance. Other MXenes such as $V_2CT_x$ have also been utilised for gas sensing. In addition to the composition and degree of oxidation, flake thickness and hybrid configuration also have a significant impact on the gas-sensing properties of MXenes.[173]

### 4.3. Drug delivery and gene therapy

Nanotechnology plays an important role in advanced drug delivery systems; for example, the development of smart nanocarriers based on 2D sheets is gaining interest in advanced drug delivery for various therapies—and nanovehicles for aptamers and DNAzymes in gene editing (Fig. 8). Controlled drug administration is advantageous for improved photothermal ablation of tumor cells and contrast imaging. Traditional clinical treatments involve surgery and radiotherapy, but these methods often reduce patients' life quality and survival rates because of surgical complications, radiation side effects, and high recurrence rates. Additionally, the complexity and diversity of tumors diminishes the effectiveness of conventional treatments. So, multiple therapeutic combinations are preferred to enhance anticancer activity, reduce toxicity, and overcome drug resistance. MXenes have been extensively investigated as carriers for small molecules, with a particular focus on the delivery of chemotherapeutic agents for cancer treatment. Among these advancements, MXenes can function as an ideal matrix with high loading capacity, and their external stimuli-sensitive nature facilitates guided drug release, making them an intelligent vehicle for precision medicine. For example, $Ti_3C_2T_x$ MXenes showed pH-responsive release of chemotherapeutic drugs, such as doxorubicin (DOX), with a high release profile at acidic pH (~4.5).[145,174] MXene nanosheets have also been reported to co-host proteins, glucose oxidases, and chloroperoxidases, leading to MXene/enzyme drug systems (MXene-based bionic cascaded-enzyme nanoreactors) for enzyme dynamic therapy.[175] As discussed above, surface modification with polymers to create highly stable and biocompatible platforms is one of the strategies used to incorporate MXenes into drug delivery (Fig. 7). Polyethylene glycol (PEG) modification is considered an effective route to overcome MXene precipitation; for example, $Ti_3C_2$ aggregation in phosphate buffer solution (PBS) and Dulbecco's modified Eagle medium (DMEM). PEGylated $Ti_3C_2$-MXene behaves as an efficient carrier of DOX.[176] Acidic conditions reduce the ionic interactions between DOX and MXene-SS-PEG (SS; cystamine dihydrochloride disulfide), which leads to the release of the DOX drug from the MXene surface.[174] In addition, polyvinylpyrrolidone (PVP) polymer functionalization,[176,177] ionic liquids[178] and other materials[179] have shown the potential in regulating their drug release profile. In addition,

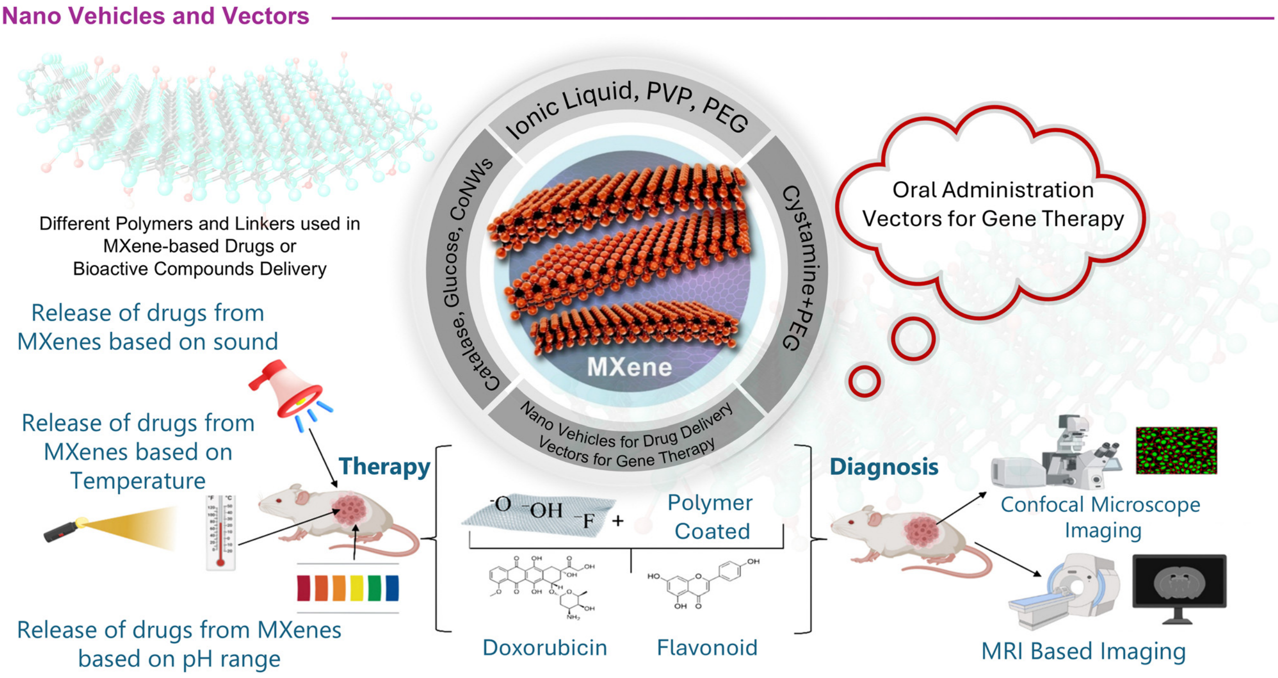

Fig. 8 Schematic presention of different surface modification strategies involved in MXene based drug delivery systems and other potential applications. Reproduced with Permission from ref. 179 © 2024, Controlled Release Society.

decorating MXene sheets with cobalt nanowires (CoNWs) also increases the drug-loading capacity of $Ti_3C_2T_x$ flakes.[180] Herein, electrostatic interactions facilitated the loading of DOX over CoNWs@$Ti_3C_2T_x$, and these interactions reduced as the pH is decreased to an acidic level, thereby facilitating drug release. Despite rapid advancements in MXene research, its potential for oral drug delivery, particularly in controlled release systems for therapeutic proteins, remains unexplored. A notable study by Seitak *et al.*[181] demonstrated the potential of MXene to load the therapeutic protein catalase with an efficient pH-responsive release. This marks an important step toward the use of MXenes in oral drug delivery platforms. Also, the biocompatibility of MXene-based nanocarriers and their ability to effectively load and deliver catalase protein, a high-molecular-weight macromolecule, highlight their potential for oral drug delivery.

Advances in genomics and gene therapy have the potential to address many diseases historically considered untreatable. However, the clinical translation of these technologies faces significant challenges such as achieving precise and efficient regulation of genetic information. This also helps in developing safe and effective delivery vectors for therapeutic payloads. MXenes also show significant promise in biomedicine as vectors for gene therapy, addressing issues associated with other nanomaterials, such as lower loading capacity. Moreover, as non-viral alternatives, MXenes also reduce immunogenicity and toxicity hazards with versatility in delivering diverse genetic materials, such as the Cas ribonucleoprotein (RNP) complex, miRNA, and DNA. Their multifunctionality also extends to theranostic applications by combining therapy with real-time monitoring, thus making them powerful tools for advancing gene therapy and precision medicine. Wang *et al.* demonstrated DNA-functionalized stimuli-responsive MXene systems for controllable genome editing. By leveraging the photothermal conversion properties of MXenes, nucleic acid strand displacement was triggered by NIR irradiation, enabling precise release of Cas ribonucleoprotein complexes based on the intensity of the incident NIR light.[182] This approach integrates external signals as triggers, thereby providing a programmable platform for *in vivo* therapeutic genome editing using MXenes as nanocarriers. A persistent challenge in non-viral gene delivery, including CRISPR systems, is achieving sufficient transfection efficiency, which can be addressed by MXene composites and tailored surface functionalization.[183] By enhancing delivery efficiency and overcoming the limitations of non-viral methods compared to viral vectors, MXene-based systems offer a promising alternative for advanced gene therapy. However, their potential gene therapy remains unexplored, and only a few studies have highlighted their capabilities. Proper functionalization of MXenes can satisfy various therapeutic needs, for instance, realizing advanced stimuli-responsive systems to release therapeutic agents under external triggers, such as temperature, external electric stimuli, magnetic stimuli, or ultrasound, this ensuring noninvasive, localized, and controlled delivery. Advances in nanomanufacturing are also important to further support the scalability and reproducibility of these systems. These advancements increase their clinical translatability, and establish MXenes as promising platforms for next-generation biomedical applications.

### 4.4. Biomedical imaging

Photoacoustic (PA) imaging involves the absorption of non-ionising laser pulses by the biological tissues, causing thermal

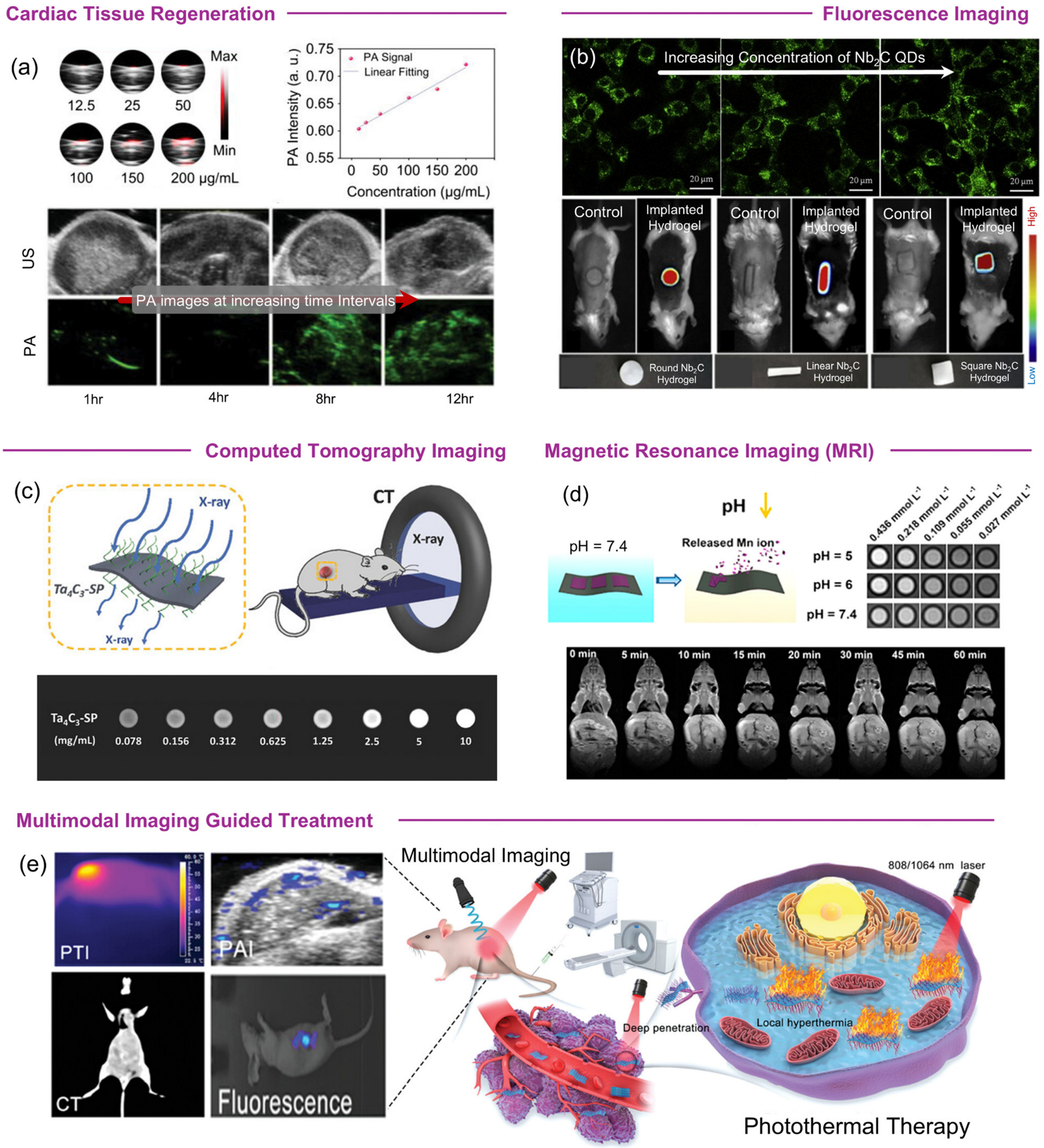

Fig. 9 (a) Concentration- and time-dependent acoustic signal generation of V$_4$C$_3$T$_x$/ATO@BSA for enhanced photoacoustic imaging. Reproduced with Permission from ref. 184 © 2023 Wiley-VCH GmbH. (b) Nb$_2$CT$_x$ QDs hydrogel-administered mice for high-resolution cellular imaging. (Top) FL images at different concentrations (100–200 μg mL$^{-1}$) monitored for 4 hours and (bottom) pseudo-color images of different shapes show that the administered hydrogel remained intact without disturbing the tissues. Reproduced with Permission from ref. 185, © 2020 Published by Elsevier B.V. (c) Computed tomography imaging technique and *in vivo* CT images using Ta$_4$C$_3$T$_x$ MXenes at different concentrations showing contrast enhancement. Reproduced with Permission from ref. 186, © 2017 Wiley-VCH Verlag GmbH & Co. KGaA, Weinheim. (d) pH and concentration dependent *in vitro* MRI with MnO$_x$/Ti$_3$C$_2$T$_x$-SP hybrid nanosheets for T1-weighted imaging. Reproduced with Permission from ref. 146 © 2017, American Chemical Society (e) combined modality imaging showing the versatility of MXenes in integrated diagnostic approaches. Reproduced with Permission from ref. 187, © 2021 The Authors. Advanced Science, published by Wiley-VCH GmbH.

expansion, and subsequent generation of photoacoustic signals. These signals are then converted into a light-absorption distribution image. This method leverages the low attenuation coefficients of tissues and address the limitations of traditional optical imaging. Unlike conventional MAX phases, MXene sheets display semimetal-like bandgaps, offering localised surface plasmon resonance (LSPR) effects. High photothermal conversion efficiencies (PTCEs) and strong absorption of $Ti_3C_2T_x$, $Ta_4C_3T_x$, and $Nb_2CT_x$ MXenes make them promising contrast agents (CAs) for PA imaging. Furthermore, the acoustic response of MXenes to near-infrared (NIR) light excitation is sufficiently large to be used for in-depth tissue imaging, an area where typical CAs provide low resolution.[20] V-based MXene nanosheets demonstrated efficient photothermal absorption and good PA signals within the NIR region, making them highly effective for PA imaging-assisted cancer therapy both *in vitro* and *in vivo* (Fig. 9a).[184] This implies that MXenes are suitable for combined PA imaging and photothermal therapy (PTT), enabling real-time disease monitoring and treatment (an area known as theranostics).

Another important application is fluorescence imaging (FLI) of biological events at the molecular level. The usual morphology of MXenes provides a low luminescence effect in aqueous solution. So, introducing fluorescent species to the surface of MXenes can effectively improve their FL emission properties. Such as, the electrostatic adsorption of the cationic fluorescent drug DOX, and its autofluorescence effect have been exploited for both bioimaging and anticancer therapy.[188] Another approach involves the preparation of luminescent MQDs. Compared to typical MQDs, titanium nitride QDs ($Ti_2NT_x$ QDs) exhibited high PTCE upon NIR irradiation. The PA signal of $Ti_2NT_x$-QDs exhibited linearity with concentration and the enhanced permeability and retention (EPR) effect, ensuring rapid accumulation in tumour tissues. $Nb_2C$ QDs have been designed to exploit their unique luminescence properties.[185] MQDs demonstrate excitation-dependent photoluminescence, making them well suited for multicolour cell imaging (Fig. 9b). Their excellent biocompatibility, anti-photobleaching, and high FLQY make them attractive for FLI applications. However, a clear mechanism behind their luminescence behavior is still under debate. Still, the two main hypotheses are the size effect and surface defects (or surface passivation). Size- and surface-chemistry-dependent luminescence nature of MQDs enables the tuning of the emission wavelengths, ensuring a wide range of fluorescent probes for different imaging needs. For example, defect-induced luminescence and size-effect-induced quantum confinement in $Ti_3C_2T_x$ and $Nb_2CT_x$ MXene QDs have been exploited for cell imaging and labelling.[185] Convincingly, the small size of MQDs offers easy diffusion into biological tissues, thus providing detailed images at the cellular level. This indicate MQDs utility for monitoring cellular processes, visualising tumour boundaries, evaluating the delivery and effectiveness of therapeutic agents in real-time.

On the other hand, $Ta_4C_3T_x$[186] and $W_{1.33}CT_x$,[187] have shown potential as a contrast agents in computed tomography (CT) imaging. CT relies on the absorption of X-rays by various tissues in the body, and compared to traditional iodine-based CAs, high atomic numbers of MXenes (Ta = 73, $W = 74$) and their large X-ray attenuation coefficients offer improved image contrast (Fig. 9c), facilitating clear visualisation of fine anatomical structures and abnormalities. Enhanced contrast aids in accurate diagnosis, particularly in early-stage diseases when tumour morphology and pathological changes are needed to be monitored. In addition, the functionalization of MXenes (*e.g.* $Ta_4C_3T_x$-SP) with target molecules enables stability and targeted imaging of the tissues, allowing for more precise and personalised clinical diagnoses.

MRI is a non-invasive imaging technique with high contrast and its deep tissue penetration and provide high-resolution images. Studies have explored MXenes as MRI contrast agents for fine images with minimal toxicity. For instance, $MnO_x/Ti_3C_2T_x$ hybrid nanosheets have been developed as pH-sensitive MRI contrast agents, showing enhanced T1-weighted *in vivo* imaging of tumour-bearing mice (Fig. 9d).[146] This highlights that Mn-based CAs are safe alternatives to Gd-based agents, with improved imaging sensitivity.[146] MXenes combined with iron oxide nanoparticles showed great potential for use in T2-weighted MRI.[20] This indicates that functionalized MXenes with targeting ligands can enable the production of efficient MRI agents to accurately highlight specific tissues or pathologies, which is crucial in oncology for precise tumour localisation and characterisation. While, the multifunctionality of MXenes renders them ideal MRI contrast agents as magnetic properties can be modulated through surface modification and hybridisation.[189] Their strong luminescence, high photothermal conversion efficiency, high fluorescence yield, and good biocompatibility for PA, CT, and MRI imaging instigate the use of MXenes in multimodal imaging-guided treatment (Fig. 9e).[187] However, further research is required to address several important aspects, including long-term *in vivo* biocompatibility, physiological stability, and clinical evaluation, to better understand MXenes' potential for real-life applications.

### 4.5. Synergistic therapeutics

Photothermal therapy (PTT), involves the use of a photosensitive substance that transforms light into heat and destroys malignant cells. It is preferable to use NIR light, termed as ''biological window'', because its established tissue penetration is greater than that of visible light. MXenes are excellent candidates for PTT owing to their intrinsic absorption capacity and efficient light-to-heat conversion in NIR region. For instance, $Ti_3C_2T_x$ have demonstrated remarkable *in vivo* photothermal effects upon NIR irradiation and effective tumour ablation.[23] Notably, most PTT agents exhibit an absorption peak in the first biological window (NIR-I biowindow, 750–1000 nm), including $Ti_3C_2$ as described earlier. However, the maximum laser power density for safe human skin exposure and penetration depth were higher for the second biological window (NIR-II, 1000 nm–1350 nm) than for NIR-I. Another crucial aspect in PPT therapy is the sufficient drug loading and precise release at the tumor site. As we discussed before, the surface of MXene behave as a spacious matrix for drug loading (*e.g.*, DOX loading capacity of $\sim$211.8% w/w in the case of modified $Ti_3C_2T_x$ MXene)[20] and suitable modifications for

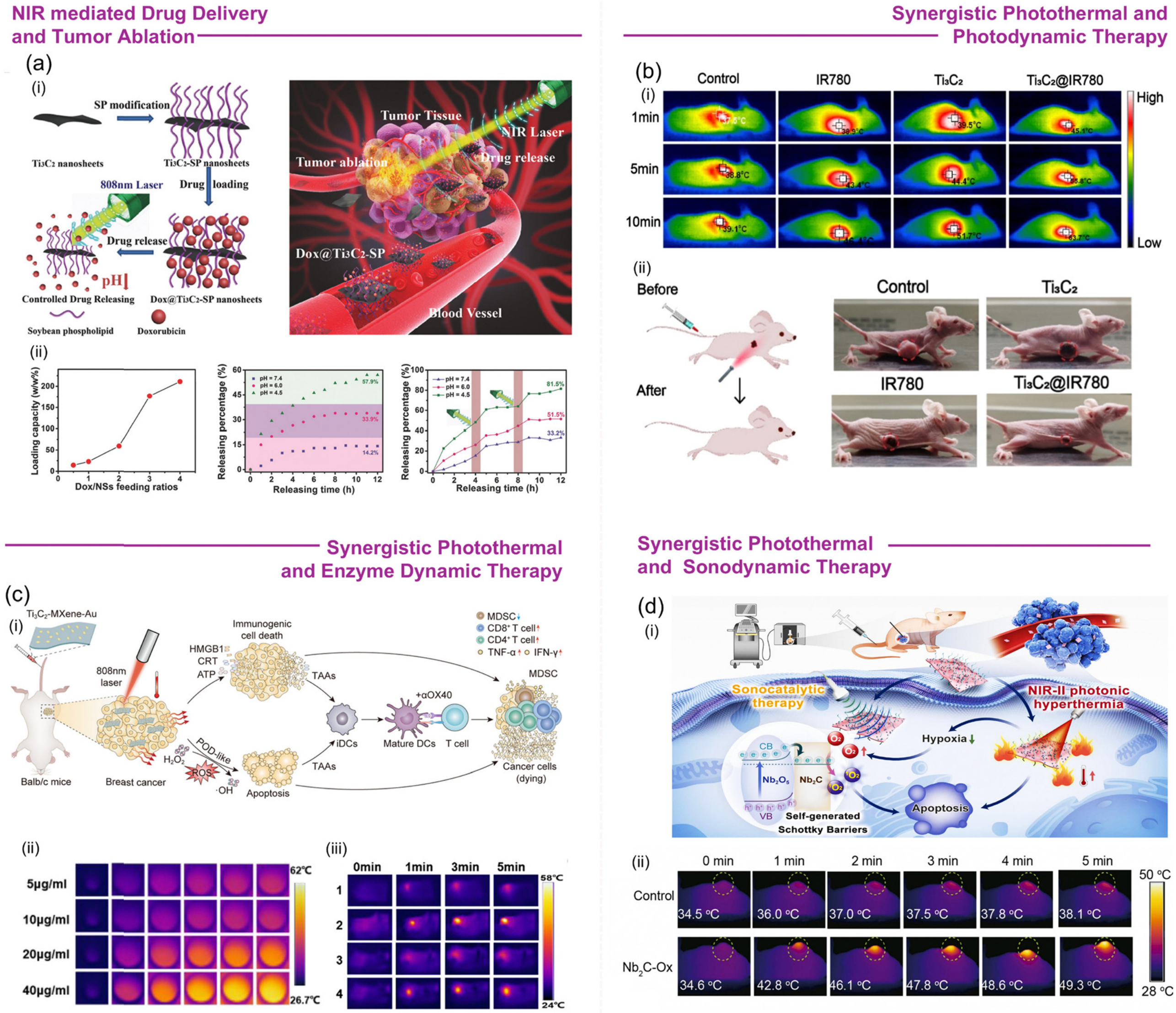

Fig. 10 (a-i) SP surface modification and DOX loading of $Ti_3C_2T_x$ MXene nanosheets (left). Controlled drug release and *in vivo* NIR-triggered photothermal ablation of cancer cells (right). (a-ii) Drug loading capacity curves and time-dependent drug release under varying pH conditions with or without laser irradiation (808 nm). Reproduced with permission from ref. 145 © 2018 Wiley-VCH Verlag GmbH & Co. KGaA, Weinheim. (b-i) *In vivo* photothermal response of $Ti_3C_2$@IR780 nanocomposites illustrating locally induced hyperthermia upon NIR laser irradiation. (b-ii) Schematic representation of tumour injection and the group of tumour-bearing mice showing significant growth inhibition by the $Ti_3C_2$@IR780 system. Reproduced with permission from ref. 190 © 2022, The Authors. Published by Elsevier Ltd. (c-i) Schematics of the Au@$Ti_3C_2$ system for photothermal and immune synergistic therapy (c-ii) photothermal response of different concentrations of Au@$Ti_3C_2$ upon 808 nm laser irradiation, and (iii) photothermal response (IR images) of Au@$Ti_3C_2$ at the tumour site after different irradiation periods demonstrating superior hyperthermia activity. Reproduced with permission from ref. 191 © 2022, American Chemical Society. (d) Schematic representation of sonodynamic therapy with $Nb_2C$ MXene nanosheets, demonstrating ultrasound-induced ROS generation and tumour cell apoptosis. Infrared images of 4T1 bearing mice irradiated with 1064 nm laser irradiation after intravenous injection of Ox-$Nb_2C$. Reproduced with permission from ref. 192 © 2023 Elsevier Ltd. All rights reserved.

controlled release. By synergistically combining such features, DOX loaded SP@$Ti_3C_2T_x$ MXene (Fig. 10a-i) demonstrated pH-sensitive drug delivery and NIR-triggered on-demand drug release (Fig. 10a-ii).[145] Such integrated platforms highlight effective encapsulation and release of therapeutic agents for targeted therapies.[20]

Photodynamic therapy (PDT) involves NIR light-activated photosensitisers and facilitates cytotoxic ROS generation. This is followed by localised oxidative stress, leading to noninvasive cell death. MXene reported to have the potential for ROS generation under specific irradiation conditions.[23] Lin *et al.* examined $Ti_3C_2T_x$ modified with a NIR-sensitive photosensitizer "IR780" ($Ti_3C_2T_x$@IR780) for targeted PTT and PDT.[190] *In vivo* studies have demonstrated that $Ti_3C_2T_x$@IR780 can efficiently accumulate at tumour sites and NIR exposure for 10 min increases the tumour surface temperature to 63.7 °C (sufficient for the ablation) (Fig. 10b-i). Furthermore, $Ti_3C_2$@IR780 showed higher ROS generation, which disrupted mitochondrial activity and caused apoptosis in ∼60.51% of tumour cells, significantly inhibiting tumour growth in tumour-bearing mice (Fig. 10b-ii). This implies that high PTCE of MXenes ensure maximum therapeutic effects with minimum damage to healthy tissues. Multifunctional nanoplatform based on Au@$Ti_3C_2T_x$ nanocomposites,[191] combines photothermal properties and peroxidase-like activity, enabling *in vivo* dual-mode thermal and PA imaging, as well as synergistically combining PTT and enzyme dynamic therapy (EDT) (Fig. 10c-i). Au@$Ti_3C_2T_x$ displayed a concentration-dependent PTCE under 808 nm laser irradiation and locally increased the temperature to 62 °C (Fig. 10c-ii). Compared with the control groups, the high temperature induced by Au@$Ti_3C_2T_x$ proved sufficient for local hyperthermia (Fig. 10c-iii). Au@$Ti_3C_2T_x$ facilitate EDT followed by generating cytotoxic ROS through enzyme-catalyzed intracellular reactions and ultimately inducing cell apoptosis. This triple PTT/EDT/immune therapy proposes a potential pathway to empower the immune system to fight cancer by directly destroying tumour cells.

Sonodynamic therapy (SDT) is another non-invasive cancer treatment that uses ultrasound-sensitive sonosensitisers to produce ROS and effectively destroy cancer cells.[20] Unlike PDT and PTT, SDT can deeply penetrate at tumour tissue but often struggles with hypoxic environments and ineffective sonosensitisers. Conventional photosensitizers typically produce similar ROS levels under ultrasound irradiation; also, their hydrophobicity and high phototoxicity can limit absorption. This negatively affect pharmacokinetics and SDT effectiveness. Studies have shown that oxidised MXene nanosheets display sonodynamic effects and rapidly generate ROS under ultrasonic irradiation, making them effective sonosensitisers for tumour therapy. Xu *et al.* reported oxidised niobium carbide (Ox-$Nb_2CT_x$) MXenes as sonosensitisers.[192] Under ultrasound irradiation, the close interfacial contact of *in situ* heterojunctions promotes rapid electron–hole pair separation in Ox-$Nb_2CT_x$ and prevents further carrier recombination. As a result, the Ox-$Nb_2CT_x$ nanosheets exhibited strong sonodynamic effects and produced abundant ROS to destroy tumour cells (Fig. 10d-i). This study suggests that even with mild oxidation, the intrinsic photothermal capacity of Ox-$Nb_2CT_x$ MXenes is not affected, and photonic hyperthermia is achieved in the NIR-II biowindow (Fig. 10d-ii). Localised hyperthermia is also known to improve oxygen supply in tumour microenvironments, thus increasing the effectiveness of stem cell therapy in tumour eradication. For example, Ox-$Ti_3C_2T_x$ increases the sonodynamic performance by approximately 3.7-fold compared to untreated $Ti_3C_2T_x$, making it a safe and effective sonosensitiser for cancer therapy.[20] Alternative methods consist of decorating MXenes with carbon dots (CDs) to form heterojunctions, thereby enhancing carrier transfer and reducing tumour hypoxia, thus improving SDT by inhibiting antioxidant enzymes.[193] MXene-based platforms also utilise chemo-dynamic therapy (CDT). CDT uses metal ions to trigger Fenton reactions and produce cytotoxic hydroxyl radicals. For this purpose, MXenes with a high metal content are good candidates *e.g.*, $Ti_3C_2T_x$ quantum dots show activity similar to that of the Fenton reaction in CDT, effectively inhibiting tumour growth and maintaining biocompatibility.[20]

These developments highlight the versatility and incredible synergy of MXenes in therapeutic applications. To date, MXenes have emerged as competitive candidates for the development of advanced therapeutic strategies. Further experiments on the long-term toxicity of these nanomaterials should be conducted in light of appropriate standardised integration and activation strategies. As research continues, MXenes are expected to have a major impact on the future of biomedical and clinical treatments.

### 4.6. Regenerative medicine

Regenerative medicine seeks to replace, engineer, or regenerate human cells, tissues, or organs to restore their functionality. Cardiovascular diseases, particularly myocardial infarction (MI), are leading causes of morbidity and mortality. Traditional cardiac patch repair with sutures or staples can cause bleeding and inflammation, whereas, insulating properties of fibrotic tissue disrupt signal transmission, causing ventricular arrhythmias and potentially fatal heart failure. So, conductive and adhesive biomaterials are required to enhance cardiac repair. MXenes show promise as conductive biohybrid platforms, promoting cardiomyocyte proliferation, while maintaining their growth and alignment. MXenes's ability in cardiac tissue engineering is driven by their potential to mimic the electrical conductivity of native cardiac tissues.[194] MXenes facilitate the propagation of electrical impulses across cardiomyocytes, thereby underpinning synchronous beating/contractility and reducing the risk of post-MI arrhythmias. Recently, Lee *et al.* developed an conductive and adhesive hydrogel (CAH) using $Ti_3C_2T_x$ alongwith gelatin and dextran aldehyde (dex-ald).[194] This paintable CAH patch demonstrated stable adhesion to the epicardium and sufficient characteristics for cardiac tissue regeneration, without the need for sutures (Fig. 11a-i). Monitoring the pathological fibrosis of an infarcted heart treated with CAH cardiac patches indicated a decrease in fibrosis on left ventricular (Fig. 11a-ii), indicating that mechanical support and electrical conductivity of the CAH prevent structural remodelling of the infarcted heart.

Moreover, injuries to the peripheral and central nervous systems lead to significant functional loss and limited natural regenerative capacity. Neural tissue engineering leverages biomaterials to facilitate nerve-cell interactions and regeneration. The conductive properties of MXenes also support neural cell growth and differentiation,[197] promote neurite outgrowth while maintaining the electrical conductance of the extracellular matrix with an improved neural transmission. Guo *et al.* investigated the effects of $Ti_3C_2T_x$ films on mouse neural stem cells (NSCs).[195] Compared to traditional tissue culture polystyrene (TCPS), NSCs on MXene films showed stable adhesion, enhanced proliferation, and more synchronised network activity (Fig. 11b-i). MXene films notably improve neural differentiation, leading to longer neurites, increased branching points and terminals, thereby supporting normal synapse development. In addition, the film, combined with electrical stimulation, further enhanced NSC proliferation (Fig. 11b-ii). These results suggest that $Ti_3C_2T_x$ MXene is a promising interface for

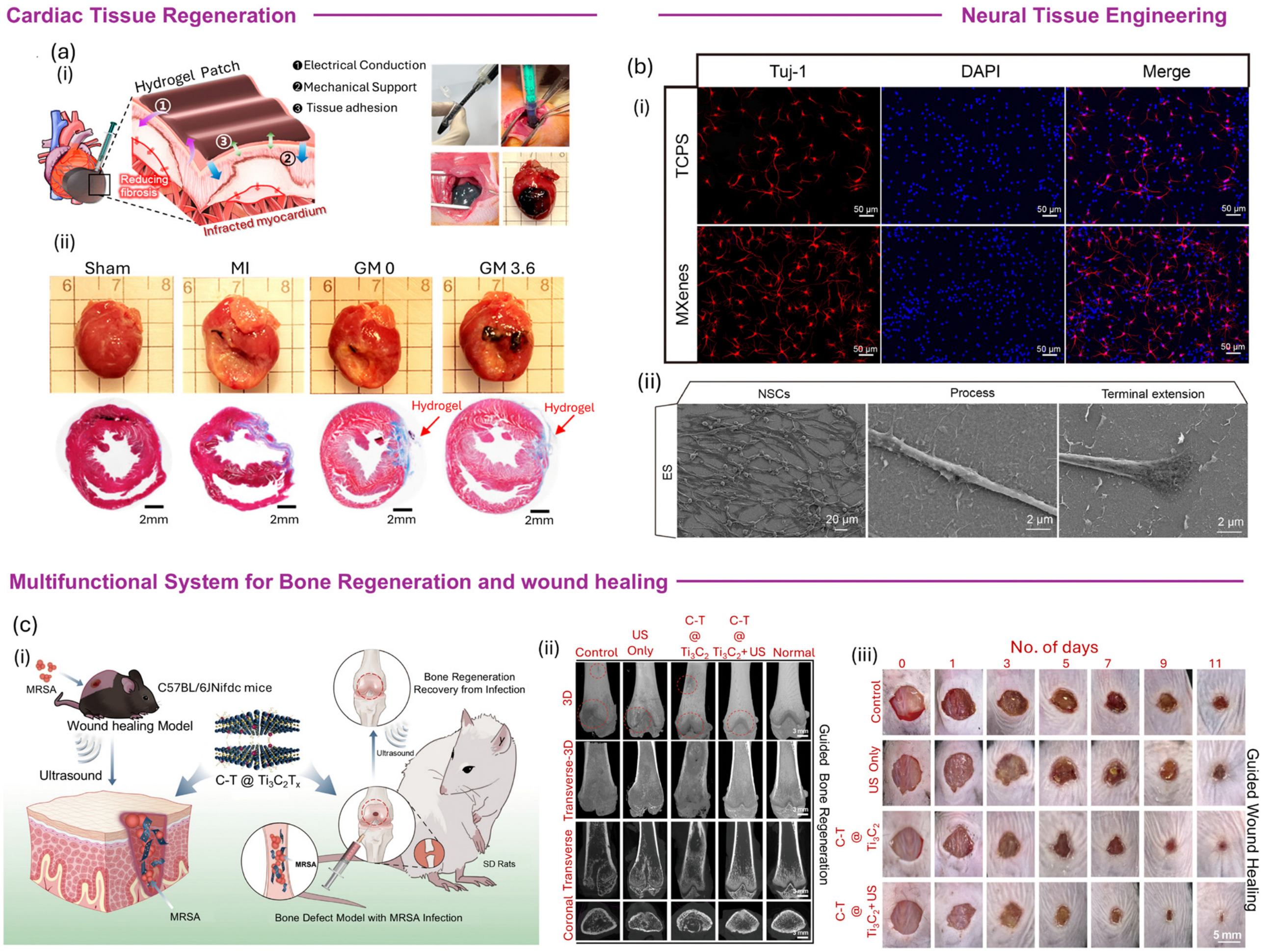

Fig. 11 (a) Paintable MXene-based multifunctional conductive and adhesive hydrogel (CAH) patches for infarcted heart repair (left). Mixing of MXene-gelatin and dextran aldehyde (dex-ald) for MXene-CAH fabrication and injection into the beating epicardium (right). (b) Gross anatomy of the progression of infarcted heart tissue repair and Masson's trichrome staining images showing the efficacy of MXene-CAH (GM3.0). Reproduced with Permission from ref. 194 © 2023, American Chemical Society. (b-i) Application of $Ti_3C_2T_x$ MXene in neural tissue engineering, highlighting neural cell differentiation, and (b-ii) the effect of electric simulation (10 V, 188–313 Hz, 25 μ pulses, 10 min for 3 days) on NSCs-$Ti_3C_2T_x$ demonstrated stable adhesion and effective proliferation. Reproduced with Permission from ref. 195 © 2020 Acta Materialia, Published by Elsevier Ltd. (c-i) Application of MXenes as a multifunctional system for bone regeneration and wound healing. (c-ii) Monitoring of mouse femur bone *via* micro-computed tomography views in different groups after four weeks of treatment. (c-iii) *In vivo* wound healing monitoring of MRSA-infected mice, highlighting their antimicrobial properties and enhancing cell proliferation at the wound site. Reproduced with Permission from ref. 196 © 2023, Springer Nature.

proliferation, differentiation, and maturation of NSC-derived neurones.

Similarly, bone regeneration and wound healing are two important aspects of regenerative medicine. Bone defects pose a significant clinical challenge owing to the slow self-healing capability of bones. MXene-incorporated scaffolds enhance osteoblast activity in both *in vitro* and *in vivo* bone-regeneration models. In addition, their electrical conductivity can stimulate bone cell activity, further promoting bone regeneration. $Ti_3C_2T_x$ nanocomposites (with hydroxyapatite, and sodium alginate) scaffolds produced *via* extrusion-based 3D printing have shown excellent cell adhesion, migration, proliferation, and differentiation, resulting in bone tissue formation.[20] Yu *et al.* introduced a $CaO_2$-$TiO_x$@$Ti_3C_2T_x$ composite (C-T@$Ti_3C_2T_x$) as a multifunctional nanocatalyst to treat bone defects and prosthetic joint infections (Fig. 11c-i).[196] Analysis of methicillin-resistant *Staphylococcus aureus* (MRSA)-induced cavitation in rat femurs showed that the C-T@$Ti_3C_2T_x$ group exhibited superior bone healing. Also, the ultrasound-treated femur samples exhibited new bone tissue and a significant reduction in the defect area on micro-CT analysis (Fig. 11c-ii). It is well known that the accumulation of calcium ions ($Ca^{2+}$) promotes osteogenic transformation and enhances bone repair. Moreover, the antibacterial properties of MXenes inhibit osteomyelitis and accelerate healing. To this end, scaffolds support the migration of mesenchymal cells, nutrient transport, and vessel ingrowth, thereby creating an appropriate osteogenic environment.

For wound healing, an ideal dressing should be able to maintain a constant temperature, promote proliferation, and antimicrobial activity. A combination of the antimicrobial and cell proliferation/differentiation-enhancing activities of MXenes makes them suitable for wound healing applications. C-T@$Ti_3C_2T_x$ also exhibits sonodynamic capabilities, with $CaO_2$ inducing the *in situ* oxidation of $Ti_3C_2T_x$ to form acoustic-sensitising $TiO_2$ on its surface.[196] Furthermore, the chemodynamic properties enhance the ROS generation and Fenton reactions during the sonodynamic treatment, resulting in effective antibacterial activity and improved wound healing (Fig. 11c-iii). In addition, MXene-based hydrogels promote faster wound healing by providing an efficient environment for cell growth while reducing bacterial infections.[198] Simultaneously, the MXene hydrogel forms a moisturised environment for wound healing. The *in vivo* experiment conducted thereafter showed that this system could promote tissue regeneration and accelerate wound healing to a degree beyond commercial films or standard cellulose hydrogels.

The aforementioned investigations have highlighted the bright future of MXene-based biomaterials for bone and soft tissue defects. However, the synergistic effects of MXene photothermal properties in tissue regeneration and the systematic verification of the mechanisms underlying tissue regeneration mark drastic milestones in the field of regenerative medicine.

### 4.7. Wearable and point-of-care devices

Wearable point-of-care (PoC) devices are revolutionising medical diagnostics with on-site detection and general health monitoring. Wearable sensors track metabolic changes by monitoring body temperature, physical movements, and vital signs for real-time monitoring of human health. MXenes are ideal for such applications because of their mechanical and electronic properties.[199] Recently, Yu *et al.* introduced an MXene-based wearable wireless sensor for automated electrochemical monitoring of female hormones (Fig. 12-i and ii).[200] The flexible working electrode contains single-stranded DNAs (ssDNAs) immobilized on gold nanoparticle-decorated MXene (AuNPs-MXene), and an oestradiol-selective DNA aptamer for target recognition of oestradiol with sub-picomolar sensitivity. Furthermore, an array of multiplexed inkjet-printed sensors within the microfluidic sensing reservoir enables the accurate quantification and calibration of the analyte (Fig. 12-iii and iv). Such fully integrated wireless prototypes support home monitoring of reproductive hormones and can be customised for personalised medicine.

Advanced healthcare technologies aim for wireless, battery-free biosensors for continuous and real time health monitoring.[203] Their low invasiveness and ability to facilitate remote patient observation significantly reduces the burden on healthcare systems. Shi *et al.* developed a battery-free, wearable smart bandage consisting mainly of a flexible circuit board and an electrode array as shown in Fig. 12b-i.[201] Based on clinical evidence, *Sortase aureus* and *Pyocyanin aeruginosa* are the most common bacteria causing wound infections. A smart wound-dressing system (Fig. 11b-ii) monitoring the virulence factors of these two bacteria can provide real time insights into wound healing process. A smart bandage can send signals by adhering to the skin and forming a connection with the wound (Fig. 12b-iii). This approach overcomes the limitations of conventional rigid lithium batteries and bluetooth modules by harvesting energy using NFC-enabled mobile devices with functionality in both flexible and rigid configurations (Fig. 12b-iv). In metabolite disorder management, MXene-based sensors detect metabolites such as glucose and lactate in body fluids. These sensors are especially useful for controlling diabetes, which requires continuous monitoring of the blood glucose levels.[204] Among the MXene-based PoC devices, some have been reported to detect biomarkers related to cardiovascular diseases. For example, sensors that measure troponin levels are potential indicators of an oncoming heart attack and raise alarms for timely medical intervention. Thus, their ease of use and portability makes them suitable for emergency and remote settings.[205] MXene nanosheets have been integrated into microneedle systems for monitoring muscle movements, demonstrating potential in detecting neuromuscular abnormalities.[206] However, coating MXenes over polymer microneedles in a reproducible manner is a difficult task. The recent approaches by Rosati *et al.*[207] on inkjet-printed Ag-microneedles can be promising for fabricating similar MXene-based systems with improved control and reproducibility.

Incorporating MXenes into textiles enables smart electronic fabrics for heart rate monitoring, respiration, and muscle activity, thereby significantly benefiting the sports medicine, healthcare, and rehabilitation sectors. These wearables track physical performance, hydration, and fatigue in sports and fitness, aiding athletes in optimising training and minimising injury risk. For example, sweat sensors continuously update electrolyte balance and dehydration status which is crucial to maintain consistent performance during the peak activity.[208] A range of electrochemical aptasensors have been developed based on MXene for monitoring cancer biomarkers, such as 5-hydroxymethylcytosine and carcinoembryonic antigen, with high sensitivity, selectivity, and decent potential for associated clinical applications.[209] These advances highlight the potential of MXenes as flexible wearable sensors for human health monitoring. For commercial success, multidisciplinary research and innovative approaches are still in their infancy to harness the full potential of MXene-based wearable devices. Recently, Inman *et al.*[202] reported a stand-alone MXene coil (MX-coils)-integrated textile (e-textile) to harness wireless charging and real-time data transmission (Fig. 12c-i and ii). MXene e-textile wirelessly powered an integrated EMG sensor to record human neuromuscular activity (*i.e.*, surface electromyography sEMG sensing). Relying solely on the wirelessly transmitted power from the MX-coils to charge the attached supercapacitor and simultaneously powering the EMG sensors allows real-time monitoring of bicep sEMG activity (Fig. 12c iii–v). In addition to sEMG monitoring, MX-coils can power a commercial wireless sensing system to monitor the temperature and humidity (Fig. 12c-v). This study presents an effective strategy for developing textile-based sensors and underscores the importance of designing all-MXene biosensors that integrate sensing, wireless power, and data transmission in a standalone configuration, as demonstrated in other studies.[203,210]

### 4.8. Bioelectronic implants for multimodal interventions

Flexible bioelectronic interfaces show great promise for the high-precision mapping and manipulation of excitable

**Wearable Nanobiosensor for Hormone Monitoring**

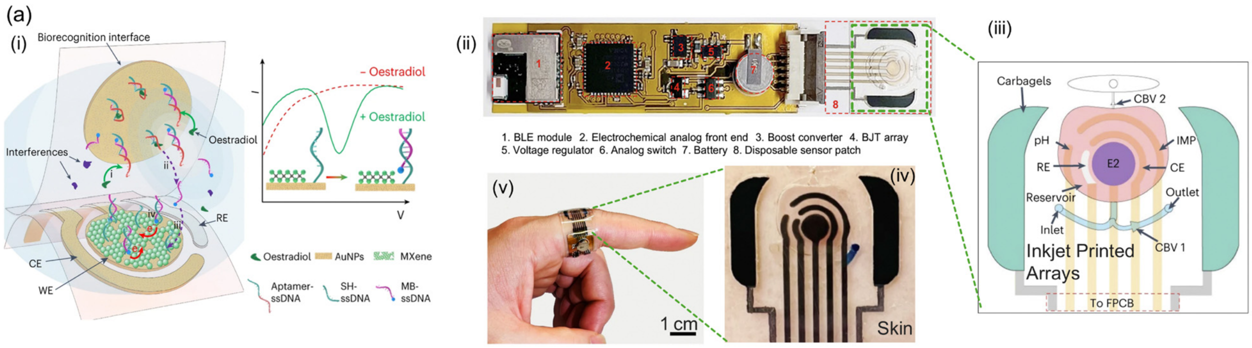

**Battery-free, NFC-enabled Smart Sensor for Wound Infection Detection**

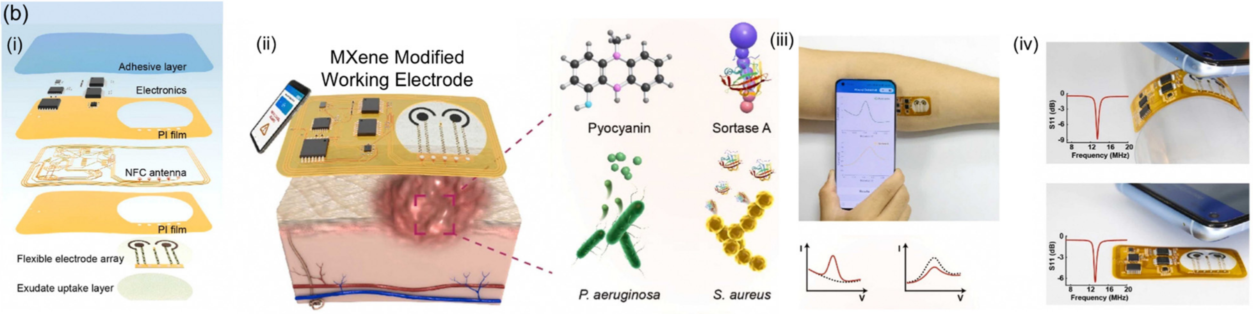

**All-MXene based electronic Textile (e-textile)**

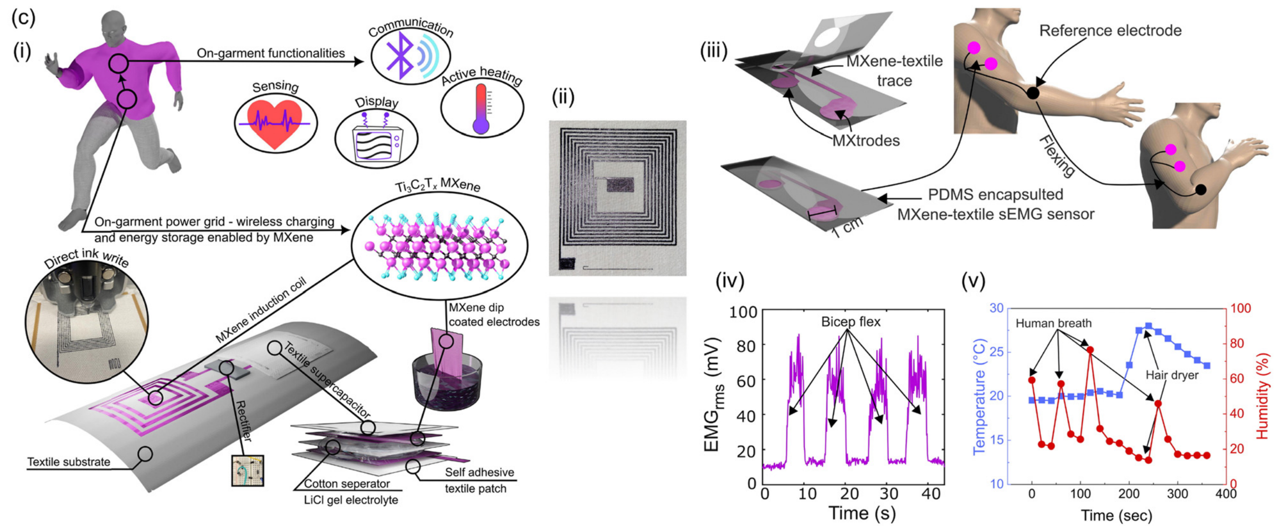

Fig. 12 (a-i) Reagentless *in situ* quantification of oestradiol using an AuNP-MXene sensor coupled with a target-induced strand-displacement aptamer switch. (a-ii) Photographs of the electronic system of the wearable sensor. (a-iii) Schematic illustration of the multiplexed microfluidic sensor patch. (a-iv) Sensing part of the disposable sensor patch. (a-v) Fully integrated wireless wearable patch on a finger. Reproduced with Permission from ref. 200 © 2024, Springer Nature Limited. (b-i) Layer-by-layer view of smart patch fabrication. (b-ii) Schematic of the smart bandage for *in situ* detection of wound infection *via* bacterial virulence factors. (b-iii) Image of a smartphone and smart bandage pasted on the arm to transfer data wirelessly. (b-iv) Near-field communication (NFC)-enabled wireless communication with various configurations of mobile terminals. Reproduced with Permission from ref. 201 © 2023 Elsevier B.V. (c-i) Printing and integration of all-MXene wireless charging system and supercapacitor for textile electronics (e-textiles) alongwith possible applications. (c-ii) Digital photograph of a 5 × 5 $cm^2$ MX-antenna. (c-iii) MXene textile electrode and a wireless EMG sensor on the bicep for sEMG monitoring. (c-iv) Real-time monitoring of sEMG signals, (c-v) temperature and humidity measurements with a built-in sensor powered by the MX-antenna. Reproduced with Permission from ref. 202 © 2024 Elsevier B.V.

networks, potentially revolutionizing approaches for monitoring, therapy, and diagnostics. Current bioelectronic materials face challenges in terms of cost and mechanical, chemical, and electrical compatibility with biological tissues. Another crucial aspect for both safe electrical stimulation and optimal recording is achieving minimal impedance at the electrode–tissue interface. As a result, traditional Ag/AgCl electrodes often utilize conductive gels at the skin interface in applications such as skin electronics to decrease impedance and enhance signal quality. Moreover, existing manufacturing techniques are expensive, not scalable, and have a limited resolution. Although solution-based fabrication methods such as inkjet or screen printing are more scalable than wafer-scale approaches and economical alternatives for producing multi-electrode arrays, there is a lack of biocompatible conductive inks available for these processes. $Ti_3C_2T_x$, among the numerous MXenes synthesized so far, has been successfully optimized and investigated for high-resolution biological interfaces, such as neuroelectronic devices,[211,212] skin comfortable sensors,[213] wearables for neuromuscular diagnosis,[214] fiber microelectrodes for biointerfacing,[215] and transparent microelectrodes for neural mapping.[216] Flavia *et al.* extensively explored $Ti_3C_2T_x$ microelectrode implants (dry MXene electrode arrays) and flexible sensors compatible with skin.[38,217] The fabrication of flexible, multichannel, high-density bioelectronic interfaces, known as "MXtrodes"[38] demonstrates the potential for superior recording and externally controllable stimulation of neuromuscular circuits by varying the input pulses. MXtrodes without a gel, designed with specific geometries for specific uses, have been employed in human epidermal sensing (Fig. 13a). The performance of the 3D MXtrode system was evaluated by recording scalp EEG signals from a healthy object (Fig. 13b) and further compared with a traditional gel-based Ag/AgCl system. Notably, low-impedance gel-free MXtrodes on the millimeter scale allow high-resolution EEG. This feature is crucial because the impedance at the electrode–skin interface plays a key role in determining the quality of the scalp EEG data. This verifies that gel-free MXtrodes, at the millimeter scale, provide improved performance in EEG applications.

Furthermore, implantable MXtrodes have also been explored for stimulation purposes, leading to their application in intraoperative electrocorticography (ECoG), a typical neurosurgical practice for tumor removal and epilepsy treatment (or other neuromodulation therapies).[38] Studies on intraoperative brain stimulation in rats have demonstrated that MXtrodes possess superior charge storage and injection capabilities compared with platinum (Pt), a material frequently employed in stimulation electrodes (Fig. 13c). This finding underscores the potential effectiveness of MXtrodes in electrical stimulation applications. It has also been shown that whisker movements can be induced by stimulation currents exceeding 1.0 mA, with the response varying based on stimulus intensity, indicating that MXtrodes can effectively modulate brain activity *via* electrical stimulation (Fig. 13d). However, additional *in vivo* testing and histological analysis are necessary to optimize the threshold voltage for MXtrodes to ensure safe stimulation. This is essential because several factors, such as the pulse frequency, duty cycle, current density, and electrode size, affect the stimulation input, which in turn determines the intensity of tissue damage. As bioelectronic technologies continue to advance, their integration into clinical imaging techniques is becoming increasingly important. The MXtrodes demonstrated excellent performance during scanning, showed no image distortion or interference, and remained undetectable (Fig. 13e).[38] This advancement has opened new opportunities for combining various modalities, such as integrating EEG with functional MRI or GluCEST, and has the potential to significantly enhance both clinical diagnostic capabilities and neuroscientific investigations.

**High interfacial impedance problem and symmetry breaking in MXenes:** MXenes, owing to their inherently low out-of-plane charge transport, face challenges with high interfacial impedance at the bioelectronic–organ interface. This hampers their application in soft bioelectronic implants, as low impedance can adversely affect electrophysiological signal fidelity and implant performance. To address this, Wu *et al.*[218] introduced mild surface oxidation to form anatase $TiO_2$ on MXenes (OBXenes), which disrupts the in-plane orbital symmetry of the p–d hybridized orbitals of MXenes, resulting in reduced interfacial impedance. While the oxidation process diminishes the in-plane conductivity of MXenes, it enhances their out-of-plane charge transport properties.

The OBXene patch integrated multiple layers of OBXene-based components, including sensors, actuators, and loopback interconnects, as illustrated in the exploded view (Fig. 14a). This patch comprises a voltage sensor, temperature sensor, heater, an electrical stimulator, an electrocardiographic (ECG) and a pressure mapping array (Fig. 14a). Designed as a bioelectronic implant, the OBXene patch bridges foundational knowledge with practical implementation, enabling precise electro- and thermal therapies, while facilitating real-time on-site monitoring of the contractile physiology of cardiomyocytes. OBXene–MECG electrode provides continuous recording of electrical activity with exceptional accuracy. This provides distinct electrophysiological patterns associated with various areas of a living rat's heart, enabling the precise detection and identification of regions affected by ischemia, infarction, or specific arrhythmogenic foci.[218]

**Electrotherapy:** Accurate and focused electrical stimulation plays a critical role in managing myocardial infarction in individuals with intraventricular conduction delays or abnormalities in ventricular depolarization. With its enhanced charge injection capacity (CIC), OBXene delivers biologically relevant charge injections with minimal heat dissipation.[218] Fig. 14(b) and (c) illustrate the setup for cardiac electrotherapy with MECG and AECG electrodes synchronized with the concurrent ECG feedback. Consequently, OBXene electrodes provide better cardiac recording with precise charge transfer to stimulate the cardiac epicardium, enabling comprehensive ECG sensing and simultaneous electrical therapy.

**Thermotherapy:** In individuals with myocardial infarction, the temperature of the heart tissue in the affected region can

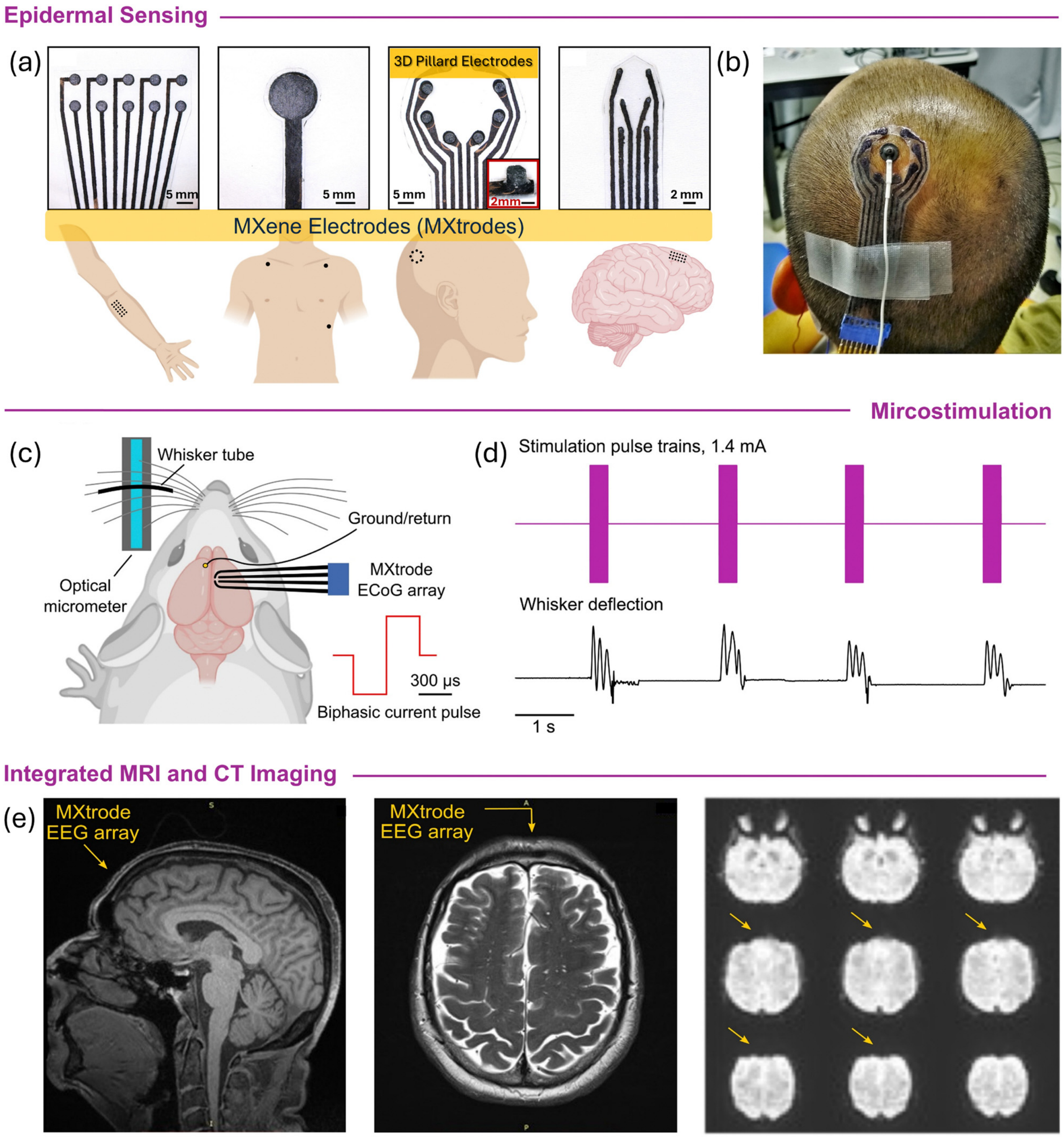

Fig. 13 (a) Digital photographs of different electrode arrays (MXene-infused electrode arrays, termed as MXtrodes) with possible anatomical sites for their application. (b) MXtrodes implanted on a healthy subject's scalp for EEG recording. (c) Schematic of the microstimulation setup (electrocorticography setup) with MXtrodes attached to the barrel cortex. (d) Whisker deflection against different stimulation input pulses. (e) MRI images in the presence of MXtrode array attached to the human forehead. Reproduced with Permission from ref. 38 © 2021 AAAS.

increase by 0.5 °C to 2 °C.[218,219] This increase results from cellular and physiological activities, including increased metabolic responses, driven by inflammation and tissue damage. As these temperature variations are localized and typically go undetected in standard body temperature assessments, specialized medical sensors are essential for accurate detection and treatment. The OBXene-based cardiac patch exhibited a strong linear correlation with the temperature (Fig. 14d). This feature facilitates temperature regulation, ranging from room temperature to clinically significant myocardial temperatures (Fig. 14d), demonstrating its potential for precise thermotherapy through targeted thermal necrosis and real-time monitoring. The OBXene-based strain sensor, depicted in Fig. 14d and e, demonstrates its flexible attachment and mechanical

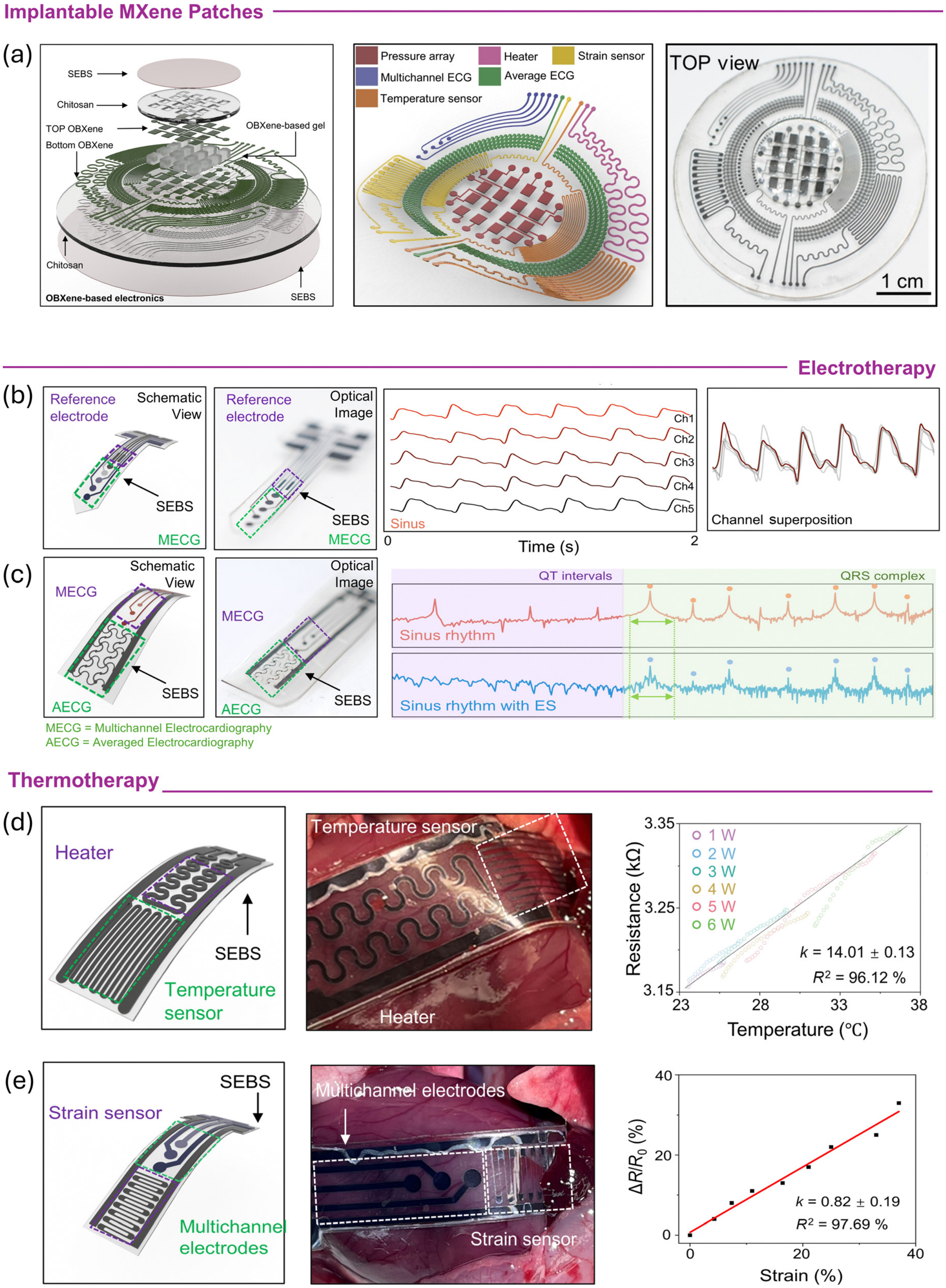

Fig. 14 (a) Exploded view (left), individual components (middle), and (right) digital image of an OBXene-based implantable patch. Schematic view and digital image of (b) OBXene-based MECG electrodes and (c) combined AECG MECG electrodes with corresponding ECG recordings of a live rat heart and simultaneous ECG detection under different electrical stimulations (*i.e.*, electrotherapy). Schematic view of a (d) heater integrated temperature sensor implanted over the rat epicardium showing the possibility of controllable heating (*i.e.*, thermotherapy). Schematic view of (e) OBXene multichannel electrodes and strain sensors implanted in the rat epicardium for simultaneous thermotherapy. Reproduced with Permission from ref. 218 © 2021 AAAS.

adaptability, enabling continuous monitoring of cardiac mechanics alongside electrotherapy. Electrical stimulation therapies stimulate the rhythm and physiological function of infarcted hearts, providing valuable insights into recovery after cardiac arrest and sudden loss of cardiac function. This biocompatible, flexible, and multifunctional implant shows exciting potential for clinical applications with wireless and battery-free management over extended periods and live cardiac monitoring. A few implantable sensing devices can simultaneously measure temperature, and ECG signals with a single electrode, while others can monitor these parameters separately. In addition, the cardiac patch based on OBXene did not contain metallic components. This platform is ideal for modern healthcare diagnostics because it prevents artifacts that interfere with diagnostic images such as those from CT or MRI. The substantial influence of OBXene, as shown by Wu *et al.*, may promote the adoption of low-dimensional materials in bioelectronic implants, potentially leading to advanced implantable electronics for organs, such as the brain, lungs, and kidneys.

### 4.9. Antiviral behavior and immune profiling

To date, the antibacterial properties of MXenes have been thoroughly investigated (detailed in ESI-II†). However, the antiviral activities of MXenes remained unexplored until Mehmet *et al.* demonstrated significant antiviral activities and immune responses in four known MXene phases (for example, $Mo_2Ti_2C_3T_x$, $Ti_3C_2T_x$, and $M_4C_3T_x$; M = Ta, Nb) against four distinct SARS-CoV-2 genotypes (known variants with wild-type or mutated spike proteins).[220] As anticipated, lower concentrations of $Ti_3C_2T_x$ and $Mo_2Ti_2C_3T_x$ exhibited better antiviral activity. $Ti_3C_2T_x$ inhibits viral activity on the cellular surface, thereby inhibiting the pathways responsible for modulating viral proteins, mutations, and/or replication. Among the four investigated viral clades (GR, GS, H, and others), $Ti_3C_2T_x$ demonstrated a significant reduction in infection in SARS-CoV-2/clade-GR infected Vero-E6 cells. This highlights the importance of viral protein changes in the inhibition and selective sensitivity of the GR clade towards MXenes. Interestingly, in contrast to the antimicrobial properties, the ineffectiveness of $TiO_2$ nanoparticles in preventing viral infection further supports the notion that the antiviral properties of MXenes are not attributable to transition metal oxides. Rather, the inhibition can be ascribed to potent interactions between the polar surfaces of MXenes and their redox-active nature. Remarkably, the antiviral efficacy of the two MXenes with identical structures but different surface environments indicates that surface chemistry plays a crucial role in this process. In addition, the biological and immunological compatibility of MXenes can be demonstrated using immune profiling. Immune responses and cytokine storms are considered to be crucial elements in COVID-19 progression. Single-cell mass cytometry, an advanced high-dimensional technique to examine the impact of MXenes on distinct immunological subsets, revealed that MXenes suppressed monocytes and counteracted the production of pro-inflammatory cytokines induced by COVID, signifying anti-inflammatory properties.[221] Given MXene's ability to inhibit viral replication and regulate the immune system, it presents a potential tool in combating viral infections.

Further investigation into the immunological characteristics of other MXenes, $Nb_4C_3T_x$, $Mo_2Ti_2C_3T_x$, and $Ta_4C_3T_x$, by Laura *et al.*[222] revealed the capacity of MXenes to interact with various immune cells *via* the LINKED method, a novel multiplexed label-free single-cell detection technique integrating single-cell mass cytometry *via* time-of-flight (CyTOF) and ion beam imaging *via* time-of-flight (MIBI-TOF). This technique facilitates identification through mass cytometry and imaging at the individual cell level, enabling concurrent measurement of multiple cellular and tissue properties without compromising cell viability. The potential immunomodulatory effects of $V_4C_3T_x$ MXenes on various immunological subpopulations were assessed using the CyTOF.[223] The molecular mechanism underlying $V_4C_3T_x$ immunomodulation indicates the absence of $V_4C_3T_x$ in any subcellular compartment, different from that of $Ti_3C_2T_x$, suggesting that the immunomodulatory effects of MXenes are unique to their elemental composition. The observed connections between internalization and material chemistry indicate that the chemical properties of MXenes may play a crucial role in their cellular uptake, which has important ramifications in the biomedical field.

The significance of immune responses to viral infections and their capability to detect them at the cellular level can enhance preclinical research on MXenes. It also anticipates the future development of MXene-based antiviral therapeutic nanoformulations. Together, these factors provide valuable insights into the development of multifunctional MXene-based nanosystems as immune modulators and antiviral agents.

**Supplementary information II (ESI†)**

- Biocompatibility, antimicrobial features and biodegradability
- Ecological impact of MXenes

Evaluating cytotoxicity is crucial for biocompatibility assessments. For a material to be considered biocompatible, it must exhibit non-cytotoxic characteristics. Regarding MXenes, their toxicity is complex and varies according to the synthesis approach, flake morphology, flake size, cell type, reactive oxygen species (ROS) production. The degradation behavior of different MXene configurations is also discussed, along with potential ecological impacts.

## 5. Theoretical studies and impact of artificial intelligence technologies

Theoretical approaches and artificial intelligence (AI) have transformed material science and research trends in MXenes. The first part of the following sections discusses the role computational science on MAX prediction, its exfoliation to MXenes alongwith additional mechanistic insights into the etching process. In the later sections, we highlight the role of AI-driven technologies and the integration of machine learning (ML) technologies in MXene research.

### 5.1. Theoretical insights into synthesis, stability and applications

Developing new MAX phases, controlling their structure, and predicting their exfoliability to form isolated sheets are topics of substantial interest in MXene research. Computational investigations have revealed the etching mechanisms of MXenes and the effects of several other parameters. The following sections examine different theoretical approaches for predicting MAX phases, their exfoliability, and atomistic perspective of the etching process. Furthermore, it presents a theoretical perspective on the role of surface terminations in determining MXene applications. A discussion on the influence of the etching route and/or etchant concentration on the electronic structure, physical properties, and aqueous stability of MXenes (commonly referred to as "water attack") is included in ESI-III† for a more comprehensive understanding of the topic.

**5.1.1. Predicting MAX exfoliability to MXenes.** Generally, MA bonds in MAX phases are weaker, whereas the bonds between MX layers are relatively stronger. Hence, the evaluation of the MA and MX bond strengths in MAX phases is the easiest way to determine their exfoliability. For that purpose, static calculations can provide insight into the binding characteristics of the MAX phase constituents. Khazaei *et al.* evaluated various M and A elements to predict novel MAX phases and offered insights into their potential exfoliation into MXene.[224] Force constant (FC) and exfoliation energy ($E_{\text{exf.}}$) were established to predict MAX exfoliability. As the bond strength is associated with FC values, higher FC values suggest stronger bonds or *vice versa*. Moreover, the $E_{\text{exf.}}$ of the MAX phases is correlated with the FC value of the A atoms ($FC_A$) and showed a linear dependence (Fig. 15a). This suggests that MAX phases with lower $FC_A$ have weaker A bonds and thus lower $E_{\text{exf.}}$ This further highlight how different MAX compositions require different etching conditions. Khaledialidusti *et al.* performed high-throughput DFT calculations on 1122 MAX candidates.[225] To computationally screen their conversion into MXenes, the FC between the M and A atoms ($FC_{MA}$) was compared with that of $FC_A$ (Fig. 15b). It was revealed that MAX phases with smaller $FC_A$ values have weaker MA bonds (*e.g.*, lower $FC_{MA}$ values) and consequently possess lower $E_{\text{exf.}}$ Therefore, it is easier to exfoliate these MAX phases. Furthermore, the correspondence between the FC values and bond lengths (Fig. 15c) indicates that the bonds between M and A are longer and therefore weaker, whereas the bond lengths between M and X are shorter (therefore stronger). This explain that only the A elements are selectively removed without disrupting MC lattice during experimental etching. This further suggests that carbide MAX phases are more easily synthesised than nitride phases which also satisfies experimental investigations.[119] In contrast, theoretical studies have also predicted the mechanical exfoliation of MAX phases. Under mechanical force, M–A bonds in $M_2AC$ were disrupted owing to high tensile stress, separating the $M_2C$ and Al-layers. Since some MAX phases exhibit stronger bonding in *ab*-plane than in the *c* direction. So, it is possible to selectively break M–A–M bonds without damaging M–X–M bonds under appropriate mechanical stress.[226] Gkountaras *et al.* effectively exfoliated a few layers of the MAX phase using an adhesive-tape approach. Because "A" was still present in the 2D flakes, the resulting crystals were named "MAXenes".[227] The possibility of forming MXenes through the mechanical exfoliation of MAX phases highlights the importance of such theoretical observations.

**5.1.2. Insights into etching propagation.** Complex experimental etching involves different factors and reaction kinetics, so a thorough model or large-scale simulation of synthesis process is difficult. Singh *et al.* delved into dynamic perception of wet-$Ti_3C_2T_x$ etching *via* MD simulations and provided an atomistic insight into the process (Fig. 15d i–viii).[228] MD simulations suggest that the terminal groups propagate the etching process. Initially, HF interacted with the outer atoms and terminated the uncoordinated edge Ti atoms with H/F groups (Fig. 15d-ii). These terminations pushed the Ti–Al atoms apart and weakened their bonds. As the HF concentration increased, both edge Ti atoms were terminated by more F atoms, which further increased the bond distance (Fig. 15d-iii) and reduced the Ti–Al bond strength. This widened the interlayer gaps and exposed the inner layers (Fig. 15d iii–vii). Following these step-by-step interactions ultimately led to the removal of the A atom and the formation of $AlF_3$ and $H_2$ (Fig. 15d vii–viii). This progressive etching mechanism and the evolution of $AlF_3$ and $H_2$ (both as by-products) are well known in the experimental etching. The electron localisation function (ELF) can provide further insight into bond formation between Ti/Al and H/F molecules in MAX and HF-etched MAX (Fig. 15e i–viii). ELF is particularly useful for analysing chemical bonding within molecules. It can differentiate between covalent, metallic, and ionic bonds by showing how electrons are distributed in space. In $Ti_3C_2T_x$, Ti–C exhibits high ELF values ($\sim$0.8–0.9), indicating strong covalent bonds, whereas moderate values ($\sim$0.4–0.6) for Al–Ti suggest relatively weak bonding. This suggests the possibility of selectively removing Al without disturbing the Ti–C lattice. Furthermore, the electron density is localised around the Al atom located on the edge of Ti–Al and is ionic in nature (Fig. 15e-i). Such high charge density around the Ti–Al layers triggers HF dissociation and subsequent adsorption of $F_1$ and $F_2$ onto the $Ti_1$ and $Ti_2$ atoms on the edges, releasing H molecules (Fig. 15e ii–viii). High ELF values ($\sim$0.8–1.0) for H and F atoms indicate strong covalent–ionic bonds between H/F and Ti. This indicated the formation of fluorinated MXenes. Experimental studies on HF-etched MAX have demonstrated that higher HF concentrations result in excess F-terminations, or *vice versa*. $H_2$ molecules are formed owing to the strong localisation of an electron pair (Fig. 15e iii–viii). HF terminates the outer Ti atoms with H or F groups which forces the Ti–Al atoms apart and weakens their bonding. Therefore, this confirms that terminations facilitate further interaction of the etchant solution with the inner layers and removal of the interleaved A layers. Jonas *et al.* also pointed out that chemical exfoliation of MAX to MXene is thermodynamically possible, considering only the adsorption of terminal groups on the flake surface.[231]

**5.1.3. Sensing applications.** Noticeably, the performance of MXene-based devices is also affected by variations in their electronic structure. Fig. 7f highlights the bandgap fluctuations in pure and oxidised MXenes and their impact on gas-sensing

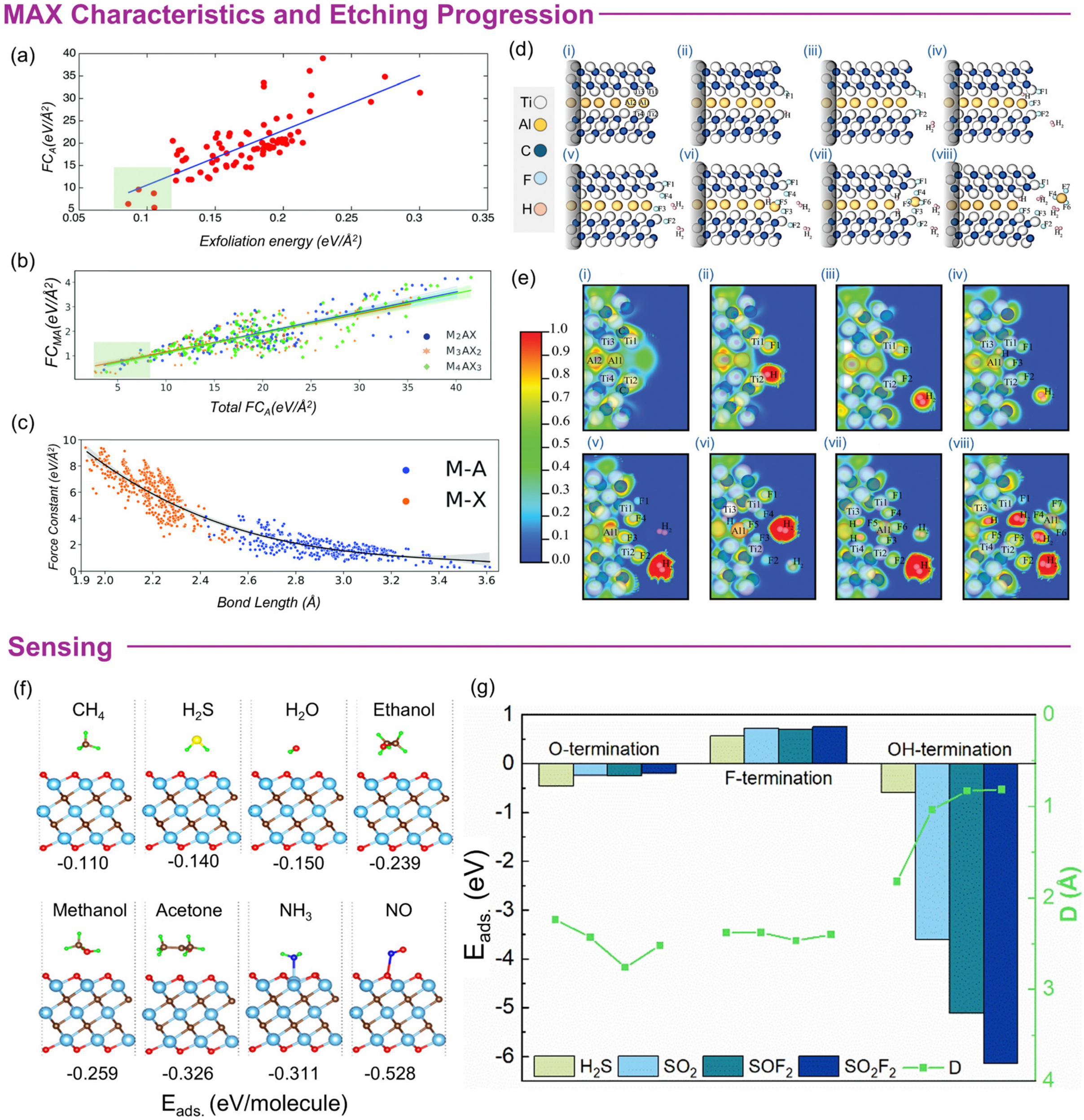

Fig. 15 (a) Correlation between the $FC_A$ of the MAX phase and exfoliation energy. Reproduced with Permission from ref. 224 Copyright © 2018 Royal Society of Chemistry. (b) Total force constant of M–A elements ($FC_{MA}$) *versus* A elements ($FC_A$) of the MAX Phase. Smaller $FC_{M-A}$ and $FC_A$ values indicate lower $E_{exf.}$ as highlighted by green boxes. (c) Variation in FC values between MA and MX bonds in MAX phases. Reproduced with Permission from ref. 225 Copyright © 2021 the Royal Society of Chemistry. (d) Atomic configuration representation and (e) ELF plots for step-by-step (i)–(viii) etching of $Ti_3Al_2$ to $Ti_3C_2T_x$ MXene realised through molecular dynamics simulations. Reproduced with Permission from ref. 228, Copyright © 2016 American Chemical Society. (f) Favourable adsorption sites of different gas molecules on MXene structures (corresponding adsorption energy values of each gas molecule are also shown). Reproduced with Permission from ref. 229, Copyright © 2019 American Chemical Society. (g) Variations in adsorption energy values and adsorption distances of different gas molecules with respect to different terminations on the MXene surface. Reproduced with Permission from ref. 230, copyright, © 2021 Elsevier B.V.

performance. First-principles calculations investigate the adsorption of various gas molecules onto the MXene surface. When gas molecules come in contact with the $Ti_3C_2O_2$ surface, they get adsorbed.[229] Therefore, it is very important to study the electronic properties and geometrical optimisation of such adsorption systems. Fig. 15f shows the most stable positions for different adsorbed gas molecules. It should be noted that all the adsorbed gases maintained their molecular structures, and no decomposition was observed. Based on the adsorption energies ($E_{ads.}$), $NH_3$, ethanol, methanol, and acetone molecules interact more strongly with the $Ti_3C_2O_2$ substrate than with $CH_4$, $H_2S$, and $H_2O$. Additionally, using $Ti_3C_2T_x$, Zeng *et al.* studied adsorption energies and corresponding adsorption distances for four different types of gas molecules: $H_2S$, $SO_2$,

$SOF_2$, and $SO_2F_2$. It is clear how the surface groups affect the adsorption energy and distance (Fig. 15g). However, target gases spontaneously adsorb onto $Ti_3C_2O_2$ and $Ti_3C_2(OH)_2$, but $Ti_3C_2F_2$ requires extra energy (positive $E_{ads.}$). In addition, the charge transfer induced by gas adsorption decreased continuously in the following order: $Ti_3C_2(OH)_2$, $Ti_3C_2O_2$, and $Ti_3C_2F_2$. This implies that OH-terminated $Ti_3C_2$ exhibits superior performance compared to =O and –F-terminated ones. Specifically, for $H_2S$ sensing, –OH-MXenes is preferable whereas oxidized-MXenes exhibit a superior performance for other gas molecules. Just a note to recall the amounts of =O, –F, and –OH vary depending on the MXene synthesis route (*e.g.*, pure HF, HCl + HF, HCl + LiF, or the molten salt method). Consequently, it is possible to control the type and number of terminal groups by following a suitable synthesis route, therefore achieving a selective gas-sensing.

**Supplementary information III (ESI†)**

- Predicting the physical properties
- Aqueous stability (the so-called water attack)
- Surface terminations and stability

This section of the supplementary information provides detailed theoretical insights into the physical properties of MXenes, particularly their electronic characteristics. It also discusses their aqueous stability (commonly referred to as 'water attack') and the influence of termination concentration.

### 5.2. Machine learning in MXene synthesis and applications

Machine learning is a process in which behaviour is modified based on prior experiences, which serve as the training data. ML is a subclass of artificial intelligence (AI) that allows data learning and decision-making without explicit programming. ML aids in predicting various features, optimising structures, and designing experiments across extensive parameter spaces. Similarly, ML algorithms have been proven to be helpful in predicting the exfoliability of MXenes and minimising the time and resources required for their experimental synthesis. As discussed in the previous section, many MXenes have been predicted theoretically, but few have been synthesised and optimised for scalable production. Consequently, ML algorithms have identified synthesizable phases from a large pool of 2D MXenes, offering a cost-effective method to minimise trial-and-error during synthesis.[232] The use of ML is also necessary because of imbalanced nature of MXene synthesis data and can be divided into positively labelled data (synthesised MXenes) and several unlabelled examples (MXenes to be evaluated for exfoliability). Therefore, using a positive and label-unlabelled (PU) ML framework is an optimal method to predict MXenes' synthesisability. This technique relies on positive evidence, classifying experimentally synthesised MXenes as labelled and those not synthesised yet as unlabelled. Frey *et al.* considered MAX in the search field because MXenes are typically produced from MAX through liquid exfoliation (provided that the MAX phase is also synthesizable at the first place).[233] Therefore, this study separately estimated the synthesizability of MAX and its corresponding MXene within the search space and focused on single-M MXenes. Qualitatively, the initial material search space was defined using 11 transition metals, 12 "A" elements, 2 X-elements (carbon "C" and nitrogen "N"), while $n$ = 1, 2, or 3. Thus, 792 MAX and 66 MXene samples were evaluated (12 MAX phases per MXene, with varying A). Furthermore, the ML algorithm was trained by including input features such as structural, thermodynamic, electronic, and fundamental data collected from material databases and DFT simulations. Several other predictive features were added to the ML algorithm to obtain most important features (each feature received a ranking from machine learning). In response, five key factors, namely, bond distance, binding energy, Bader charge per atom, formation energy, and mass per atom, were identified as essential chemical data to access MXene synthesizability. Furthermore, to predict the synthesizability, 10 synthesised MXenes, including $Hf_3C_2$, $Mo_2C$, and $Ti_2C$ (labelled as true positives), and 56 unlabelled MXenes were entered into the PU learning algorithm using the bootstrap method. Note that bootstrapping usually reiterates the data multiple times to address any shortcomings in the original data. Such a technique generates "$k$" numbers of improved datasets and reduces overfitting caused by the limited initial data—thereby making the ML system more stable. Frey *et al.* distributed bootstrap data into a 90% training set and a 10% testing set before applying the PU method, as shown in the blue boxes (Fig. 16a).[233] The PU algorithm initially selects unlabelled data randomly and describes them as "negative" (green boxes, classified as non-synthesizable). Subsequently, a classification algorithm determines a hyperplane that classifies the dataset as either "positive" (red circles, designated as synthesizable) or "negative" (Fig. 16a, bottom left). This process was repeated $k$ times for each bootstrapped dataset. Consequently, a decision tree and a "synthesizability score" were used to rank MXenes based on their synthesizability (Fig. 16a, bottom right, word cloud). As indicated by the clear pattern, Ti-, Zr-, and Hf-based MAX phases (with carbide as the X element) have strong synthesizability, whereas W-based systems have very low synthesis probability (Fig. 16b). However, there was a less obvious dependence on the A atom. This is intriguing because, although only Al-based MAX phases have been effectively etched into MXenes, a significant number of MAX compounds with different A elements have been identified as potential MXene precursors. Importantly, the synthesizability of MXenes is not always guaranteed by the expected synthesizability of MAX. In other words, it is not possible to experimentally convert all MAX phases to MXenes, as they require high exfoliation energies. Therefore, exfoliability must be simultaneously evaluated. Another important aspect is the possibility of a mechanical exfoliation. Therefore, a third criterion was manually introduced into the algorithm.[233] A combination of these criteria yielded 20 MAX/MXene combinations with the highest synthesizability, with $Zr_2C$ identified as the most probable MXene to be synthesised from $Zr_2GaC$. As highlighted in the previous section, the mechanical exfoliation energy is an unreliable predictor of exfoliation, rendering the results questionable. Instead of relying on the ML system to rank the importance of mechanical exfoliation energy in

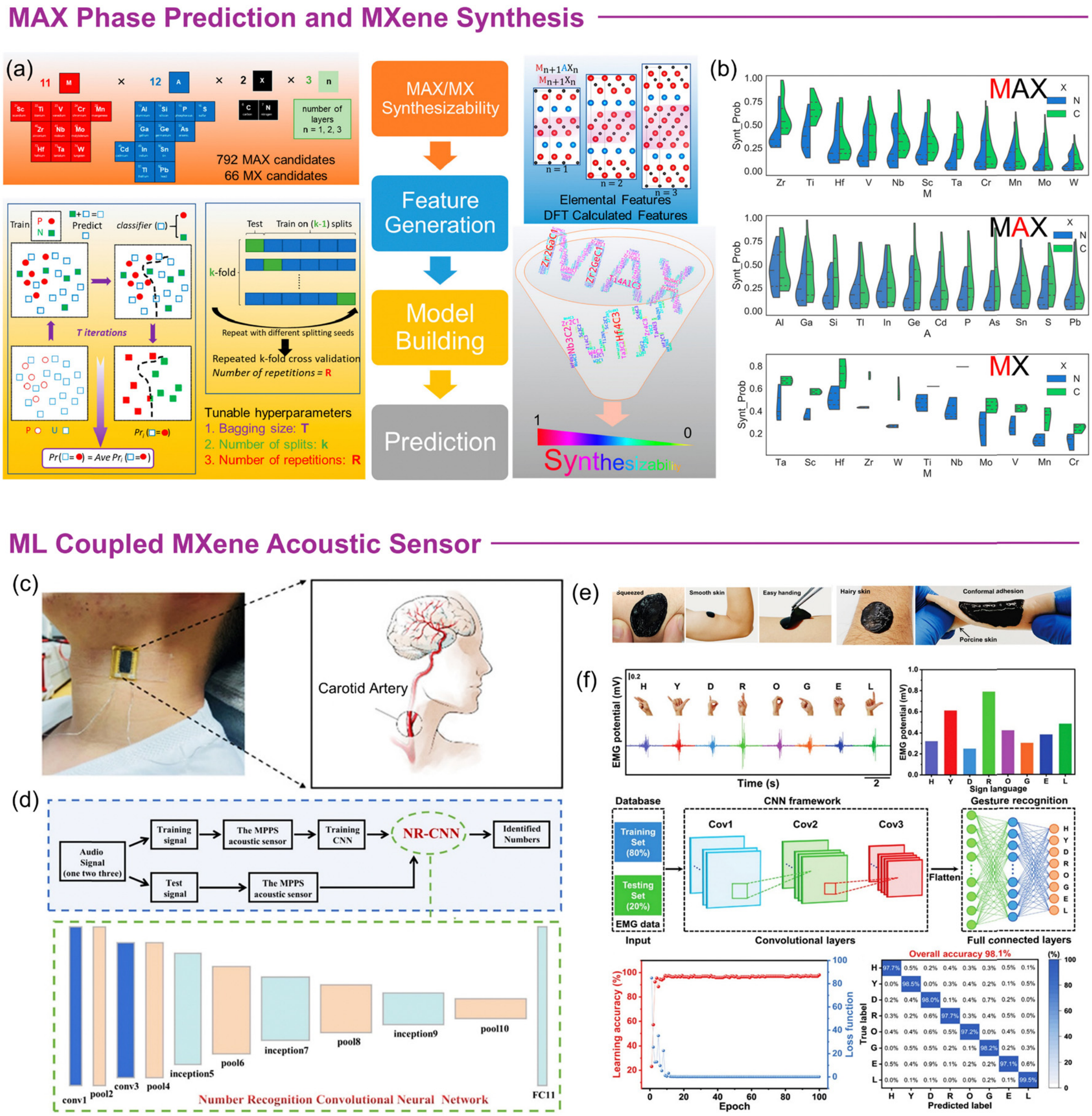

Fig. 16 (a) Schematic depiction of a computational phenomenon integrating positive and label-unlabelled (PU) learning and chemical search space. Top left: with $n$ = 1, 2, or 3, the MAX/MXene search space includes all possible combinations of M, A, and X. Top right: structural view of the MAX phase along with the corresponding MXenes. Bottom left: PU learning process for all model parameters. Bottom right: word clouds where uppercase letters and red colors indicate the high synthesizability of MXene compounds. (b) Synthesis possibilities for MXenes with respect to various M and A elements, represented by violin plots. Reproduced with Permission from ref. 233 Copyright © 2019, American Chemical Society. (c) Image of an MPAS patch pasted on the lateral side of the human neck, with the corresponding position of the carotid artery. (d) Experimental flowchart featuring an NR-CNN-based deep-learning mechanism for MPAS applications. Reproduced with Permission from ref. 235 Copyright © 2022 Wiley-VCH. (e) Hydrogel-based epidermal sensor with conductive MXene nanosheets adhering securely and stably to human skin. (f) Convolutional neural network (CNN) machine learning method for classifying and recognising EMG signals generated by various sign language gestures with corresponding testing/training sets and accuracy analysis. Reproduced with Permission from ref. 236 Copyright © 2024 Wiley-VCH GmbH.

predicting synthesizability, one may also challenge human involvement by manually adding it as a criterion. However, given the recent advances in the theoretical understanding of MXene synthesis and the impact of ML, it will be interesting to see how other properties, such as vacancies, formation energies, and chemical exfoliation energies, are determined. For instance, researchers have determined the stability of MXenes using precise stability descriptors by integrating first-principles computational modelling and ML algorithms and predicted the stability of 32 MXenes.[234] Similarly, the integration of first-principles computational modelling and machine learning algorithms has facilitated the precise determination of band gaps of MXenes, as detailed in ESI-IV.†

AI-based research and ML approaches (particularly deep learning models) have made significant progress in MXene-based electronic skin and other biomedical devices. For example, wearable sensors integrated with a convolutional neural network (CNN) provide a precise method for whole-body motion tracking and avatar reconstruction by effectively capturing physiological signals.[237] In addition, Ren *et al.* designed a MXene-based piezoresistive pressure sensor that mimics artificial eardrums and paired it with a *k*-means clustering algorithm-based speech recognition method for voice detection and recognition.[238] Compared to commercial recording devices, the MXene artificial eardrum exhibited exceptional mechanical sensitivity (62 $\text{kPa}^{-1}$) and a LOD of 0.1 Pa with good clustering, low complexity (able to distinguish 280 audio signals), and an accuracy rate of 96.4%.

Individuals with laryngeal diseases often struggle with proper pronunciation, which can hinder their communication. As the vocal cords are unique anatomical features that enable humans to communicate by producing sound, wearable artificial throat devices capable of recording physiological signals from the carotid artery wave can improve patient awareness and facilitate communication. The MXene/PEDOT:PSS acoustic sensor (MPAS) designed by Ding *et al.* effectively recognises different speeches.[235] The MPAS picks up a consistent and periodic pulse signal from the carotid artery (Fig. 16c). Furthermore, the anticipated deep learning model utilises a number recognition convolutional neural network (NR-CNN). Such an approach proved to be effective in achieving high-accuracy speech recognition (91%) across various pronunciations (Fig. 16d). It demonstrates the potential of MXene-incorporated wearable and smart artificial acoustics for speech recognition. Recently, Wang *et al.* developed a hydrogel-based epidermal sensor with conductive MXene nanosheets for electrophysiological signal monitoring (Fig. 16e).[236]

Further investigations on electromyography (EMG) signals of eight distinct hand movements (in sign language) led to varying amplitudes which were further classified and recognised by the convolutional neural network (CNN) machine learning method. A dataset of 1600 EMG data points was created after measuring each sign-language gesture 200 times. This dataset was split into two overlapping groups, 80% for training and 20% for testing. The proposed ML model exhibited significant classification, accuracy and stability after 100 training epochs, as evaluated by the learning accuracy and loss function (Fig. 16f). The recognition model revealed a high recognition accuracy of 98.1%, thus enabling the translation and detection of sign language movements based on EMG data.

Approaches that combine wearable and flexible sensors with edge-computing chips are versatile and can contribute significantly to current advances in the field *e.g.*, to develop humanoid robots. To accomplish this, various sensors and motors can be combined to create robots capable of performing tasks, such as therapy, surgery, and nursing. Moreover, soft robots equipped with 2D material actuators have shown great potential for limb prosthetics.[239,240] ML can also be used to analyze vast amounts of data available in databases and publications. However, the efficient transfer of large volumes of sensor data, energy-efficient local processing, and in-sensor machine learning are current challenges. Comparing data with varying degrees of theoretical or numerical precision is also challenging. ML can also potentially address one of the main challenges in the MXene field, that is, the toxicity mechanism, as outlined in ESI-IV.† Nonetheless, comparing the data from various studies remains a significant challenge for AI and ML. However, this issue is not unique to MXenes; rather, it is a broader challenge that computational materials science must address sooner rather than later. Standardizing protocols and developing material characterization models can benefit the AI community. Addressing these issues will require interdisciplinary research to advance hardware and software development. Furthermore, the integration of materials research, computational materials science, and emerging 5G technologies can enable the development of intelligent and automated medical devices (ESI-IV†).

**Supplementary information IV (ESI†)**

- Integration of DFT and statistical learning models
- Cytotoxicity analysis of MXenes through ML
- Integration of MXenes with internet of things (IoT) and 5G technology

Because the band gap of MXene varies with the surface terminal groups, accurate experimental determination becomes challenging. Although advanced computational techniques, such as density functional theory (DFT), can efficiently evaluate bandgaps, the values derived from the generalized gradient approximation (GGA), or local density approximation (LDA) are typically underestimated. Therefore, precise determination of the bandgaps of MXenes is a resource-intensive and time-consuming process. Herein, we delved into methodologies to better interpret MXene bandgaps. On the other hand, the integration of 5G-enabled IoT devices in healthcare enables real-time remote monitoring and personalized treatment, with 2D materials such as MXenes offering high conductivity and advanced sensor capabilities, which in turn play a crucial role in advancing smart medical devices and telemedicine solutions. We have detailed the integration of 2D materials into IoT technology in the ESI.†

## 6. Summary and outlook

In this review, we present a laboratory perspective of MXene synthesis, mainly highlighting the HF etching approach, the subsequent intercalation–delamination step, and the relevant experimental variables affecting the final quality of individual MXene flakes. Our goal was to standardize the synthesis protocols using laboratory modules and explain the science behind the experimental synthesis. This synthesis-related technique bridges the knowledge gap between laboratory aspects, experimental observations, and fundamental understanding, through a combination of scientific explanations and atomistic mechanisms. Through a rigorous review, we delve into healthcare-related applications of MXenes, investigate their underlying principles, and explicitly discuss the role of computational analysis, AI technologies, and IoT integration. This review aims to provide future researchers with relevant perspectives on MXenes and recommendations to maximize their potential in health technologies. Despite the development of MXene synthesis and enormous progress in healthcare applications, MXenes still have several limitations.

**Comparison with other 2D materials:** Graphene and other nanomaterials (*e.g.*, CNTs, gold nanoparticles, and magnetic nanoparticles) have reached commercial viability, particularly in electronics, biosensors, and medical imaging. Graphene, in particular, has dominated the scientific literature because of its well-established processing techniques and scalability. However, graphene and other materials (*e.g.*, TMD, h-BN, and the Xenes family) have several limitations. For example, cytotoxicity, hydrophobicity, limited structural, chemical, and elemental diversity of graphene, poor solubility and aggregation of TMDCs in physiological media, and h-BN, although biocompatible, lacks surface functional groups. In addition, the Xenes family, which is relatively thinner than MXenes, has been predicted to be a promising material in straintronics. Theoretical studies on silicene have demonstrated its exceptional strain resistance in both single[15] and bulk configurations,[241] making it a potential candidate for interconnects in flexible electronics. Despite its great potential, silicene is highly unstable under ambient conditions.[242] So, its integration into flexible and scalable devices faces technical challenges and requires the use of heterostructures.[243,244] In addition, Xenes are at early stages in other biomedical applications and demonstrate limited optical and electronic tunability, scarce reproducibility, and uncontrolled physicochemical nature.[245] The lack of such properties collectively leads to poor bioconjugation and functionalization, making them less attractive for biosensing and drug delivery applications. To overcome these issues, complex functionalization approaches have been employed.[246,247]

In contrast, MXenes possess features that other 2D materials lack, such as exceptional conductivity, hydrophilicity, versatile surface terminations (–OH, =O, and –F), reproducible synthesis, controlled physicochemical properties, mechanical robustness, and tunable flake size. MXenes are favorable choices for biosensors, implantable devices, and long-term therapeutic interventions. Hence, the future development of MXenes for healthcare applications is poised to benefit from their ability to overcome the limitations of other 2D materials. Although scientific and commercial interests are growing exponentially, MXenes are not currently on the same commercial scale as graphene.

**Understanding MXenes' synthesis:** The current understanding of MXene synthesis should be further expanded by exploring more accurate theoretical and experimental models. Researchers have simulated the experimental conditions of traditional HF etching using *ab initio* modelling, with studies primarily focusing on $Ti_3C_2T_x$ MXene. It may be more meaningful to understand the etching kinetics of other MAX phases (using different etching routes) and their conversion to multilayer and monolayer MXenes. It remains unclear whether the atomistic mechanism governing HF etching applies to other routes (*e.g.*, molten salt etching) or if a different approach is required. Another fundamental question that should be addressed in future research is the origin of the different terminations and the underlying thermodynamic principles. Separation of multilayer MXenes into single-layer 2D MXenes. What phenomena govern the delamination of MXene into single layers? This requires mechanistic insights similar to those obtained from $Ti_3C_2T_x$ chemical exfoliation.[228]

Taking about delamination, it's true that it is not always required for all applications, yet the limited possibilities for delamination may reduce the overall applicability of this material, especially in the case of electrochemical etching method (one of the greener production method of MXenes). Understanding the etching kinetics across diverse routes not only sheds light on the synthesis but also directly influences the delamination process. In this respect, it is important to understand the exact reasons that determine the choice of intercalant and how it can be tuned to a universal intercalant for MXenes. Can delamination be controlled by the interactions between the multilayers (originating from transition metal atoms), the type of surface termination, or is this choice solely determined by the etching procedure? Our analysis suggests that the etching route regulates the interlayer spacing and controls the choice of guest intercalant (*e.g.*, $Li^+$ intercalates in HF + HCl-etched $Ti_3C_2T_x$ owing to smaller gaps, whereas $TMA^+$/$TBA^+$ only intercalates in HF-etched MXenes). To a certain extent, the surface environment determines this choice. Nonetheless, there is limited literature explaining the underlying science of delamination; this highlights an area which requires further exploration. Systematic theoretical investigations can provide valuable information regarding reactions occurring on small scales over short time intervals. To date, we know about the $Ti_3C_2T_x$ phase, even though this knowledge can be generalized to other MXene systems. However, because of the complex surface chemistry of MXenes, their fundamentals should be investigated independently.

**A close look into existing limitations of MXenes:** As concerns over the environmental impact of MXene production and degradation grow, moving toward greener and less toxic materials is not only an ecological imperative but also aligns with increasing regulatory standards in healthcare materials. Harsh synthesis methods, oxidation, and large-scale production challenges have hindered the progress of MXenes compared to graphene. The involvement of toxic HF is detrimental and impedes the true potential of MXenes in biological applications. Because the abundance of –F terminations hinders bioconjugation, MXenes require additional modifications to make them suitable for biological use. Although a method with relatively less HF, such as MILD, is a promising alternative, it is important to consider the biological potential of fluorine-free techniques, an area that currently lacks sufficient research. Electrochemical etching and molten salt methods offer promising green alternatives; however, it is equally important to consider the biocompatibility of MXenes produced using these methods. These approaches significantly decrease the production of hazardous waste compared to HF-based methods but require innovations in cost reduction and scalability (also the delamination yield). The MXene community should also emphasize a comprehensive life-cycle analysis framework to thoroughly evaluate greener techniques. On the other hand, most non-Ti MXenes are produced *via* HF-based routes and further delaminated using organic spacers. Therefore, the development of delamination procedures without using organic spacers is important for biocompatibility as well as for increasing MXene conductivity and mechanical robustness. Similarly, controlling the dimensions of MXene sheets at the nanoscale is crucial for their use in biological applications.

Conventional production methods typically yield larger flakes with lateral sizes in the micrometre range. These larger dimensions can raise biosafety concerns, as they may accumulate at cellular sites and exhibit poor clearance from the body after therapeutic use. However, smaller flakes have the drawback of reduced conductivity, which may limit applications that rely on the conductive properties of MXene. Most studies investigated the synthesis and healthcare applications of single-metal MXenes. For example, $Ti_3C_2T_x$ MXene has received substantial attention owing to its well-documented potential. In particular, it accounts for approximately 70–80% of MXene-related publications. Other MXene compositions, such as $Nb_2CT_x$, $Ta_4C_3T_x$, and tungsten-based counterparts, have demonstrated exceptional potential for photothermal therapy and imaging. MXene research should progress both experimentally and computationally to include other counterparts as diverse compositions could open new frontiers. In this context, multi-transition metal chemistry (solid solutions and high-entropy MXenes) is promising and offers synergies for sensing and other healthcare applications.

Despite many efforts, MXenes have a short shelf-life (ESI-I†). Solution-processed delaminated MXenes (d-MXenes) undergo restacking and degradation (oxidation) over time in the presence of oxygen or water. There are potential ways to reduce the rate of oxidation; however, complete inhibition of MXene oxidation remains a significant challenge for the MXene community. The shelf life of MXenes in air and water can be extended to decades if stored as dried films (ESI-I†). Obtaining a such films into stable colloids after years of storage would be intriguing to observe. Stability issues are compounded when MXenes interact with biological systems. The long-term use of MXenes *in vivo* introduces additional challenges, such as biofouling, and demands further exploration of strategies to prevent biofouling. Furthermore, MXene agglomeration and/or precipitation in physiological environments is a challenge.[39] To mitigate biofouling or aggregation, surface modifications, such as PEGylation and peptide grafting, have been explored. Nonetheless, degradation of modified MXenes over time must be understood to ensure their long-term utility in healthcare applications. Although surface modifications improve biocompatibility, they also complicate the understanding of toxicity mechanisms, an area requiring further investigation. A global declaration of MXene biocompatibility is challenging because the synthesis process, surface groups, and flake size/shape determine the overall toxicity. In addition, despite having formal similarities, each MXene phase exhibits different properties. Therefore, exhaustive research is required to create a knowledge graph to accurately estimate cytotoxicity. In this context, ML-trained models combined with theoretical investigations can play a decisive role.

Given the complexity of toxicity and the need to fully understand the implications of MXenes, it is crucial to move beyond *in vitro* assays to more comprehensive *in vivo* investigations. Currently, MXenes lack sufficient *in vivo* validation, and further studies will help to uncover the true impact of MXenes in biological systems. Robust *in vivo* data across a wide range of MXenes are essential to meet regulatory standards. It has been shown that MXenes administrated either orally or intravenously, tend to accumulate primarily in the body organs. In addition, the half-lives of different modified MXenes vary significantly, resulting in varying degrees of degradation in biological media. This creates regulatory barriers that hinder the development of comprehensive standards to use MXene-based nanomaterials in medical applications. This suggests that research on MXenes in healthcare is still in its infancy and strict guidelines are required to guarantee their safe utilization in biological applications. Despite the promising potential of MXenes in healthcare, regulatory hurdles also continue to slow their commercialization. As these regulatory hurdles are addressed, MXenes can transition from laboratory research to scalable real-world applications. Researchers have developed a roadmap for MXenes, highlighting the most important research challenges for the next decade, including those related to synthesis, the fundamental structure–property relationship, stability, and the standardization of protocols.[248] Currently, the healthcare domain of MXenes is significantly behind that of energy storage and EMI shielding, which are the most likely candidates for early commercialization. Therefore, researchers should prioritize similar efforts in this domain as it can play a pivotal role in determining the commercial viability and broader impact of MXenes.

## Data availability

No primary research results, software or code have been included and no new data were generated or analysed as part of this review.

## Conflicts of interest

The authors declare no conflicts of interest.

## Acknowledgements

Zaheer Ud din Babar acknowledges Scuola Superiore Meridional (SSM), University of Naples, Federico-II, Naples, Italy, for funding his stay as a visiting PhD scholar at the Catala Institute of Nanoscience and Nanotechnology (ICN2), Campus UAB, 08193 Bellaterra, Barcelona, Spain. The authors are thankful to all individuals and/or organizations who provided permission to republish/reproduced their figures and other relevant information. This project has received funding from the European Union's Horizon Europe – the Framework Programme for Research and Innovation (2021–2027) under grant agreement No 101120706. The views and opinions expressed are however those of the author(s) only and do not necessarily reflect those of the European Union. Neither the European Union nor the granting authority can be held responsible for them. The ICN2 is funded by the CERCA programme/Generalitat de Catalunya. The ICN2 is supported by the Severo Ochoa Centres of Excellence programme, Grant CEX2021-001214-S, funded by MCIU/AEI/10.13039.501100011033. We acknowledge

Departament de Recerca i Universitats of Generalitat de Catalunya for the grant 2021 SGR 01464. We also acknowledge grant PID2021-124795NB-I00 funded by MICIU/AEI/10.13039/501100011033 and by "ERDF/EU"

## References

1 A. Bolotsky, D. Butler, C. Dong, K. Gerace, N. R. Glavin, C. Muratore, J. A. Robinson and A. Ebrahimi, Two-Dimensional Materials in Biosensing and Healthcare: From In Vitro Diagnostics to Optogenetics and Beyond, *ACS Nano*, 2019, **13**(9), 9781.

2 N. Rohaizad, C. C. Mayorga-Martinez, M. Fojtů, N. M. Latiff and M. Pumera, Two-dimensional materials in biomedical, biosensing and sensing applications, *Chem. Soc. Rev.*, 2021, **50**(1), 619.

3 Z. Zhu, An Overview of Carbon Nanotubes and Graphene for Biosensing Applications, *Nano-Micro Lett.*, 2017, **9**(3), 25.

4 R. Geetha Bai, N. Ninan, K. Muthoosamy and S. Manickam, Graphene: A versatile platform for nanotheranostics and tissue engineering, *Prog. Mater. Sci.*, 2018, **91**, 24.

5 P. Choudhary, T. Parandhaman, B. Ramalingam, N. Duraipandy, M. S. Kiran and S. K. Das, Fabrication of Nontoxic Reduced Graphene Oxide Protein Nanoframework as Sustained Antimicrobial Coating for Biomedical Application, *ACS Appl. Mater. Interfaces*, 2017, **9**(44), 38255.

6 J. Li, H. Zeng, Z. Zeng, Y. Zeng and T. Xie, Promising Graphene-Based Nanomaterials and Their Biomedical Applications and Potential Risks: A Comprehensive Review, *ACS Biomater. Sci. Eng.*, 2021, **7**(12), 5363.

7 K. Greben, S. Kovalchuk, A. M. Valencia, J. N. Kirchhof, S. Heeg, P. Rietsch, S. Reich, C. Cocchi, S. Eigler and K. I. Bolotin, In situ functionalization of graphene, *2D Mater.*, 2021, **8**(1), 015022.

8 V. Agarwal and K. Chatterjee, Recent advances in the field of transition metal dichalcogenides for biomedical applications, *Nanoscale*, 2018, **10**(35), 16365.

9 M. Liu, H. Zhu, Y. Wang, C. Sevencan and B. L. Li, Functionalized $MoS_2$-Based Nanomaterials for Cancer Phototherapy and Other Biomedical Applications, *ACS Mater. Lett.*, 2021, **3**(5), 462.

10 X. Zhou, H. Sun and X. Bai, Two-Dimensional Transition Metal Dichalcogenides: Synthesis, Biomedical Applications and Biosafety Evaluation, *Front. Bioeng. Biotechnol.*, 2020, **8**, 236.

11 S. Meng, Y. Zhang, H. Wang, L. Wang, T. Kong, H. Zhang and S. Meng, Recent advances on TMDCs for medical diagnosis, *Biomaterials*, 2021, **269**, 120471.

12 M. Jakubczak, A. Szuplewska, A. Rozmysłowska-Wojciechowska, A. Rosenkranz and A. M. Jastrzębska, Novel 2D MBenes—Synthesis, Structure, and Biotechnological Potential, *Adv. Funct. Mater.*, 2021, **31**(38), 2103048.

13 K. Khan, A. K. Tareen, M. Iqbal, L. Wang, C. Ma, Z. Shi, Z. Ye, W. Ahmad, R. U. Rehman Sagar and S. S. Shams, *et al.*, Navigating recent advances in monoelemental materials (Xenes)-fundamental to biomedical applications, *Prog. Solid State Chem.*, 2021, **63**, 100326.

14 S. Balendhran, S. Walia, H. Nili, S. Sriram and M. Bhaskaran, Elemental Analogues of Graphene: Silicene, Germanene, Stanene, and Phosphorene, *Small*, 2015, **11**(6), 640.

15 S. Sahoo, A. Sinha, N. A. Koshi, S.-C. Lee, S. Bhattacharjee and B. Muralidharan, Silicene: an excellent material for flexible electronics, *J. Phys. D: Appl. Phys.*, 2022, **55**(42), 425301.

16 G. Yang, F. Liu, J. Zhao, L. Fu, Y. Gu, L. Qu, C. Zhu, J.-J. Zhu and Y. Lin, MXenes-based nanomaterials for biosensing and biomedicine, *Coord. Chem. Rev.*, 2023, **479**, 215002.

17 K. Huang, Z. Li, J. Lin, G. Han and P. Huang, Two-dimensional transition metal carbides and nitrides (MXenes) for biomedical applications, *Chem. Soc. Rev.*, 2018, **47**(14), 5109.

18 K. A. S. Usman, J. Zhang, K. P. Marquez, M. A. N. Judicpa, P. A. Lynch, A. Bedford, B. Anasori and J. M. Razal, Recent advances and opportunities in MXene-based liquid crystals, *InfoMat*, 2024, **6**(3), e12516.

19 L. Jia, S. Zhou, A. Ahmed, Z. Yang, S. Liu, H. Wang, F. Li, M. Zhang, Y. Zhang and L. Sun, Tuning MXene electrical conductivity towards multifunctionality, *Chem. Eng. J.*, 2023, **475**, 146361.

20 H. Huang, C. Dong, W. Feng, Y. Wang, B. Huang and Y. Chen, Biomedical engineering of two-dimensional MXenes, *Adv. Drug Delivery Rev.*, 2022, **184**, 114178.

21 L. Lorencova, P. Kasak, N. Kosutova, M. Jerigova, E. Noskovicova, A. Vikartovska, M. Barath, P. Farkas and J. Tkac, MXene-based electrochemical devices applied for healthcare applications, *Microchim. Acta*, 2024, **191**(2), 88.

22 N. Ahmad, S. Rasheed, A. Mohyuddin, B. Fatima, M. I. Nabeel, M. T. Riaz, M. Najam-ul-Haq and D. Hussain, 2D MXenes and their composites; design, synthesis, and environmental sensing applications, *Chemosphere*, 2024, **352**, 141280.

23 S. Iravani and R. S. Varma, MXenes for Cancer Therapy and Diagnosis: Recent Advances and Current Challenges, *ACS Biomater. Sci. Eng.*, 2021, **7**(6), 1900.

24 R. Garg and F. Vitale, Latest advances on MXenes in biomedical research and health care, *MRS Bull.*, 2023, **48**(3), 283.

25 N. H. Solangi, S. A. Mazari, N. M. Mubarak, R. R. Karri, N. Rajamohan and D.-V. N. Vo, Recent trends in MXene-based material for biomedical applications, *Environ. Res.*, 2023, **222**, 115337.

26 A. Maleki, M. Ghomi, N. Nikfarjam, M. Akbari, E. Sharifi, M.-A. Shahbazi, M. Kermanian, M. Seyedhamzeh, E. Nazarzadeh Zare and M. Mehrali, *et al.*, Biomedical Applications of MXene-Integrated Composites: Regenerative Medicine, Infection Therapy, Cancer Treatment, and Biosensing, *Adv. Funct. Mater.*, 2022, **32**(34), 2203430.

27 C. Liu, Z. Feng, T. Yin, T. Wan, P. Guan, M. Li, L. Hu, C.-H. Lin, Z. Han and H. Xu, *et al.*, Multi-Interface

Engineering of MXenes for Self-Powered Wearable Devices, *Adv. Mater.*, 2024, **36**(42), 2403791.

28 A. Dey, S. Varagnolo, N. P. Power, N. Vangapally, Y. Elias, L. Damptey, B. N. Jaato, S. Gopalan, Z. Golrokhi and P. Sonar, *et al.*, Doped MXenes—A new paradigm in 2D systems: Synthesis, properties and applications, *Prog. Mater. Sci.*, 2023, **139**, 101166.

29 S. Hao, H. Han, Z. Yang, M. Chen, Y. Jiang, G. Lu, L. Dong, H. Wen, H. Li and J. Liu, *et al.*, Recent Advancements on Photothermal Conversion and Antibacterial Applications over MXenes-Based Materials, *Nano-Micro Lett.*, 2022, **14**(1), 178.

30 X. He, S. Koo, E. Obeng, A. Sharma, J. Shen and J. S. Kim, Emerging 2D MXenes for antibacterial applications: Current status, challenges, and prospects, *Coord. Chem. Rev.*, 2023, **492**, 215275.

31 D. H. Ho, Y. Y. Choi, S. B. Jo, J.-M. Myoung and J. H. Cho, Sensing with MXenes: Progress and Prospects, *Adv. Mater.*, 2021, **33**(47), 2005846.

32 B. Anasori and Y. Gogotsi, *2D Metal Carbides and Nitrides (MXenes): Structure, Properties and Applications*, Springer International Publishing, Cham, 2019, DOI: 10.1007/978-3-030-19026-2_1.

33 A. VahidMohammadi, J. Rosen and Y. Gogotsi, The world of two-dimensional carbides and nitrides (MXenes), *Science*, 2021, **372**(6547), eabf1581.

34 S. Abdolhosseinzadeh, X. Jiang, H. Zhang, J. Qiu and C. Zhang, Perspectives on solution processing of two-dimensional MXenes, *Mater. Today*, 2021, **48**, 214.

35 L. Meng, W. Wang, B. Xu, J. Qin, K. Zhang and H. Liu, Solution-Processed Flexible Transparent Electrodes for Printable Electronics, *ACS Nano*, 2023, **17**(5), 4180.

36 T. Y. Ko, H. Ye, G. Murali, S.-Y. Lee, Y. H. Park, J. Lee, J. Lee, D.-J. Yun, Y. Gogotsi and S. J. Kim, *et al.*, Functionalized MXene ink enables environmentally stable printed electronics, *Nat. Commun.*, 2024, **15**(1), 3459.

37 J. Miao, M. Tian, L. Qu and X. Zhang, Flexible, transparent and conductive wearable electronic skin based on 2D titanium carbide (MXene) ink, *Carbon*, 2024, **222**, 118950.

38 N. Driscoll, B. Erickson, B. B. Murphy, A. G. Richardson, G. Robbins, N. V. Apollo, G. Mentzelopoulos, T. Mathis, K. Hantanasirisakul and P. Bagga, *et al.*, MXene-infused bioelectronic interfaces for multiscale electrophysiology and stimulation, *Sci. Transl. Med.*, 2021, **13**(612), eabf8629.

39 H. Li, R. Fan, B. Zou, J. Yan, Q. Shi and G. Guo, Roles of MXenes in biomedical applications: recent developments and prospects, *J. Nanobiotechnol.*, 2023, **21**(1), 73.

40 F. Seidi, A. Arabi Shamsabadi, M. Dadashi Firouzjaei, M. Elliott, M. R. Saeb, Y. Huang, C. Li, H. Xiao and B. Anasori, MXenes Antibacterial Properties and Applications: A Review and Perspective, *Small*, 2023, **19**(14), 2206716.

41 M. Han, D. Zhang, A. Singh, T. Hryhorchuk, C. Eugene Shuck, T. Zhang, L. Bi, B. McBride, V. B. Shenoy and Y. Gogotsi, Versatility of infrared properties of MXenes, *Mater. Today*, 2023, **64**, 31.

42 W. Feng, X. Han, H. Hu, M. Chang, L. Ding, H. Xiang, Y. Chen and Y. Li, 2D vanadium carbide MXenzyme to alleviate ROS-mediated inflammatory and neurodegenerative diseases, *Nat. Commun.*, 2021, **12**(1), 2203.

43 K. Maleski, C. E. Shuck, A. T. Fafarman and Y. Gogotsi, The Broad Chromatic Range of Two-Dimensional Transition Metal Carbides, *Adv. Opt. Mater.*, 2021, **9**(4), 2001563.

44 T. Xu, S. Tan, S. Li, T. Chen, Y. Wu, Y. Hao, C. Liu and G. Ji, Synergistic Densification in Hybrid Organic-Inorganic MXenes for Optimized Photothermal Conversion, *Adv. Funct. Mater.*, 2024, **34**(29), 2400424.

45 S. L. Murray, S. Serajian, S. I. Gnani Peer Mohamed, S. Robinson, R. Krishnamoorthy, S. R. Das, M. Bavarian, S. Nejati, U. Kilic and M. Schubert, *et al.*, Ultrabroadband Optical Properties of 2D Titanium Carbide MXene, *ACS Appl. Mater. Interfaces*, 2024, 10, DOI: 10.1021/acsami.4c12079.

46 V. Neubertova, O. Guselnikova, Y. Yamauchi, A. Olshtrem, S. Rimpelova, E. Čižmár, M. Orendáč, J. Duchon, L. Volfova and J. Lancok, *et al.*, Covalent functionalization of $Ti_3C_2T$ MXene flakes with Gd-DTPA complex for stable and biocompatible MRI contrast agent, *Chem. Eng. J.*, 2022, **446**, 136939.

47 M. Aslam, T. Ahmad, M. H. Manzoor, Laiba and F. Verpoort, MXenes as theranostics: Diagnosis and therapy including *in vitro* and *in vivo* applications, *Appl. Mater. Today*, 2023, **35**, 102002.

48 V. Natu, M. Sokol, L. Verger and M. W. Barsoum, Effect of Edge Charges on Stability and Aggregation of $Ti_3C_2T_z$ MXene Colloidal Suspensions, *J. Phys. Chem. C*, 2018, **122**(48), 27745.

49 K. R. G. Lim, M. Shekhirev, B. C. Wyatt, B. Anasori, Y. Gogotsi and Z. W. Seh, Fundamentals of MXene synthesis, *Nat. Synth.*, 2022, **1**(8), 601.

50 T. Li, L. Yao, Q. Liu, J. Gu, R. Luo, J. Li, X. Yan, W. Wang, P. Liu and B. Chen, *et al.*, Fluorine-Free Synthesis of High-Purity $Ti_3C_2T$ (T = OH, O) *via* Alkali Treatment, *Angew. Chem., Int. Ed.*, 2018, **57**(21), 6115.

51 M. Alhabeb, K. Maleski, T. S. Mathis, A. Sarycheva, C. B. Hatter, S. Uzun, A. Levitt and Y. Gogotsi, Selective Etching of Silicon from $Ti_3SiC_2$ (MAX) To Obtain 2D Titanium Carbide (MXene), *Angew. Chem., Int. Ed.*, 2018, **57**(19), 5444.

52 M. Shekhirev, J. Busa, C. E. Shuck, A. Torres, S. Bagheri, A. Sinitskii and Y. Gogotsi, Ultralarge Flakes of $Ti_3C_2T_x$ MXene via Soft Delamination, *ACS Nano*, 2022, **16**(9), 13695.

53 J. Zhou, M. Dahlqvist, J. Björk and J. Rosen, Atomic Scale Design of MXenes and Their Parent Materials—From Theoretical and Experimental Perspectives, *Chem. Rev.*, 2023, **123**(23), 13291.

54 M. Downes, C. E. Shuck, B. McBride, J. Busa and Y. Gogotsi, Comprehensive synthesis of $Ti_3C_2T_x$ from MAX phase to MXene, *Nat. Protoc.*, 2024, **19**, 1807–1834.

55 T. S. Mathis, K. Maleski, A. Goad, A. Sarycheva, M. Anayee, A. C. Foucher, K. Hantanasirisakul, C. E. Shuck, E. A. Stach and Y. Gogotsi, Modified MAX Phase Synthesis for Environmentally Stable and Highly Conductive $Ti_3C_2$ MXene, *ACS Nano*, 2021, **15**(4), 6420.

56 A. Thakur, N. Chandran BS, K. Davidson, A. Bedford, H. Fang, Y. Im, V. Kanduri, B. C. Wyatt, S. K. Nemani and V. Poliukhova, *et al.*, Step-by-Step Guide for Synthesis and Delamination of $Ti_3C_2T_x$ MXene, *Small Methods*, 2023, **7**(8), 2300030.

57 C. E. Shuck, M. Han, K. Maleski, K. Hantanasirisakul, S. J. Kim, J. Choi, W. E. B. Reil and Y. Gogotsi, Effect of $Ti_3AlC_2$ MAX Phase on Structure and Properties of Resultant $Ti_3C_2T_x$ MXene, *ACS Appl. Nano Mater.*, 2019, **2**(6), 3368.

58 M. Anayee, N. Kurra, M. Alhabeb, M. Seredych, M. N. Hedhili, A.-H. Emwas, H. N. Alshareef, B. Anasori and Y. Gogotsi, Role of acid mixtures etching on the surface chemistry and sodium ion storage in $Ti_3C_2T_x$ MXene, *Chem. Commun.*, 2020, **56**(45), 6090.

59 M. Downes, C. E. Shuck, B. McBride, J. Busa and Y. Gogotsi, Comprehensive synthesis of $Ti_3C_2T_x$ from MAX phase to MXene, *Nat. Protoc.*, 2024, **19**, 1807–1834.

60 M. Ghidiu, M. R. Lukatskaya, M.-Q. Zhao, Y. Gogotsi and M. W. Barsoum, Conductive two-dimensional titanium carbide 'clay' with high volumetric capacitance, *Nature*, 2014, **516**(7529), 78.

61 A. Lipatov, M. Alhabeb, M. R. Lukatskaya, A. Boson, Y. Gogotsi and A. Sinitskii, Effect of Synthesis on Quality, Electronic Properties and Environmental Stability of Individual Monolayer $Ti_3C_2$ MXene Flakes, *Adv. Electron. Mater.*, 2016, **2**(12), 1600255.

62 F. Shahzad, M. Alhabeb, C. B. Hatter, B. Anasori, S. Man Hong, C. M. Koo and Y. Gogotsi, Electromagnetic interference shielding with 2D transition metal carbides (MXenes), *Science*, 2016, **353**(6304), 1137.

63 M. Naguib, M. Kurtoglu, V. Presser, J. Lu, J. Niu, M. Heon, L. Hultman, Y. Gogotsi and M. W. Barsoum, Two-Dimensional Nanocrystals Produced by Exfoliation of $Ti_3AlC_2$, *Adv. Mater.*, 2011, **23**(37), 4248.

64 M. Alhabeb, K. Maleski, B. Anasori, P. Lelyukh, L. Clark, S. Sin and Y. Gogotsi, Guidelines for Synthesis and Processing of Two-Dimensional Titanium Carbide ($Ti_3C_2T_x$ MXene), *Chem. Mater.*, 2017, **29**(18), 7633.

65 C. E. Shuck, K. Ventura-Martinez, A. Goad, S. Uzun, M. Shekhirev and Y. Gogotsi, Safe Synthesis of MAX and MXene: Guidelines to Reduce Risk During Synthesis, *ACS Chem. Health Saf.*, 2021, **28**(5), 326.

66 O. Mashtalir, M. Naguib, B. Dyatkin, Y. Gogotsi and M. W. Barsoum, Kinetics of aluminum extraction from $Ti_3AlC_2$ in hydrofluoric acid, *Mater. Chem. Phys.*, 2013, **139**(1), 147.

67 M. Anayee, C. E. Shuck, M. Shekhirev, A. Goad, R. Wang and Y. Gogotsi, Kinetics of $Ti_3AlC_2$ Etching for $Ti_3C_2T_x$ MXene Synthesis, *Chem. Mater.*, 2022, **34**(21), 9589.

68 Y.-J. Kim, S. J. Kim, D. Seo, Y. Chae, M. Anayee, Y. Lee, Y. Gogotsi, C. W. Ahn and H.-T. Jung, Etching Mechanism of Monoatomic Aluminum Layers during MXene Synthesis, *Chem. Mater.*, 2021, **33**(16), 6346.

69 L. Verger, V. Natu, M. Ghidiu and M. W. Barsoum, Effect of Cationic Exchange on the Hydration and Swelling Behavior of $Ti_3C_2T_z$ MXenes, *J. Phys. Chem. C*, 2019, **123**(32), 20044.

70 C. A. Voigt, M. Ghidiu, V. Natu and M. W. Barsoum, Anion Adsorption, $Ti_3C_2T_z$ MXene Multilayers, and Their Effect on Claylike Swelling, *J. Phys. Chem. C*, 2018, **122**(40), 23172.

71 S. Kajiyama, L. Szabova, H. Iinuma, A. Sugahara, K. Gotoh, K. Sodeyama, Y. Tateyama, M. Okubo and A. Yamada, Enhanced Li-Ion Accessibility in MXene Titanium Carbide by Steric Chloride Termination, *Adv. Energy Mater.*, 2017, **7**(9), 1601873.

72 K. Matthews, T. Zhang, C. E. Shuck, A. VahidMohammadi and Y. Gogotsi, Guidelines for Synthesis and Processing of Chemically Stable Two-Dimensional $V_2CT_x$ MXene, *Chem. Mater.*, 2022, **34**(2), 499.

73 K. L. Firestein, J. F. S. Fernando, C. Zhang, C.-E. M. Lewis and D. V. Golberg, Delaminated V2C MXene Nanostructures Prepared via LiF Salt Etching for Electrochemical Applications, *ACS Appl. Nano Mater.*, 2022, **5**(9), 12117.

74 Q. Shan, X. Mu, M. Alhabeb, C. E. Shuck, D. Pang, X. Zhao, X.-F. Chu, Y. Wei, F. Du and G. Chen, *et al.*, Two-dimensional vanadium carbide (V2C) MXene as electrode for supercapacitors with aqueous electrolytes, *Electrochem. Commun.*, 2018, **96**, 103.

75 M. Naguib, R. R. Unocic, B. L. Armstrong and J. Nanda, Large-scale delamination of multi-layers transition metal carbides and carbonitrides "MXenes", *Dalton Trans.*, 2015, **44**(20), 9353.

76 M. Han, C. E. Shuck, R. Rakhmanov, D. Parchment, B. Anasori, C. M. Koo, G. Friedman and Y. Gogotsi, Beyond $Ti_3C_2T_x$: MXenes for Electromagnetic Interference Shielding, *ACS Nano*, 2020, **14**(4), 5008.

77 G. Ying, A. D. Dillon, A. T. Fafarman and M. W. Barsoum, Transparent, conductive solution processed spincast 2D $Ti_2CT_x$ (MXene) films, *Mater. Res. Lett.*, 2017, **5**(6), 391.

78 A. N. Giordano, J. Jiang, A. Advincula, K. Shevchuk, M. S. Carey, T. C. Back, Y. Gogotsi, D. Nepal, R. Pachter and R. Rao, Raman Spectroscopy and Laser-Induced Surface Modification of Nb2CTx MXene, *ACS Mater. Lett.*, 2024, **6**(8), 3264–3271, DOI: 10.1021/acsmaterialslett.4c00922.

79 X. Zhu, K. Yang, Z. Zhang, S. He, Z. Shen, W. Jiang, Y. Huang, Y. Xu, Q. Jiang and L. Pan, *et al.*, Additive-Free Anode with High Stability: Nb2CTx MXene Prepared by HCl-LiF Hydrothermal Etching for Lithium-Ion Batteries, *ACS Appl. Mater. Interfaces*, 2024, **16**(22), 28709.

80 M. Seredych, C. E. Shuck, D. Pinto, M. Alhabeb, E. Precetti, G. Deysher, B. Anasori, N. Kurra and Y. Gogotsi, High-Temperature Behavior and Surface Chemistry of Carbide MXenes Studied by Thermal Analysis, *Chem. Mater.*, 2019, **31**(9), 3324.

81 B. Anasori, Y. Xie, M. Beidaghi, J. Lu, B. C. Hosler, L. Hultman, P. R. C. Kent, Y. Gogotsi and M. W. Barsoum, Two-Dimensional, Ordered, Double Transition Metals Carbides (MXenes), *ACS Nano*, 2015, **9**(10), 9507.

82 A. Thakur, N. Chandran BS, K. Davidson, A. Bedford, H. Fang, Y. Im, V. Kanduri, B. C. Wyatt, S. K. Nemani and V. Poliukhova, *et al.*, Step-by-Step Guide for Synthesis and Delamination of $Ti_3C_2T$ MXene, *Small Methods*, 2023, **7**(8), 2300030.

83 J. Li, M. Lu, W. Zheng and W. Zhang, Ion-intercalation architecture for robust functionalization of two-dimensional MXenes, *Energy Storage Mater.*, 2024, **64**, 103068.

84 H. Chen, H. Ma and C. Li, Host–Guest Intercalation Chemistry in MXenes and Its Implications for Practical Applications, *ACS Nano*, 2021, **15**(10), 15502.

85 M. Ghidiu, J. Halim, S. Kota, D. Bish, Y. Gogotsi and M. W. Barsoum, Ion-Exchange and Cation Solvation Reactions in $Ti_3C_2$ MXene, *Chem. Mater.*, 2016, **28**(10), 3507.

86 V. Natu, R. Pai, O. Wilson, E. Gadasu, H. Badr, A. Karmakar, A. J. D. Magenau, V. Kalra and M. W. Barsoum, Effect of Base/Nucleophile Treatment on Interlayer Ion Intercalation, Surface Terminations, and Osmotic Swelling of $Ti_3C_2T_z$ MXene Multilayers, *Chem. Mater.*, 2022, **34**(2), 678.

87 J. L. Hart, K. Hantanasirisakul, A. C. Lang, B. Anasori, D. Pinto, Y. Pivak, J. T. van Omme, S. J. May, Y. Gogotsi and M. L. Taheri, Control of MXenes' electronic properties through termination and intercalation, *Nat. Commun.*, 2019, **10**(1), 522.

88 L. Lei, J. Yin, K. Wu and N. Yang, Size-Dependent Electrochemistry of Oxygenated $Ti_3C_2T_x$ MXenes, *Small Methods*, 2023, **7**(6), 2300302.

89 S. Yi, L. Wang, X. Zhang, C. Li, W. Liu, K. Wang, X. Sun, Y. Xu, Z. Yang and Y. Cao, *et al.*, Cationic intermediates assisted self-assembly two-dimensional $Ti_3C_2T_x$/rGO hybrid nanoflakes for advanced lithium-ion capacitors, *Sci. Bull.*, 2021, **66**(9), 914.

90 L. Wang, X. Zhang, Y. Xu, C. Li, W. Liu, S. Yi, K. Wang, X. Sun, Z.-S. Wu and Y. Ma, Tetrabutylammonium-Intercalated 1T-$MoS_2$ Nanosheets with Expanded Interlayer Spacing Vertically Coupled on 2D Delaminated MXene for High-Performance Lithium-Ion Capacitors, *Adv. Funct. Mater.*, 2021, **31**(36), 2104286.

91 Y. Long, Y. Tao, T. Shang, H. Yang, Z. Sun, W. Chen and Q.-H. Yang, Roles of Metal Ions in MXene Synthesis, Processing and Applications: A Perspective, *Adv. Sci.*, 2022, **9**(12), 2200296.

92 S. Célérier, S. Hurand, C. Garnero, S. Morisset, M. Benchakar, A. Habrioux, P. Chartier, V. Mauchamp, N. Findling and B. Lanson, *et al.*, Hydration of $Ti_3C_2T_x$ MXene: An Interstratification Process with Major Implications on Physical Properties, *Chem. Mater.*, 2019, **31**(2), 454.

93 E. S. Muckley, M. Naguib, H.-W. Wang, L. Vlcek, N. C. Osti, R. L. Sacci, X. Sang, R. R. Unocic, Y. Xie and M. Tyagi, *et al.*, Multimodality of Structural, Electrical, and Gravimetric Responses of Intercalated MXenes to Water, *ACS Nano*, 2017, **11**(11), 11118.

94 Y. Deng, T. Shang, Z. Wu, Y. Tao, C. Luo, J. Liang, D. Han, R. Lyu, C. Qi and W. Lv, *et al.*, Fast Gelation of $Ti_3C_2T_x$ MXene Initiated by Metal Ions, *Adv. Mater.*, 2019, **31**(43), 1902432.

95 D. W. Smith, Ionic hydration enthalpies, *J. Chem. Educ.*, 1977, **54**(9), 540.

96 B. C. Wyatt, M. G. Boebinger, Z. D. Hood, S. Adhikari, P. P. Michałowski, S. K. Nemani, M. G. Muraleedharan, A. Bedford, W. J. Highland and P. R. C. Kent, *et al.*, Alkali cation stabilization of defects in 2D MXenes at ambient and elevated temperatures, *Nat. Commun.*, 2024, **15**(1), 6353.

97 N. Goossens, K. Lambrinou, B. Tunca, V. Kotasthane, M. C. Rodríguez González, A. Bazylevska, P. O. Å. Persson, S. De Feyter, M. Radovic and F. Molina-Lopez, *et al.*, Upscaled Synthesis Protocol for Phase-Pure, Colloidally Stable MXenes with Long Shelf Lives, *Small Methods*, 2024, **8**(1), 2300776.

98 Y. C. Jee, J. S. Yun, S. H. Im and W.-S. Kim, Environment-friendly synthesis of $Ti_3C_2T_x$ MXene by etching and galvanic reactions for Al removal of $Ti_3AlC_2$ MAX, *Chem. Eng. J.*, 2024, **495**, 153354.

99 A. Gentile, S. Marchionna, M. Balordi, G. Pagot, C. Ferrara, V. Di Noto and R. Ruffo, Critical Analysis of MXene Production with In-Situ HF Forming Agents for Sustainable Manufacturing, *ChemElectroChem*, 2022, **9**(23), e202200891.

100 D. D. Kruger, H. García and A. Primo, Molten Salt Derived MXenes: Synthesis and Applications, *Adv. Sci.*, 2024, **11**(35), 2307106.

101 Y. Li, H. Shao, Z. Lin, J. Lu, L. Liu, B. Duployer, P. O. Å. Persson, P. Eklund, L. Hultman and M. Li, *et al.*, A general Lewis acidic etching route for preparing MXenes with enhanced electrochemical performance in non-aqueous electrolyte, *Nat. Mater.*, 2020, **19**(8), 894.

102 M. Li, J. Lu, K. Luo, Y. Li, K. Chang, K. Chen, J. Zhou, J. Rosen, L. Hultman and P. Eklund, *et al.*, Element Replacement Approach by Reaction with Lewis Acidic Molten Salts to Synthesize Nanolaminated MAX Phases and MXenes, *J. Am. Chem. Soc.*, 2019, **141**(11), 4730.

103 S. Kumar, Fluorine-Free MXenes: Recent Advances, Synthesis Strategies, and Mechanisms, *Small*, 2024, **20**(16), 2308225.

104 L. Liu, M. Orbay, S. Luo, S. Duluard, H. Shao, J. Harmel, P. Rozier, P.-L. Taberna and P. Simon, Exfoliation and Delamination of $Ti_3C_2T_x$ MXene Prepared *via* Molten Salt Etching Route, *ACS Nano*, 2022, **16**(1), 111.

105 A. Jawaid, A. Hassan, G. Neher, D. Nepal, R. Pachter, W. J. Kennedy, S. Ramakrishnan and R. A. Vaia, Halogen Etch of $Ti_3AlC_2$ MAX Phase for MXene Fabrication, *ACS Nano*, 2021, **15**(2), 2771.

106 H. Shi, P. Zhang, Z. Liu, S. Park, M. R. Lohe, Y. Wu, A. Shaygan Nia, S. Yang and X. Feng, Ambient-Stable Two-Dimensional Titanium Carbide (MXene) Enabled by Iodine Etching, *Angew. Chem., Int. Ed.*, 2021, **60**(16), 8689.

107 V. Natu, R. Pai, M. Sokol, M. Carey, V. Kalra and M. W. Barsoum, 2D $Ti_3C_2T_z$ MXene Synthesized by Water-free Etching of $Ti_3AlC_2$ in Polar Organic Solvents, *Chem*, 2020, **6**(3), 616.

108 S. Gong, F. Zhao, Y. Zhang, H. Xu, M. Li, J. Qi, H. Wang, Z. Wang, Y. Hu and X. Fan, *et al.*, Few-layered $Ti_3C_2T_x$ MXene synthesized via water-free etching toward high-performance supercapacitors, *J. Colloid Interface Sci.*, 2023, **632**, 216.

109 W. Sun, S. A. Shah, Y. Chen, Z. Tan, H. Gao, T. Habib, M. Radovic and M. J. Green, Electrochemical etching of $Ti_2AlC$ to $Ti_2CT_x$ (MXene) in low-concentration hydrochloric acid solution, *J. Mater. Chem. A*, 2017, **5**(41), 21663.

110 S. Yang, P. Zhang, F. Wang, A. G. Ricciardulli, M. R. Lohe, P. W. M. Blom and X. Feng, Fluoride-Free Synthesis of Two-Dimensional Titanium Carbide (MXene) Using A Binary Aqueous System, *Angew. Chem., Int. Ed.*, 2018, **57**(47), 15491.

111 M. Shen, W. Jiang, K. Liang, S. Zhao, R. Tang, L. Zhang and J.-Q. Wang, One-Pot Green Process to Synthesize MXene with Controllable Surface Terminations using Molten Salts, *Angew. Chem., Int. Ed.*, 2021, **60**(52), 27013.

112 M. Song, S.-Y. Pang, F. Guo, M.-C. Wong and J. Hao, Fluoride-Free 2D Niobium Carbide MXenes as Stable and Biocompatible Nanoplatforms for Electrochemical Biosensors with Ultrahigh Sensitivity, *Adv. Sci.*, 2020, **7**(24), 2001546.

113 B. Richard, C. Shahana, R. Vivek, M. Amarendar Reddy and P. A. Rasheed, Acoustic platforms meet MXenes – a new paradigm shift in the palette of biomedical applications, *Nanoscale*, 2023, **15**(45), 18156.

114 A. E. Ghazaly, H. Ahmed, A. R. Rezk, J. Halim, P. O. Å. Persson, L. Y. Yeo and J. Rosen, Ultrafast, One-Step, Salt-Solution-Based Acoustic Synthesis of $Ti_3C_2$ MXene, *ACS Nano*, 2021, **15**(3), 4287.

115 H. Alijani, A. R. Rezk, M. M. Khosravi Farsani, H. Ahmed, J. Halim, P. Reineck, B. J. Murdoch, A. El-Ghazaly, J. Rosen and L. Y. Yeo, Acoustomicrofluidic Synthesis of Pristine Ultrathin $Ti_3C_2T_z$ MXene Nanosheets and Quantum Dots, *ACS Nano*, 2021, **15**(7), 12099.

116 A. M. Amani, L. Tayebi, E. Vafa, M. Abbasi, A. Vaez, H. Kamyab, S. Chelliapan, M. J. Azizli and R. Bazargan-Lari, On the horizon of greener pathways to travel into a greener future portal: Green MXenes, environment-friendly synthesis, and their innovative applications, *J. Cleaner Prod.*, 2024, **436**, 140606.

117 S. Jin, Y. Guo, F. Wang and A. Zhou, The synthesis of MXenes, *MRS Bull.*, 2023, **48**(3), 245.

118 M. A. Saeed, M. Z. Qamar, Z. Khalid, E. Chamanehpour and Y. K. Mishra, Two-dimensional MXenes: A route from synthesis to applications in self-powered IoT devices, *Chem. Eng. J.*, 2024, **490**, 151600.

119 D. Wang, C. Zhou, A. S. Filatov, W. Cho, F. Lagunas, M. Wang, S. Vaikuntanathan, C. Liu, R. F. Klie and D. V. Talapin, Direct synthesis and chemical vapor deposition of 2D carbide and nitride MXenes, *Science*, 2023, **379**(6638), 1242.

120 N. Sirotkin, A. Khlyustova and A. Agafonov, Plasma-Liquid Synthesis as a New Method for the Production of MXenes, *Plasma Chem. Plasma Process.*, 2024, **44**(4), 1853.

121 Z. U. D. Babar, B. Della Ventura, R. Velotta and V. Iannotti, Advances and emerging challenges in MXenes and their nanocomposites for biosensing applications, *RSC Adv.*, 2022, **12**(30), 19590.

122 R. Cheng, T. Hu, M. Hu, C. Li, Y. Liang, Z. Wang, H. Zhang, M. Li, H. Wang and H. Lu, *et al.*, MXenes induce epitaxial growth of size-controlled noble nanometals: A case study for surface enhanced Raman scattering (SERS), *J. Mater. Sci. Technol.*, 2020, **40**, 119.

123 M. Shin, S. Yang, H. W. Kwak and K. H. Lee, Synthesis of gold nanoparticles using silk sericin as a green reducing and capping agent, *Eur. Polym. J.*, 2022, **164**, 110960.

124 Z. Zhang, H. Li, G. Zou, C. Fernandez, B. Liu, Q. Zhang, J. Hu and Q. Peng, Self-Reduction Synthesis of New MXene/Ag Composites with Unexpected Electrocatalytic Activity, *ACS Sustainable Chem. Eng.*, 2016, **4**(12), 6763.

125 Y. Wang, P. Zhao, B. Gao, M. Yuan, J. Yu, Z. Wang and X. Chen, Self-reduction of bimetallic nanoparticles on flexible MXene-graphene electrodes for simultaneous detection of ascorbic acid, dopamine, and uric acid, *Microchem. J.*, 2023, **185**, 108177.

126 E. Satheeshkumar, T. Makaryan, A. Melikyan, H. Minassian, Y. Gogotsi and M. Yoshimura, One-step Solution Processing of Ag, Au and Pd@MXene Hybrids for SERS, *Sci. Rep.*, 2016, **6**(1), 32049.

127 K. Li, T. Jiao, R. Xing, G. Zou, J. Zhou, L. Zhang and Q. Peng, Fabrication of tunable hierarchical MXene@AuNPs nanocomposites constructed by self-reduction reactions with enhanced catalytic performances, *Sci. China Mater.*, 2018, **61**(5), 728.

128 H. Xie, P. Li, J. Shao, H. Huang, Y. Chen, Z. Jiang, P. K. Chu and X.-F. Yu, Electrostatic Self-Assembly of $Ti_3C_2T_x$ MXene and Gold Nanorods as an Efficient Surface-Enhanced Raman Scattering Platform for Reliable and High-Sensitivity Determination of Organic Pollutants, *ACS Sens.*, 2019, **4**(9), 2303.

129 J. Wang, Q. Xu, J. Liu, W. Kong and L. Shi, Electrostatic Self-Assembly of MXene on Ruthenium Dioxide-Modified Carbon Cloth for Electrochemical Detection of Kaempferol, *Small*, 2023, **19**(34), 2301709.

130 H. Niu, X. Yang, Q. Wang, X. Jing, K. Cheng, K. Zhu, K. Ye, G. Wang, D. Cao and J. Yan, Electrostatic self-assembly of MXene and edge-rich CoAl layered double hydroxide on molecular-scale with superhigh volumetric performances, *J. Energy Chem.*, 2020, **46**, 105.

131 T. Basak and T. Basak, Edge Modification and Site-Selective Functionalization of Graphene Quantum Dots: A Versatile Technique for Designing Tunable Optoelectronic and Sensing Devices, *J. Phys. Chem. A*, 2023, **127**(25), 5335.

132 S. Soman, S. Kulkarni, A. Pandey, N. Dhas, K. S. Shirur, R. S. Gude, S. M. Vidya, S. Nayak, S. D. George and S. Mutalik, Unlocking the power of MXenes – Crafting a 2D nanoplatform for tomorrow: Synthesis, functionalization, stability, and biomedical applications, *Mater. Today Commun.*, 2024, **38**, 107711.

133 X. Wu, J. Gong, H. Zhang, Y. Wang and F. Tan, Cellular uptake and cytotoxicity of PEGylated MXene nanomaterials mediated by protein corona, *Sci. Total Environ.*, 2024, **912**, 169227.

134 M. Sai Bhargava Reddy and S. Aich, Recent progress in surface and heterointerface engineering of 2D MXenes for

gas sensing applications, *Coord. Chem. Rev.*, 2024, **500**, 215542.

135 Y. Deng, Y. Wang, M. Lin, Y. Chen, Z.-J. Qian, J. Liu and X. Li, High-Density Au Anchored to $Ti_3C_2$-Based Colorimetric-Fluorescence Dual-Mode Lateral Flow Immunoassay for All-Domain-Enhanced Performance and Signal Intercalibration, *Anal. Chem.*, 2024, **96**(13), 5106.

136 U. Amara, I. Hussain, M. Ahmad, K. Mahmood and K. Zhang, 2D MXene-Based Biosensing: A Review, *Small*, 2023, **19**(2), 2205249.

137 U. Amara; L. Xu; I. Hussain; K. Yang; H. Hu and D. Ho MXene Hydrogels for Soft Multifunctional Sensing: A Synthesis-Centric Review, 2405047, DOI: 10.1002/smll.202405047.

138 J. Wang, M. Shen, Z. Liu and W. Wang, MXene materials for advanced thermal management and thermal energy utilization, *Nano Energy*, 2022, **97**, 107177.

139 T. Guo, D. Zhou, S. Deng, M. Jafarpour, J. Avaro, A. Neels, J. Heier and C. Zhang, Rational Design of $Ti_3C_2T_x$ MXene Inks for Conductive, Transparent Films, *ACS Nano*, 2023, **17**(4), 3737.

140 I. C. Lee, Y.-C. E. Li, J. L. Thomas, M.-H. Lee and H.-Y. Lin, Recent advances using MXenes in biomedical applications, *Mater. Horiz.*, 2024, **11**(4), 876.

141 J. V. M. Lima, H. G. Lemos, R. A. Silva, J. H. H. Rossato, M. H. Boratto and C. F. O. Graeff, Tailoring interlayer spacing of $Ti_3C_2T_x$ MXene with organic acid doped polyaniline and polypyrrole for more stable supercapacitors, *J. Alloys Compd. Commun.*, 2024, **3**, 100007.

142 M. Lu, W. Han, H. Li, W. Zhang and B. Zhang, There is plenty of space in the MXene layers: The confinement and fillings, *J. Energy Chem.*, 2020, **48**, 344.

143 A. Zamhuri, G. P. Lim, N. L. Ma, K. S. Tee and C. F. Soon, MXene in the lens of biomedical engineering: synthesis, applications and future outlook, *Biomed. Eng. Online*, 2021, **20**(1), 33.

144 Y. Wang, W. Feng and Y. Chen, Chemistry of two-dimensional MXene nanosheets in theranostic nanomedicine, *Chin. Chem. Lett.*, 2020, **31**(4), 937.

145 X. Han, J. Huang, H. Lin, Z. Wang, P. Li and Y. Chen, 2D Ultrathin MXene-Based Drug-Delivery Nanoplatform for Synergistic Photothermal Ablation and Chemotherapy of Cancer, *Adv. Healthcare Mater.*, 2018, **7**(9), 1701394.

146 C. Dai, H. Lin, G. Xu, Z. Liu, R. Wu and Y. Chen, Biocompatible 2D Titanium Carbide (MXenes) Composite Nanosheets for pH-Responsive MRI-Guided Tumor Hyperthermia, *Chem. Mater.*, 2017, **29**(20), 8637.

147 H. Lin, X. Wang, L. Yu, Y. Chen and J. Shi, Two-Dimensional Ultrathin MXene Ceramic Nanosheets for Photothermal Conversion, *Nano Lett.*, 2017, **17**(1), 384.

148 C. Dai, Y. Chen, X. Jing, L. Xiang, D. Yang, H. Lin, Z. Liu, X. Han and R. Wu, Two-Dimensional Tantalum Carbide (MXenes) Composite Nanosheets for Multiple Imaging-Guided Photothermal Tumor Ablation, *ACS Nano*, 2017, **11**(12), 12696.

149 Z. Liu, H. Lin, M. Zhao, C. Dai, S. Zhang, W. Peng and Y. J. T. Chen, 2D superparamagnetic tantalum carbide composite MXenes for efficient breast-cancer theranostics, *Theranostics*, 2018, **8**(6), 1648.

150 X. Han, X. Jing, D. Yang, H. Lin, Z. Wang, H. Ran, P. Li and Y. J. T. Chen, Therapeutic mesopore construction on 2D Nb2C MXenes for targeted and enhanced chemo-photothermal cancer therapy in NIR-II biowindow, *Theranostics*, 2018, **8**(16), 4491.

151 H. Lin, S. Gao, C. Dai, Y. Chen and J. Shi, A Two-Dimensional Biodegradable Niobium Carbide (MXene) for Photothermal Tumor Eradication in NIR-I and NIR-II Biowindows, *J. Am. Chem. Soc.*, 2017, **139**(45), 16235.

152 W. Feng, R. Wang, Y. Zhou, L. Ding, X. Gao, B. Zhou, P. Hu and Y. Chen, Ultrathin Molybdenum Carbide MXene with Fast Biodegradability for Highly Efficient Theory-Oriented Photonic Tumor Hyperthermia, *Adv. Funct. Mater.*, 2019, **29**(22), 1901942.

153 M. Wu, J. Yang, T. Ye, B. Wang, Y. Tang and X. Ying, Efficient Drug Delivery of $Ti_3C_2T_x$ MXenes for Synergistic Treatment of Human Hypopharyngeal Squamous Cell Carcinoma, *ACS Appl. Mater. Interfaces*, 2023, **15**(25), 29939.

154 Q. Qiao, J. Wang, B. Li, Y. Guo, T. Liao, Z. Xu, Y. Kuang and C. Li, $Ti_3C_2T_x$ MXene nanosheet-based drug delivery/cascaded enzyme system for combination cancer therapy and anti-inflammation, *Appl. Mater. Today*, 2024, **38**, 102215.

155 Y. Ma, T. Jiang, R. Zhang, F. Liu, S. Song, H. Zhang, J. Huang and Z. He, The Application of 2d Mxene Nanosheet -Based Thermosensitive Gel Delivery System Loaded with Cisplatin and Imiquimod for Lung Cancer, *Int. J. Nanomed.*, 2024, **19**, 4719.

156 R. P. Pandey, P. A. Rasheed, T. Gomez, K. Rasool, J. Ponraj, K. Prenger, M. Naguib and K. A. Mahmoud, Effect of Sheet Size and Atomic Structure on the Antibacterial Activity of Nb-MXene Nanosheets, *ACS Appl. Nano Mater.*, 2020, **3**(11), 11372.

157 F. Wang, C. Yang, C. Duan, D. Xiao, Y. Tang and J. Zhu, An Organ-Like Titanium Carbide Material (MXene) with Multilayer Structure Encapsulating Hemoglobin for a Mediator-Free Biosensor, *J. Electrochem. Soc.*, 2015, **162**(1), B16.

158 H. L. Chia, C. C. Mayorga-Martinez, N. Antonatos, Z. Sofer, J. J. Gonzalez-Julian, R. D. Webster and M. Pumera, MXene Titanium Carbide-based Biosensor: Strong Dependence of Exfoliation Method on Performance, *Anal. Chem.*, 2020, **92**(3), 2452.

159 L. Lorencova, T. Bertok, E. Dosekova, A. Holazova, D. Paprckova, A. Vikartovska, V. Sasinkova, J. Filip, P. Kasak and M. Jerigova, *et al.*, Electrochemical performance of $Ti_3C_2T_x$ MXene in aqueous media: towards ultrasensitive H2O2 sensing, *Electrochim. Acta*, 2017, **235**, 471.

160 P. Nayak, Q. Jiang, R. Mohanraman, D. Anjum, M. N. Hedhili and H. N. Alshareef, Inherent electrochemistry and charge transfer properties of few-layered two-dimensional $Ti_3C_2T_x$ MXene, *Nanoscale*, 2018, **10**(36), 17030.

161 P. Abdul Rasheed, R. P. Pandey, T. Gomez, K. A. Jabbar, K. Prenger, M. Naguib, B. Aïssa and K. A. Mahmoud, Nb-based MXenes for efficient electrochemical sensing of

small biomolecules in the anodic potential, *Electrochem. Commun.*, 2020, **119**, 106811.

162 N. Noriega, M. Shekhirev, C. E. Shuck, J. Salvage, A. VahidMohammadi, M. K. Dymond, J. Lacey, S. Sandeman, Y. Gogotsi and B. A. Patel, Pristine $Ti_3C_2T_x$ MXene Enables Flexible and Transparent Electrochemical Sensors, *ACS Appl. Mater. Interfaces*, 2024, **16**(5), 6569.

163 S. Hideshima, Y. Ogata, D. Takimoto, Y. Gogotsi and W. Sugimoto, Vertically aligned MXene bioelectrode prepared by freeze-drying assisted electrophoretic deposition for sensitive electrochemical protein detection, *Biosens. Bioelectron.*, 2024, **250**, 116036.

164 S. Kumar, Y. Lei, N. H. Alshareef, M. A. Quevedo-Lopez and K. N. Salama, Biofunctionalized two-dimensional $Ti_3C_2$ MXenes for ultrasensitive detection of cancer biomarker, *Biosens. Bioelectron.*, 2018, **121**, 243.

165 M. H. M. Facure, G. Gahramanova, D. Zhang, T. Zhang, C. E. Shuck, L. A. Mercante, D. S. Correa and Y. Gogotsi, All-MXene electronic tongue for neurotransmitters detection, *Biosens. Bioelectron.*, 2024, **262**, 116526.

166 X. Zhu, B. Liu, H. Hou, Z. Huang, K. M. Zeinu, L. Huang, X. Yuan, D. Guo, J. Hu and J. Yang, Alkaline intercalation of $Ti_3C_2$ MXene for simultaneous electrochemical detection of Cd(II), Pb(II), Cu(II) and Hg(II), *Electrochim. Acta*, 2017, **248**, 46.

167 P. A. Rasheed, R. P. Pandey, K. Rasool and K. A. Mahmoud, Ultra-sensitive electrocatalytic detection of bromate in drinking water based on Nafion/$Ti_3C_2T_x$ (MXene) modified glassy carbon electrode, *Sens. Actuators, B*, 2018, **265**, 652.

168 P. A. Rasheed, R. P. Pandey, K. A. Jabbar and K. A. Mahmoud, Nb4C3Tx (MXene)/Au/DNA Aptasensor for the Ultraselective Electrochemical Detection of Lead in Water Samples, *Electroanalysis*, 2022, **34**(10), 1540.

169 K. Shevchuk, A. Sarycheva and Y. Gogotsi, Evaluation of two-dimensional transition-metal carbides and carbonitrides (MXenes) for SERS substrates, *MRS Bull.*, 2022, **47**(6), 545.

170 M. Wan, J. Zhou, H. Yang, X. Dai, Y. Zheng, Z. Xia and L. Wang, Covalently N-Doped MXene Quantum Dots for Highly Stable Fluorescent $Cu^{2+}$ Ion Sensor, *ACS Appl. Nano Mater.*, 2022, **5**(8), 11715.

171 H. Pazniak, I. A. Plugin, M. J. Loes, T. M. Inerbaev, I. N. Burmistrov, M. Gorshenkov, J. Polcak, A. S. Varezhnikov, M. Sommer and D. V. Kuznetsov, *et al.*, Partially Oxidized $Ti_3C_2T_x$ MXenes for Fast and Selective Detection of Organic Vapors at Part-per-Million Concentrations, *ACS Appl. Nano Mater.*, 2020, **3**(4), 3195.

172 S. Zhang, Z. Qi and Y. Li, Alkali preparation and ions detection of $Ti_3C_2$ quantum dots, *Ceram. Int.*, 2022, **48**(15), 21118.

173 S. Mehdi Aghaei, A. Aasi and B. Panchapakesan, Experimental and Theoretical Advances in MXene-Based Gas Sensors, *ACS Omega*, 2021, **6**(4), 2450.

174 H. Wen, P. Liu, Z. Jiang, H. Peng and H. Liu, Redox-responsive MXene-SS-PEG nanomaterials for delivery of doxorubicin, *Inorg. Chem. Commun.*, 2023, **147**, 110227.

175 X. Zhang, L. Cheng, Y. Lu, J. Tang, Q. Lv, X. Chen, Y. Chen and J. Liu, A MXene-Based Bionic Cascaded-Enzyme Nanoreactor for Tumor Phototherapy/Enzyme Dynamic Therapy and Hypoxia-Activated Chemotherapy, *Nano-Micro Lett.*, 2021, **14**(1), 22.

176 Y. Xu, Y. Wang, J. An, A. C. Sedgwick, M. Li, J. Xie, W. Hu, J. Kang, S. Sen and A. Steinbrueck, *et al.*, 2D-ultrathin MXene/DOXjade platform for iron chelation chemo-photothermal therapy, *Bioact. Mater.*, 2022, **14**, 76.

177 Z. Hao, Y. Li, X. Liu, T. Jiang, Y. He, X. Zhang, C. Cong, D. Wang, Z. Liu and D. Gao, Enhancing biocatalysis of a MXene-based biomimetic plasmonic assembly for targeted cancer treatments in NIR-II biowindow, *Chem. Eng. J.*, 2021, **425**, 130639.

178 B. Lu, S. Hu, D. Wu, C. Wu, Z. Zhu, L. Hu and J. Zhang, Ionic liquid exfoliated $Ti_3C_2T_x$ MXene nanosheets for photoacoustic imaging and synergistic photothermal/chemotherapy of cancer, *J. Mater. Chem. B*, 2022, **10**(8), 1226.

179 V. K. Deb and U. Jain, $Ti_3C_2$ (MXene), an advanced carrier system: role in photothermal, photoacoustic, enhanced drugs delivery and biological activity in cancer therapy, *Drug Delivery Transl. Res.*, 2024, **14**(11), 3009.

180 Y. Liu, Q. Han, W. Yang, X. Gan, Y. Yang, K. Xie, L. Xie and Y. Deng, Two-dimensional MXene/cobalt nanowire heterojunction for controlled drug delivery and chemo-photothermal therapy, *Mater. Sci. Eng., C*, 2020, **116**, 111212.

181 A. Seitak, A. Shanti, K. Al Adem, N. Farid, S. Luo, J. Iskandarov, G. N. Karanikolos, K. Liao, V. Chan and S. Lee, 2D MXenes for controlled releases of therapeutic proteins, *J. Biomed. Mater. Res.*, 2023, **111**(4), 514.

182 S. Wang, Z. Zhang, R. Tang, F. He, Y. Huang, Z. Nie and C. Lei, Responsive MXene nanovehicles deliver CRISPR/Cas12a for boolean logic-controlled gene editing, *Sci. China:Chem.*, 2022, **65**(11), 2318.

183 M. Tavakolizadeh, M. Atarod, S. J. Seyyed Tabaei, S. Sojdeh, E. Nazarzadeh Zare, M. Rabiee and N. Rabiee, Green modified-UiO-66/MXene sandwich composites for gene-chemotherapy synergistic cancer suppression: Co-delivery of doxorubicin and pCRISPR, *Alexandria Eng. J.*, 2023, **80**, 144.

184 R. Zhao, Y. Zhu, L. Feng, B. Liu, Y. Hu, H. Zhu, Z. Zhao, H. Ding, S. Gai and P. Yang, Architecture of Vanadium-Based MXene Dysregulating Tumor Redox Homeostasis for Amplified Nanozyme Catalytic/Photothermal Therapy, *Adv. Mater.*, 2024, **36**(2), 2307115.

185 G. Yang, J. Zhao, S. Yi, X. Wan and J. Tang, Biodegradable and photostable Nb2C MXene quantum dots as promising nanofluorophores for metal ions sensing and fluorescence imaging, *Sens. Actuators, B*, 2020, **309**, 127735.

186 H. Lin, Y. Wang, S. Gao, Y. Chen and J. Shi, Theranostic 2D Tantalum Carbide (MXene), *Adv. Mater.*, 2018, **30**(4), 1703284.

187 B. Zhou, H. Yin, C. Dong, L. Sun, W. Feng, Y. Pu, X. Han, X. Li, D. Du and H. Xu, *et al.*, Biodegradable and Excretable 2D W1.33C i-MXene with Vacancy Ordering for Theory-Oriented Cancer Nanotheranostics in Near-Infrared Biowindow, *Adv. Sci.*, 2021, **8**(24), 2101043.

188 G. Liu, J. Zou, Q. Tang, X. Yang, Y. Zhang, Q. Zhang, W. Huang, P. Chen, J. Shao and X. Dong, Surface Modified $Ti_3C_2$ MXene Nanosheets for Tumor Targeting Photothermal/Photodynamic/Chemo Synergistic Therapy, *ACS Appl. Mater. Interfaces*, 2017, **9**(46), 40077.

189 Y. Li, M. Lai, M. Hu, S. Zhao, B. Liu and J.-J. Kai, Insights into electronic and magnetic properties of MXenes: From a fundamental perspective, *Sustainable Mater. Technol.*, 2022, **34**, e00516.

190 Y. Lin, S. Xu, X. Zhao, L. Chang, Y. Hu, Z. Chen, X. Mei and D. Chen, Preparation of NIR-sensitive, photothermal and photodynamic multi-functional Mxene nanosheets for laryngeal cancer therapy by regulating mitochondrial apoptosis, *Mater. Des.*, 2022, **220**, 110887.

191 X. Chang, Q. Wu, Y. Wu, X. Xi, J. Cao, H. Chu, Q. Liu, Y. Li, W. Wu and X. Fang, *et al.*, Multifunctional Au Modified $Ti_3C_2$-MXene for Photothermal/Enzyme Dynamic/Immune Synergistic Therapy, *Nano Lett.*, 2022, **22**(20), 8321.

192 J. Xu, L. Chen, S. Ding, X. Dai, Y. Dai, Y. Chen and X. Ni, Self-generated Schottky barriers in niobium carbide MXene nanocatalysts for theory-oriented sonocatalytic and NIR-II photonic hyperthermia tumor therapy, *Nano Today*, 2023, **48**, 101750.

193 F. Gao, C. Xue, T. Zhang, L. Zhang, G.-Y. Zhu, C. Ou, Y.-Z. Zhang and X. Dong, MXene-Based Functional Platforms for Tumor Therapy, *Adv. Mater.*, 2023, **35**(51), 2302559.

194 M. Lee, J. Park, G. Choe, S. Lee, B. G. Kang, J. H. Jun, Y. Shin, M. C. Kim, Y. S. Kim and Y. Ahn, *et al.*, A Conductive and Adhesive Hydrogel Composed of MXene Nanoflakes as a Paintable Cardiac Patch for Infarcted Heart Repair, *ACS Nano*, 2023, **17**(13), 12290.

195 R. Guo, M. Xiao, W. Zhao, S. Zhou, Y. Hu, M. Liao, S. Wang, X. Yang, R. Chai and M. Tang, 2D $Ti_3C_2T_x$ MXene couples electrical stimulation to promote proliferation and neural differentiation of neural stem cells, *Acta Biomater.*, 2022, **139**, 105.

196 Y. Yu, H. Sun, Q. Lu, J. Sun, P. Zhang, L. Zeng, K. Vasilev, Y. Zhao, Y. Chen and P. Liu, Spontaneous formation of MXene-oxidized sono/chemo-dynamic sonosensitizer/nanocatalyst for antibacteria and bone-tissue regeneration, *J. Nanobiotechnol.*, 2023, **21**(1), 193.

197 M. S. Kang, H. J. Jang, H. J. Jo, I. S. Raja and D.-W. Han, MXene and Xene: promising frontier beyond graphene in tissue engineering and regenerative medicine, *Nanoscale Horiz.*, 2024, **9**(1), 93.

198 H. Park, J.-U. Kim, S. Kim, N. S. Hwang and H. D. Kim, Sprayable $Ti_3C_2$ MXene hydrogel for wound healing and drug release system, *Mater. Today Bio*, 2023, **23**, 100881.

199 K. Chen, Y. Hu, F. Wang, M. Liu, P. Liu, C. Li, Y. Yu, X. Xiao and Q. Feng, Ultra-stretchable, adhesive, and self-healing MXene/polyampholytes hydrogel as flexible and wearable epidermal sensors, *Colloids Surf., A*, 2022, **645**, 128897.

200 C. Ye, M. Wang, J. Min, R. Y. Tay, H. Lukas, J. R. Sempionatto, J. Li, C. Xu and W. Gao, A wearable aptamer nanobiosensor for non-invasive female hormone monitoring, *Nat. Nanotechnol.*, 2024, **19**(3), 330.

201 Z. Shi, C. Dai, P. Deng, X. Li, Y. Wu, J. Lv, C. Xiong, Y. Shuai, F. Zhang and D. Wang, *et al.*, Wearable battery-free smart bandage with peptide functionalized biosensors based on MXene for bacterial wound infection detection, *Sens. Actuators, B*, 2023, **383**, 133598.

202 A. Inman, B. S. Mohammadlou, K. Shevchuk, J. FitzPatrick, J. W. Park, N. Pacik-Nelson, I. Roslyk, E. M. Gallo, R. Garg and F. Vitale, *et al.*, MXene-enabled textile-based energy grid utilizing wireless charging, *Mater. Today*, 2024, **81**, 59.

203 G. Maroli, G. Rosati, S. Suárez-García, D. Bedmar-Romero, R. Kobrin, Á. González-Laredo, M. Urban, R. Alvárez-Diduk, D. Ruiz-Molina and A. Merkoçi, Wearable, battery-free, wireless multiplexed printed sensors for heat stroke prevention with mussel-inspired bio-adhesive membranes, *Biosens. Bioelectron.*, 2024, **260**, 116421.

204 F. Chen, J. Wang, L. Chen, H. Lin, D. Han, Y. Bao, W. Wang and L. Niu, A Wearable Electrochemical Biosensor Utilizing Functionalized $Ti_3C_2T_x$ MXene for the Real-Time Monitoring of Uric Acid Metabolite, *Anal. Chem.*, 2024, **96**(9), 3914.

205 V. Chaudhary, V. Khanna, H. T. Ahmed Awan, K. Singh, M. Khalid, Y. K. Mishra, S. Bhansali, C.-Z. Li and A. Kaushik, Towards hospital-on-chip supported by 2D MXenes-based 5th generation intelligent biosensors, *Biosens. Bioelectron.*, 2023, **220**, 114847.

206 Y.-C. Yang, Y.-T. Lin, J. Yu, H.-T. Chang, T.-Y. Lu, T.-Y. Huang, A. Preet, Y.-J. Hsu, L. Wang and T.-E. Lin, MXene Nanosheet-Based Microneedles for Monitoring Muscle Contraction and Electrostimulation Treatment, *ACS Appl. Nano Mater.*, 2021, **4**(8), 7917.

207 G. Rosati, P. B. Deroco, M. G. Bonando, G. G. Dalkiranis, K. Cordero-Edwards, G. Maroli, L. T. Kubota, O. N. Oliveira, L. A. M. Saito and C. de Carvalho Castro Silva, *et al.*, Introducing all-inkjet-printed microneedles for *in vivo* biosensing, *Sci. Rep.*, 2024, **14**(1), 29975.

208 C. Jin and Z. Bai, MXene-Based Textile Sensors for Wearable Applications, *ACS Sens.*, 2022, **7**(4), 929.

209 A. Parihar, A. Singhal, N. Kumar, R. Khan, M. A. Khan and A. K. Srivastava, Next-Generation Intelligent MXene-Based Electrochemical Aptasensors for Point-of-Care Cancer Diagnostics, *Nano-Micro Lett.*, 2022, **14**(1), 100.

210 M. Rossetti, C. Srisomwat, M. Urban, G. Rosati, G. Maroli, H. G. Yaman Akbay, O. Chailapakul and A. Merkoçi, Unleashing inkjet-printed nanostructured electrodes and battery-free potentiostat for the DNA-based multiplexed detection of SARS-CoV-2 genes, *Biosens. Bioelectron.*, 2024, **250**, 116079.

211 N. Driscoll, A. G. Richardson, K. Maleski, B. Anasori, O. Adewole, P. Lelyukh, L. Escobedo, D. K. Cullen, T. H. Lucas and Y. Gogotsi, *et al.*, Two-Dimensional $Ti_3C_2$ MXene for High-Resolution Neural Interfaces, *ACS Nano*, 2018, **12**(10), 10419.

212 N. Driscoll, K. Maleski, A. G. Richardson, B. Murphy, B. Anasori, T. H. Lucas, Y. Gogotsi and F. Vitale, Fabrication of $Ti_3C_2$ MXene Microelectrode Arrays for In Vivo Neural Recording, *J. Vis. Exp.*, 2020, **1940-087X**, 2020.

213 B. B. Murphy, P. J. Mulcahey, N. Driscoll, A. G. Richardson, G. T. Robbins, N. V. Apollo, K. Maleski, T. H. Lucas,

Y. Gogotsi and T. Dillingham, *et al.*, A Gel-Free $Ti_3C_2T$-Based Electrode Array for High-Density, High-Resolution Surface Electromyography, *Adv. Mater. Technol.*, 2020, **5**(8), 2000325.

214 R. Garg, N. Driscoll, S. Shankar, T. Hullfish, E. Anselmino, F. Iberite, S. Averbeck, M. Rana, S. Micera and J. R. Baxter, *et al.*, Wearable High-Density MXene-Bioelectronics for Neuromuscular Diagnostics, Rehabilitation, and Assistive Technologies, *Small Mathods*, 2023, **7**(8), 2201318.

215 L. Bi, R. Garg, N. Noriega, R. J. Wang, H. Kim, K. Vorotilo, J. C. Burrell, C. E. Shuck, F. Vitale and B. A. Patel, *et al.*, Soft, Multifunctional MXene-Coated Fiber Microelectrodes for Biointerfacing, *ACS Nano*, 2024, **18**(34), 23217.

216 S. Shankar, Y. Chen, S. Averbeck, Q. Hendricks, B. Murphy, B. Ferleger, N. Driscoll, M. Shekhirev, H. Takano and A. Richardson, *et al.*, Transparent MXene Microelectrode Arrays for Multimodal Mapping of Neural Dynamics, *Adv. Healthcare Mater.*, 2024, 2402576.

217 B. Erickson, R. Rich, S. Shankar, B. Kim, N. Driscoll, G. Mentzelopoulos, G. Fernandez-Nuñez, F. Vitale and J. D. Medaglia, Evaluating and benchmarking the EEG signal quality of high-density, dry MXene-based electrode arrays against gelled Ag/AgCl electrodes, *J. Neural Eng.*, 2024, **21**(1), 016005.

218 Y. Wu, Y. Li, Y. Liu, D. Zhu, S. Xing, N. Lambert, H. Weisbecker, S. Liu, B. Davis and L. Zhang, *et al.*, Orbit symmetry breaking in MXene implements enhanced soft bioelectronic implants, *Sci. Adv.*, 2024, **10**(40), eadp8866.

219 S.-H. Chen, H.-C. Chang, P.-W. Chiu, M.-Y. Hong, I. C. Lin, C.-C. Yang, C.-T. Hsu, C.-W. Ling, Y.-H. Chang and Y.-Y. Cheng, *et al.*, Triage body temperature and its influence on patients with acute myocardial infarction, *BMC Cardiovasc. Disord.*, 2023, **23**(1), 388.

220 M. A. Unal, F. Bayrakdar, L. Fusco, O. Besbinar, C. E. Shuck, S. Yalcin, M. T. Erken, A. Ozkul, C. Gurcan and O. Panatli, *et al.*, 2D MXenes with antiviral and immunomodulatory properties: A pilot study against SARS-CoV-2, *Nano Today*, 2021, **38**, 101136.

221 C. Weiss, M. Carriere, L. Fusco, I. Capua, J. A. Regla-Nava, M. Pasquali, J. A. Scott, F. Vitale, M. A. Unal and C. Mattevi, *et al.*, Toward Nanotechnology-Enabled Approaches against the COVID-19 Pandemic, *ACS Nano*, 2020, **14**(6), 6383.

222 L. Fusco, A. Gazzi, C. E. Shuck, M. Orecchioni, D. Alberti, S. M. D'Almeida, D. Rinchai, E. Ahmed, O. Elhanani and M. Rauner, *et al.*, Immune Profiling and Multiplexed Label-Free Detection of 2D MXenes by Mass Cytometry and High-Dimensional Imaging, *Adv. Mater.*, 2022, **34**(45), 2205154.

223 L. Fusco, A. Gazzi, C. E. Shuck, M. Orecchioni, E. I. Ahmed, L. Giro, B. Zavan, A. Yilmazer, K. Ley and D. Bedognetti, *et al.*, V4C3 MXene Immune Profiling and Modulation of T Cell-Dendritic Cell Function and Interaction, *Small Mathods*, 2023, **7**(8), 2300197.

224 M. Khazaei, A. Ranjbar, K. Esfarjani, D. Bogdanovski, R. Dronskowski and S. Yunoki, Insights into exfoliation possibility of MAX phases to MXenes, *Phys. Chem. Chem. Phys.*, 2018, **20**(13), 8579.

225 R. Khaledialidusti, M. Khazaei, S. Khazaei and K. Ohno, High-throughput computational discovery of ternary-layered MAX phases and prediction of their exfoliation for formation of 2D MXenes, *Nanoscale*, 2021, **13**(15), 7294.

226 M. Khazaei, A. Mishra, N. S. Venkataramanan, A. K. Singh and S. Yunoki, Recent advances in MXenes: From fundamentals to applications, *Curr. Opin. Solid State Mater. Sci.*, 2019, **23**(3), 164.

227 A. Gkountaras, Y. Kim, J. Coraux, V. Bouchiat, S. Lisi, M. W. Barsoum and T. Ouisse, Mechanical Exfoliation of Select MAX Phases and Mo4Ce4Al7C3 Single Crystals to Produce MAXenes, *Small*, 2020, **16**(4), 1905784.

228 P. Srivastava, A. Mishra, H. Mizuseki, K.-R. Lee and A. K. Singh, Mechanistic Insight into the Chemical Exfoliation and Functionalization of $Ti_3C_2$ MXene, *ACS Appl. Mater. Interfaces*, 2016, **8**(36), 24256.

229 M. Wu, M. He, Q. Hu, Q. Wu, G. Sun, L. Xie, Z. Zhang, Z. Zhu and A. Zhou, $Ti_3C_2$ MXene-Based Sensors with High Selectivity for NH3 Detection at Room Temperature, *ACS Sens.*, 2019, **4**(10), 2763.

230 F. Zeng, X. Feng, X. Chen, Q. Yao, Y. Miao, L. Dai, Y. Li and J. Tang, First-principles analysis of $Ti_3C_2T_x$ MXene as a promising candidate for SF6 decomposition characteristic components sensor, *Appl. Surf. Sci.*, 2022, **578**, 152020.

231 J. Björk, J. Halim, J. Zhou and J. Rosen, Predicting chemical exfoliation: fundamental insights into the synthesis of MXenes, *npj 2D Mater. Appl.*, 2023, **7**(1), 5.

232 B. Ryu, L. Wang, H. Pu, M. K. Y. Chan and J. Chen, Understanding, discovery, and synthesis of 2D materials enabled by machine learning, *Chem. Soc. Rev.*, 2022, **51**(6), 1899.

233 N. C. Frey, J. Wang, G. I. Vega Bellido, B. Anasori, Y. Gogotsi and V. B. Shenoy, Prediction of Synthesis of 2D Metal Carbides and Nitrides (MXenes) and Their Precursors with Positive and Unlabeled Machine Learning, *ACS Nano*, 2019, **13**(3), 3031.

234 M. He and L. Zhang, Machine learning and symbolic regression investigation on stability of MXene materials, *Comput. Mater. Sci.*, 2021, **196**, 110578.

235 H. Ding, Z. Zeng, Z. Wang, X. Li, T. Yildirim, Q. Xie, H. Zhang, S. Wageh, A. A. Al-Ghamdi and X. Zhang, *et al.*, Deep Learning-Enabled MXene/PEDOT:PSS Acoustic Sensor for Speech Recognition and Skin-Vibration Detection, *Adv. Intell. Syst.*, 2022, **4**(10), 2200140.

236 W. Wang, H. Zhou, Z. Xu, Z. Li, L. Zhang and P. Wan, Flexible Conformally Bioadhesive MXene Hydrogel Electronics for Machine Learning-Facilitated Human-Interactive Sensing, *Adv. Mater.*, 2024, **36**, 2401035.

237 H. Yang, J. Li, X. Xiao, J. Wang, Y. Li, K. Li, Z. Li, H. Yang, Q. Wang and J. Yang, *et al.*, Topographic design in wearable MXene sensors with in-sensor machine learning for full-body avatar reconstruction, *Nat. Commun.*, 2022, **13**(1), 5311.

238 G.-Y. Gou, X.-S. Li, J.-M. Jian, H. Tian, F. Wu, J. Ren, X.-S. Geng, J.-D. Xu, Y.-C. Qiao and Z.-Y. Yan, *et al.*, Two-stage

amplification of an ultrasensitive MXene-based intelligent artificial eardrum, *Sci. Adv.*, 2022, **8**(13), eabn2156.

239 S. Duan, Y. Lin, Z. Wang, J. Tang, Y. Li, D. Zhu, J. Wu, L. Tao, C.-H. Choi and L. Sun, *et al.*, Conductive Porous MXene for Bionic, Wearable, and Precise Gesture Motion Sensors, *Research*, 2021, **2021**, DOI: 10.34133/2021/9861467.

240 K. J. Jyothish and S. Mishra, A Survey on Robotic Prosthetics: Neuroprosthetics, Soft Actuators, and Control Strategies, *ACM Comput. Surv.*, 2024, **56**(8), 195.

241 S. Sahoo, N. A. Koshi, S.-C. Lee, S. Bhattacharjee and B. Muralidharan, Density Functional Theory of Straintronics Using the Monolayer-Xene Platform: A Comparative Study, *ACS Appl. Nano Mater.*, 2024, **7**(3), 2939.

242 M. Takahashi, Flat building blocks for flat silicene, *Sci. Rep.*, 2017, **7**(1), 10855.

243 G. Li, L. Zhang, W. Xu, J. Pan, S. Song, Y. Zhang, H. Zhou, Y. Wang, L. Bao and Y.-Y. Zhang, *et al.*, Stable Silicene in Graphene/Silicene van der Waals Heterostructures, *Adv. Mater.*, 2018, **30**(49), 1804650.

244 C. Grazianetti, A. Molle and C. Martella, The future of Xenes beyond graphene: challenges and perspective, *2D Mater.*, 2024, **11**(4), 042005.

245 W. Tao, N. Kong, X. Ji, Y. Zhang, A. Sharma, J. Ouyang, B. Qi, J. Wang, N. Xie and C. Kang, *et al.*, Emerging two-dimensional monoelemental materials (Xenes) for biomedical applications, *Chem. Soc. Rev.*, 2019, **48**(11), 2891.

246 Y. Xiao, Y. X. Pang, Y. Yan, P. Qian, H. Zhao, S. Manickam, T. Wu and C. H. Pang, Synthesis and Functionalization of Graphene Materials for Biomedical Applications: Recent Advances, Challenges, and Perspectives, *Adv. Sci.*, 2023, **10**(9), 2205292.

247 Q. Li, X. Wu, S. Mu, C. He, X. Ren, X. Luo, M. Adeli, X. Han, L. Ma and C. Cheng, Microenvironment Restruction of Emerging 2D Materials and their Roles in Therapeutic and Diagnostic Nano-Bio-Platforms, *Adv. Sci.*, 2023, **10**(20), 2207759.

248 Y. Gogotsi and Q. Huang, MXenes: Two-Dimensional Building Blocks for Future Materials and Devices, *ACS Nano*, 2021, **15**(4), 5775.